ADAPTIVE ESTIMATION AND HEURISTIC OPTIMIZATION OF NONLINEAR SPACECRAFT ATTITUDE DYNAMICS

DISSERTATION

Joshuah A. Hess, Captain, USAF

AFIT-ENY-DS-16-S-061

DEPARTMENT OF THE AIR FORCE
AIR UNIVERSITY

AIR FORCE INSTITUTE OF TECHNOLOGY

Wright-Patterson Air Force Base, Ohio

AFIT-ENY-DS-16-S-061

ADAPTIVE ESTIMATION AND HEURISTIC OPTIMIZATION OF NONLINEAR SPACECRAFT ATTITUDE DYNAMICS

DISSERTATION

Presented to the Faculty

Graduate School of Engineering and Management

Air Force Institute of Technology

Air University

Air Education and Training Command

in Partial Fulfillment of the Requirements for the

Degree of Doctor of Philosophy in Aerospace Engineering

Joshuah A. Hess, B.S., M.S.

Captain, USAF

September 2016

ADAPTIVE ESTIMATION AND HEURISTIC OPTIMIZATION OF

NONLINEAR SPACECRAFT ATTITUDE DYNAMICS

Joshuah A. Hess, B.S., M.S.
Captain, USAF

Committee Membership:

Dr. Eric D. Swenson
Chair

Dr. Jonathan T. Black
Member

Dr. Richard G. Cobb
Member

Dr. Richard T. Martin
Member

ADEDEJI B. BADIRU, PhD
Dean, Graduate School of Engineering
and Management

AFIT-ENY-DS-16-S-061

Abstract

For spacecraft conducting on-orbit operations, changes to the structure of the spacecraft are not uncommon. These planned or unanticipated changes in inertia properties couple with the spacecraft's attitude dynamics and typically require estimation. For systems with time-varying inertia parameters, multiple model adaptive estimation (MMAE) routines can be utilized for parameter and state estimates. MMAE algorithms involve constructing a bank of recursive estimators, each assuming a different hypothesis for the system's dynamics. This research has three distinct, but related, contributions to satellite attitude dynamics and estimation. In the first part of this research, MMAE routines employing parallel banks of unscented attitude filters are applied to analytical models of spacecraft with time-varying mass moments of inertia (MOI), with the objective of estimating the MOI and classifying the spacecraft's behavior. New adaptive estimation techniques were either modified or developed that can detect discontinuities in MOI up to 98% of the time in the specific problem scenario. Second, heuristic optimization techniques and numerical methods are applied to Wahba's single-frame attitude estimation problem, decreasing computation time by an average of nearly 67%. Finally, this research poses MOI estimation as an ODE parameter identification problem, achieving successful numerical estimates through shooting methods and exploiting the polhodes of rigid body motion with results, on average, to be within $< 1\%$ to 5% of the true MOI values.

Acknowledgments

I would first like to extend a sincere thank you to my advisor, Dr. Eric Swenson. His guidance, mentorship, and trust have been invaluable and instrumental in developing and completing this dissertation. I would like to thank Dr. Jonathan Black, Dr. Richard Cobb, and Dr. Richard Martin for their time, effort, guidance, and willingness to serve on my research committee. To the committee as a whole, thank you for extending to me your trust and the degree of independence to develop knowledge and contribute to the field. To Dr. Fred Leve, thank you for introducing me to the community's need for this problem, and for your help in constructing the research objectives and key dynamics, and for your continued support.

During the course of a dissertation, it is easy to become lost in a sea of technical jargon and extremely niched research. I would also like to thank my office colleagues for providing not only technical inputs, but also for their friendship outside of AFIT. To my first calculus teacher in high school, thank you for building such a strong foundation of independent thought and analytical reasoning.

Finally, to my friends and family. Thank you for helping me balance research with life during the past three years. My mother, stepfather, grandparents, and sister have been a sounding board for ideas and a source of inspiration. To my fiancée, you and your family have been by my side through this entire experience, and thank you for your commitment, ideas, time, and your positive attitude and support.

To the countless number of friends, family, and colleagues who have helped along the way, I give you my sincerest thanks.

Joshuah A. Hess

Table of Contents

List of Figures

List of Tables

List of Algorithms

List of Symbols

Symbol	Definition
$\mathbf{A}$	Jacobian
$\mathbf{H}$	Angular momentum vector
$\mathbf{M}$	External moment vector
$\boldsymbol{\omega}$	Angular velocity vector
$\mathbf{I}$	Moment of inertia matrix
A, B, C	Major, intermediate, and minor principal MOI
I_1, I_2, I_3	Alternate form for major, intermediate, and minor MOI
Ω	Relative spin rate in axisymmetric angular velocity
$\mathbf{R}^{bi}$	Rotation matrix
Φ	Principal rotation angle
$\hat{e}$	Eigenaxis or principal rotation angle
$\mathbf{q}$	Quaternion
$\boldsymbol{\varrho}$	Three components of quaternion
$\mathbf{1}_{n \times n}$	$N \times N$ identity matrix
$\mathbf{0}_{n \times n}$	$N \times N$ zero matrix
$(\mathbf{a})^{\times}$	Skew-symmetric matrix of vector $\mathbf{a}$
$\boldsymbol{\Phi}$	State transition matrix
$\boldsymbol{\Lambda}$	System input allocation matrix
$\boldsymbol{\Gamma}$	System disturbance allocation matrix
$\boldsymbol{P}$	Covariance matrix
$\boldsymbol{Q}$	Process noise matrix
$\boldsymbol{R}$	Measurement noise matrix
$\mathbf{H}$	Measurement relation matrix

Symbol	Definition
$\mathbf{f}(\mathbf{x}, t)$	System dynamics
$\mathbf{h}(\mathbf{x}, t)$	Measurement state relation
$\boldsymbol{\chi}$	Sigma points in UKF
J	Cost function
w_k	Weighting value
$\boldsymbol{\nu}$	Residual vector
(f, a)	Tuning values in UKF
$\tilde{\mathbf{y}}$	Measurement vector
$p(\cdot)$	Probability distribution function
$\mathbf{x}$	State vector
$(\hat{\cdot})$	Indicates estimate
$\mathbf{p}$	Parameter vector
λ_1, λ_2	Low-pass filter values
En	Innovation metric
B_i	Magnetic field components
$\mathbf{v}, \mathbf{n}, \boldsymbol{\eta}$	Noise vector
σ	Standard deviation, unless specified otherwise
m	Mass
Δt	Time step
$\mathbf{K}$	Davenport K-matrix
χ	Constriction factor in PSO
ϕ_e	Principal angle error metric
H	Scalar angular momentum
T	Scalar rotational kinetic energy
k_1, k_2, k_3	Smelt parameters

List of Acronyms

Acronym	Definition
AFIT	Air Force Institute of Technology
AFSPC	Air Force Space Command
AGI	Analytical Graphics Incorporated
ALM	Adaptive Likelihood Mixture
ASAT	Anti Satellite
ADCS	Attitude Determination and Control System
BVP	Boundary Value Problem
CDF	Cumulative Distribution Function
COM	Center of Mass
CRP	Classical Rodrigues Parameters
DOF	degrees of freedom
EKF	Extended Kalman Filter
EOM	Equations of Motion
FQS	Fast Quartic Solver
GEO	geosynchronous Earth orbit
GA	Genetic Algorithm
GPS	Global Positioning System
HOUF	Higher Order Unscented Filter
IC	initial conditions
IMM	Interacting Multiple Model
IMU	Inertial Measurement Unit
ISR	Intelligence, Surveillance, and Reconnaissance
JSpOC	Joint Space Operations Center

Acronym	Definition
LEO	low Earth orbit
LKF	Linear Kalman Filter
LOS	Line of Sight
MAP	Maximum a Posteriori
MEO	medium Earth orbit
MMAE	Multiple Model Adaptive Estimation
MOI	Moment of Inertia
MRP	Modified Rodrigues Parameters
NRC	National Research Council
NSSS	National Security Space Strategy
ODE	Ordinary Differential Equations
PDF	Probability Distribution Function
PID	Proportional Integral Derivative
PSO	Particle Swarm Optimization
QUEST	Quaternion Estimation
RSO	Resident Space Object
RMM	Residual Magnetic Moment
RV	random variable
SGP4	Simplified General Perturbations 4
SP	Special Perturbations
SSA	Space Situational Awareness
SQP	Sequential Quadratic Programming
STM	State Transition Matrix
SVD	Singular Value Decomposition
TAM	Three Axis Magnetometer

Acronym	Definition
TVMOI	Time Varying Moment of Inertia
US	United States
USAF	United States Air Force
UKF	Unscented Kalman Filter
USQUE	Unscented Quaternion Estimation

ADAPTIVE ESTIMATION AND HEURISTIC OPTIMIZATION OF

NONLINEAR SPACECRAFT ATTITUDE DYNAMICS

I.   Introduction

1.1   Motivation

The National Security Space Strategy (NSSS) highlights the vital role of space in Intelligence, Surveillance, and Reconnaissance (ISR), power projection, diplomacy, and military operations 1][1]. Further, the NSSS details the increasingly *congested, contested*, and *competitive* space environment and the need to maintain the strategic national security advantages afforded by space. The growing global domain of space operations requires an improvement in shared Space Situational Awareness (SSA), and the NSSS recommends the United States (US) invest its knowledge base to foster SSA cooperation while protecting US and partner space capabilities [1].

There are over 1,000 operational satellites and an excess of 11,000 pieces of trackable debris among the low Earth orbit (LEO), medium Earth orbit (MEO), and geosynchronous Earth orbit (GEO) orbital regimes [1; 2]. The Joint Space Operations Center (JSpOC) performs the SSA mission by tasking collections from various sensor sources to collect orbital data and perform current and future predictions of space object ephemeris. The SSA mission is becoming increasingly difficult when considering the trend towards smaller space vehicles [3], discussion of disaggregated mission sets [4], as well as debris created from collisions [5], Anti Satellite (ASAT) testing [1], and other catastrophic events.

Further impeding the SSA mission are the methods by which the JSpOC tracks and propagates Resident Space Object (RSO)s. In 2011, Air Force Space

1

Command (AFSPC) tasked the National Research Council (NRC) to "assess (their) astrodynamics standards...and their effectiveness..." [6]. Nongravitational effects (e.g., solar radiation pressure, atmospheric drag) perturb the nominal Keplerian motion of an object with a wide range of effects depending on the position and attitude of the object. AFSPC employs a number of astrodynamics algorithms to generate ephemerides with varying degrees of accuracy and inclusions of perturbing forces, which directly affect computational time. The analytic models in the more commonly known Simplified General Perturbations 4 (SGP4) and Special Perturbations (SP) numerical integration techniques do not take into account certain key satellite properties, such as attitude and shape, and additions of these states could improve orbit predictions [6].

The accuracy from including an RSO's attitude within an orbital state propagator is limited by the accuracy of the attitude estimate. The attitude dynamics of a rigid (or flexible) body are highly nonlinear, coupled, and sensitive to particular system parameters such as the spacecraft moment of inertia (MOI) [7]. Accurate attitude determination and the tight coupling between the MOI and rotational dynamics of the spacecraft is of concern to SSA operators. Miscalculation of the spacecraft orientation, changes in MOI, or assumptions of rigidity could directly contribute to the observed effect of non-gravitational perturbations on an orbit and the consequential error and state covariance growth. Moment of inertia changes are not always deterministic. Unplanned changes to a spacecraft's structure can result from debris, external actors, or hardware faults. For example, the recent loss of the Japanese satellite *Hitomi* has been attributed to human error and possible solar panel faults [8]. In this example, adaptive estimation techniques applied to the available streaming attitude telemetry could have potentially identified the fault through various filters assuming different MOI modes.

2

As three independent parameters are needed to define a body's attitude, the number of sensor measurements often pose the attitude estimation as under- or overdetermined, and implies that attitude *determination* algorithms are essentially *estimation* routines. Some particular spacecraft configurations allow for special case solutions of Euler's rotational equations (for example, an axisymmetric, torque-free rigid body), but nonlinearities and external forcing functions will perturb even this simplistic model and one must estimate the attitude. Various sensor sources ranging from inertial measurement units to star sensors are used to construct observations for attitude estimation algorithms. The sensor observations are then operated on by some estimation routine in order to determine the state and account for sensor noise. A survey of various estimation and filtering techniques will be discussed in Chapter 2.

The NRC found that for the nonlinear governing equations in astrodynamics, advanced estimation techniques should be employed to characterize state estimates and their uncertainties [6]. Space is a data-sparse environment, and, consequently, convergence times for state estimators and filters can be of considerable duration. Multiple model filters have been shown to be capable of converging on state estimates with limited data [6; 9]. Multiple model techniques have also demonstrated operational efficacy in detecting the states of maneuvering missiles and aircraft where sudden changes in dynamics are experienced [6; 10; 11]. Multiple model techniques are well posed for the spacecraft maneuver estimation problem, determining if and how a maneuver occurred for a given satellite at a given time [12–15]. The rotational analog to the translational maneuver detection seeks to determine sudden changes in a spacecraft's MOI via streaming attitude telemetry. Sudden or gradual MOI changes that are not accounted for are likely to introduce an evolving error into the coupled

rotational and translational dynamics, potentially leading to position tracking errors while hindering on-orbit missions that are functions of attitude.

1.2   Problem Statement

For spacecraft conducting on-orbit operations, changes to the structure of the spacecraft are not uncommon. The extension of a communications antenna, deployment of a gravity gradient boom, solar panel rotation, fuel usage, or catastrophic events such as debris collisions, will produce changes in the spacecraft's MOI. There is a tight coupling between MOI and rotational dynamics which further couples with translational motion when model perturbations are included, or the point mass assumption is relaxed. Thus, accurate situational awareness and characterization of a spacecraft is a function of both translational and rotational motion, and requires accurate attitude determination and estimation of structural properties.

1.3   Research Objectives

The objective of this research is to develop and evaluate new estimation methodologies to determine spacecraft attitude and MOI, and probabilistically classify spacecraft behavior. Chapter 3 examines a new application of adaptive attitude estimation to a spacecraft with time-varying MOI as a proof of concept that lays the foundation for future hardware experiments. In Chapter 4, newly developed computational techniques and heuristic optimization methods are evaluated with respect to the single-frame attitude estimation problem where orientation is determined by using multiple unit vector observations. In Chapter 5, the MOI estimation problem is formulated as one of parameter estimation within a system of nonlinear Ordinary Differential Equations (ODE), wherein single-shooting numerical methods are enhanced. Finally, also in Chapter 5, classical properties of analytical

mechanics are combined with hybrid optimization techniques to estimate principal MOI.

1.4   Methodology Overview

The dissertation is formatted as three separate, but distinct, articles intended as journal submissions. Chapters 3 through 5 are related with the commonality of studying satellite attitude dynamics, rigid body motion, and estimation theory. Due to this construct, background and methodology are repeated throughout. Chapter 3 demonstrates a novel application of MMAE to attitude dynamics with a time-varying MOI, while Chapter 4 looks at attitude estimation as a single-frame problem rather than the filtering methods in Chapter 3. Finally, Chapter 5 enhances and develops algorithms for estimating the spacecraft mass MOI, a key system characteristic of rigid body motion. This section provides a main overview of the methodology used in each chapter.

The research presented in Chapter 3 examines the application of MMAE to spacecraft attitude determination using an on-board gyro and three-axis magnetometer. The multiple model filter bank is constructed of variants of the Unscented Quaternion Estimation (USQUE) filter developed by Crassidis, et al. [16]. Three scenarios are examined: (1) a scenario identifying the correct relative MOI ratio; (2) determining an input command to a deployable, rotating payload; and (3) detecting a series of separating payloads. Truth data is simulated using Euler's Equations of Motion (EOM) and converted to measurements while corrupting with Gaussian noise for filter inputs. Finally, a series of adaptive estimation algorithms are analyzed for robustness and detection capabilities.

Chapter 4 examines the use of new computational and optimization techniques to the single-frame attitude estimation problem. For the computational portion, a series of test cases constructed by Markley [17] are used which are designed to be

representative of various sensor combinations, observations, and sensor noise. The research makes use of Strobach's Fast Quartic Solver [18] to rapidly solve a quartic eigendecomposition problem to compute the optimal quaternion, and is compared to classical methods such as QUEST and the q-method. The optimization portion performs a Monte Carlo type simulation on a series of vector measurements with varying noise, and directly minimizes a least-squares cost function using particle swarm optimization (PSO) and a genetic algorithm (GA). Various combinations of noise levels, vector observations, and optimization solver parameters are analyzed. Results are assessed using computational time and attitude error as metrics.

Chapter 5 presents a novel approach to determining the relative MOI ratios and the actual principal MOI values given angular velocity measurements. The relative MOI ratios are estimated by constructing an algorithm to perform single-shooting on Euler's equations while iterating on the MOI ratios via the Levenberg-Marquardt variant of Newton-Raphson iteration. Known external torques are then accounted for by re-deriving a Jacobian in an effort to determine the principal MOI using single-shooting. Finally, the principal MOI is estimated by exploiting a classical shape in rigid body motion known as a polhode, which is formed by the intersection of an angular momentum and kinetic energy ellipsoid. Various sets of angular velocity measurements are simulated, and a two-step optimization process is employed that uses intermediate conversions between variables known as Smelt parameters. The shape of two ellipsoids is then iterated on until their intersection is within a degree of numerical tolerance error when compared to the measured polhode.

1.5 Research Contributions

The development of an adaptive estimation methodology in Chapter 3 has immediate and future impacts to the space community. This research presented a first-of-its-kind examination of time-varying MOI characterization using streaming

6

attitude data. Although this research focuses on the use of on-board sensor suites, ground-based or stand-off sensors, that are capable of detecting some phenomenology that correlates with attitude, follow analogous algorithms. The problem of detecting separating payloads is also directly analogous to estimating positive additions to the MOI or spacecraft structure. This work demonstrated that time-varying MOI characterization is possible using adaptive estimation and has set a path for hardware experimentation, and the reformulation of the problem that is not as reliant on the variability of filters in the adaptive estimation bank.

A key contribution from the work in Chapter 4 resulted in the application of a rapid quartic root solver applied to the characteristic equation from Wahba's problem for a savings in computational cost. This research also allowed for the contribution of a new application of heuristic optimization to a total least-squares problem for attitude determination. For the rapid root solver, faster and precise attitude estimates allow for decreased time lag between observation and estimate, and can assist in the implementation of near real-time optimal control. One of the main benefits to estimating the quaternion via a heuristic method is a 'close enough' initial guess is not required, as heuristic techniques implement randomly chosen initial candidate solutions. Although these optimization methods may be too computationally demanding for on-board processing, the heuristic algorithms are applicable to off-line post-processing of a vector observation time history.

The research contributions from Chapter 5 are more mathematical and abstract in nature, but do present two new methodologies to estimate structural configurations of spacecraft using angular rate data. Relative MOI ratios and principal MOI values have not, to the author's knowledge, been posed as an ODE parameter estimation problem using Euler's equations, and, further, have not been estimated via single-shooting techniques. For torque free rigid body motion, the literature has also

indicated that only the relative MOI ratios can typically be estimated, but via intermediate normalizations and two-step optimization this research has shown that, given a measured set of angular velocity, the principal MOI of a spacecraft can be estimated. For a tumbling non-cooperative spacecraft or piece of debris, capture requires some knowledge of the body's MOI. This research has shown that, by some type of sensor measurement that results in an angular velocity estimate, the principal MOI can be estimated by exploiting the polhodes of classic analytical mechanics.

1.6 Dissertation Overview

The author has organized this dissertation into six chapters. In Chapter 1, the problem and its motivation are introduced. Chapter 2 presents a broad, in-depth review of previous research in the various fields this dissertation extends. Chapter 3 demonstrates a novel application of MMAE to attitude dynamics with a time-varying MOI, while Chapter 4 looks at attitude estimation as a single-frame problem rather than the filtering methods in Chapter 3. Chapter 5 enhances and develops algorithms for estimating the spacecraft mass MOI, a key system characteristic of rigid body motion. Chapter 6 concludes the dissertation by providing a summary of the research results, detailed contributions made by this work, and future work the author has deemed noteworthy. As the dissertation is presented as distinct but related articles, there will inevitably be some overlapping background, literature review, and methodology in each chapter that is included for completeness, but may appear as redundant to the reader. Hyperlinks are included throughout to enable quick reference to equations, sections, sources, and acronyms. The following subsections present a brief overview of Chapters 3 to 5.

1.6.1 Adaptive Estimation of Nonlinear Spacecraft Attitude Dynamics with Time Varying Moments of Inertia.

In Chapter 3 a series of scenarios are constructed to evaluate the performance of various adaptive estimation routines in identifying and estimating a spacecraft's time varying MOI. To the extent of the author's knowledge, this effort is the first application of adaptive estimation to the case of a variable spacecraft MOI using streaming attitude data. A methodology is developed to detect sudden MOI changes using a bank of Unscented Kalman Filters as a numerical testbed for future real-world implementation. A hybrid adaptive estimation algorithm to detect sudden parameter changes in nonlinear systems is developed combining two state of the art routines. The work in [19] presented the preliminary results of the research discussed in Chapter 3.

1.6.2 Alternate Numerical Solutions to Wahba's Problem of Sequential Frame Attitude Estimation Using Heuristic Optimization and Fast Quartic Numerical Solvers.

In Chapter 4 the single-frame estimation problem is solved by a rapid numerical solver and by heuristic optimization techniques. Grace Wahba posed the satellite attitude determination problem as a least-squares optimization problem in 1965 [20]. That is, given N sets of simultaneous vector measurements in two different reference frames, Wahba's problem seeks to approximate the rotation matrix between the two frames that minimizes a particular cost function. This rotation matrix defines the current attitude estimate. Classical numerical solutions to Wahba's problem include Davenport's q-method [21], TRIAD [22], QUEST [23], and several other techniques [24]. This research proposes the application of Strobach's Fast Quartic Solver [18] to quickly solve a fourth-order eigenvalue problem required for the quaternion attitude estimate. Additionally, this work examines the application of heuristic based

techniques, to include particle swarm optimization (PSO) and genetic algorithms (GA), to solve Wahba's minimization problem to estimate spacecraft attitude.

1.6.3 *Spacecraft Moment of Inertia Estimation Posed as an Ordinary Differential Equation Parameter Estimation.*

Chapter 5 investigates the problem of MOI estimation given measurements of the rotational trajectory and initial conditions. The current problem is solved in two manners. The first approach formulates the problem as a parameter estimation in a nonlinear ordinary differential equation under the presence of stochastic measurement noise. Relative MOI ratios are estimated with Single-shooting methods employing Levenberg-Marquardt iteration schemes. The second approach, in a new fashion, employs a cost function exploiting the classical polhodes of analytical mechanics and known constants of the motion, within a two-step optimization process utilizing heuristic optimization techniques as warm starts to Sequential Quadratic Programming (SQP) optimizers. Intermediate normalizations and use of Smelt parameters are used to minimize the cost function to estimate actual principal MOI values rather than relative MOI ratios.

1.7 Chapter Summary

This chapter served to introduce the reader to research and results discussed throughout this dissertation. Motivating examples were given and a problem statement detailed. From this problem statement, research goals were developed. The methodology used in the research was detailed and the contributions to the field were also discussed.

II. Background

This chapter provides a discussion on related work in satellite attitude dynamics, attitude and adaptive estimation, MOI estimation, and heuristic optimization. The review presented in this chapter provides a contained, consolidated basis of research upon which this dissertation is built. An additional goal of this chapter is to establish boundaries on relevant research in order to demonstrate contributions to the fields made by this dissertation. The chapter begins with a philosophical and mathematical discussion of spacecraft attitude dynamics. Next, this chapter provides a discussion on estimation theory immediately followed by its application to spacecraft attitude estimation. A survey on adaptive estimation, a methodology critical to the results of Chapter 3, is then provided. The estimation portion of this chapter will then finish with a discussion of spacecraft MOI estimation, the focus of Chapter 5. Next, a survey on heuristic optimization, focusing on PSO and GA, is provided as these methods are pertinent to the results presented in Chapters 4 and 5. As this document is constructed with three distinct articles, some background in Chapters 3 to 5 may appear repetitive when compared to the forthcoming discussing. This section is intended to provide a broad overview, while individual chapters will provide more details regarding the literature review.

2.1 A Discussion on Rigid Body Motion and Spacecraft Attitude Dynamics

The commonality among the three distinct research projects presented in this dissertation is spacecraft attitude dynamics. Therefore, this section will present a top-level discussion on rigid body motion and attitude dynamics. The derivation of Euler's equations will be presented along with a particular solution to the system. A discussion on attitude parameterization will be presented, accompanied by the

quaternion equations of motion. The section will conclude by examining the impact of time-varying MOI on a spacecraft's attitude motion.

2.1.1 Euler's Rotational Equations of Motion.

The rotational dynamics of a rigid body, where rigid implies that the distance between any two points on the body is constant, are derived by essentially restating the conservation of angular momentum principle. That is, in an inertial frame, the time rate of change of a body's angular momentum, $\mathbf{H}$, is equal to the vector sum of external torques, $\mathbf{M}$, acting on the body. Let $\boldsymbol{\omega}$ denote the angular velocity of a body expressed in a reference frame fixed to the body, but with respect to some inertial frame, and let $\mathbf{I}$ denote a real, symmetric 3×3 matrix whose elements are the body's moments and products of inertia. The conservation of angular momentum principle can be stated mathematically as

$$\mathbf{M} = \dot{\mathbf{H}}, \tag{2.1}$$

where $\mathbf{H}$ is expressed as

$$\mathbf{H} = \mathbf{I}\boldsymbol{\omega}, \tag{2.2}$$

and the $\dot{(\,)}$ notation indicates an inertial derivative with respect to time. Substituting Eq. (2.2) into Eq. (2.1), and subsequently applying the Transport Theorem to Eq.(2.1) results in the following body-frame derivative

$$\mathbf{M} = \mathbf{I}\dot{\boldsymbol{\omega}} + \boldsymbol{\omega}^{\times}\mathbf{I}\boldsymbol{\omega}, \tag{2.3}$$

where the MOI has been assumed constant, and the $\boldsymbol{\omega}^{\times}$ operator is the skew-symmetric matrix multiplication representation of a cross-product, given as

$$\boldsymbol{\omega}^{\times} = \begin{bmatrix} 0 & -\omega_3 & \omega_2 \\ \omega_3 & 0 & -\omega_1 \\ \omega_2 & \omega_1 & 0 \end{bmatrix}. \tag{2.4}$$

12

Solving for $\dot{\boldsymbol{\omega}}$, the rotational equations of motion become

$$\dot{\boldsymbol{\omega}} = \mathbf{I}^{-1}\left[\mathbf{M} - \boldsymbol{\omega}^{\times}\mathbf{I}\boldsymbol{\omega}\right] \tag{2.5}$$

The system of equations represents a set of coupled, nonlinear ODE, the solution of which yields the instantaneous angular velocity $\boldsymbol{\omega}$. Since the attitude of a body is an orientation with respect to another reference frame, this angular velocity is then used to map to a particular attitude parameterization, discussed in Sections 2.1.3 and 2.1.4. The coupled, nonlinear ODEs of rotational motion are difficult to solve in closed-form. The following presents a popular particular case of torque-free motion.

2.1.2 Closed-Form Solutions for Spacecraft Rigid Body Motion.

Without loss of generality, the rigid body is now assumed as a rigid spacecraft, and the assumption is made that there are no external torques, and that MOI matrix has been diagonalized such that

$$\mathbf{I} = \begin{bmatrix} A & 0 & 0 \\ 0 & B & 0 \\ 0 & 0 & C \end{bmatrix}, \tag{2.6}$$

where $A, B,$ and C are now the MOI about the body's principal axes. Given the assumption that $\mathbf{I}$ is real, symmetric, and has been diagonalized, the inverse of this matrix is then the diagonal matrix of the reciprocals of the diagonal. Placing these assumptions in Eq. (2.5), the matrix-vector form of Euler's equations in the principal frame are

$$\begin{bmatrix} \dot{\omega}_1 \\ \dot{\omega}_2 \\ \dot{\omega}_3 \end{bmatrix} = -\begin{bmatrix} \frac{1}{A} & 0 & 0 \\ 0 & \frac{1}{B} & 0 \\ 0 & 0 & \frac{1}{C} \end{bmatrix} \begin{bmatrix} 0 & -\omega_3 & \omega_2 \\ \omega_3 & 0 & -\omega_1 \\ \omega_2 & \omega_1 & 0 \end{bmatrix} \begin{bmatrix} A & 0 & 0 \\ 0 & B & 0 \\ 0 & 0 & C \end{bmatrix} \begin{bmatrix} \omega_1 \\ \omega_2 \\ \omega_3 \end{bmatrix}. \tag{2.7}$$

13

Eq. (2.7) is now expabnded in three scalar equations and rearranged to represent the full coupled, nonlinear system of ODEs

$$\dot{\omega}_1 = \left(\frac{B-C}{A}\right)\omega_2\omega_3$$
$$\dot{\omega}_2 = \left(\frac{C-A}{B}\right)\omega_3\omega_1.$$
$$\dot{\omega}_3 = \left(\frac{A-B}{C}\right)\omega_1\omega_2$$

(2.8)

From Eq.(2.8), it is immediately apparent that for torque-free rigid body motion, one of the main driving system characteristics is the relative MOI ratios (the coefficients in the parentheses), versus the individual MOI values. Closed form solutions of Euler's torque-free equations of motion exist in closed-form for special cases. Consider the case of a rigid body that is isoinertial (e.g., a sphere), the rotational equations of motion would then integrate such that all angular velocities were constant values.

A particular solution presented now is the case of the axisymmetric body (e.g., a rectangular prism or cylinder) where A and B are equal. Placing this assumption in Eq. (2.8) produces

$$\dot{\omega}_1 = \left(1-\frac{C}{A}\right)\omega_2\omega_3$$
$$\dot{\omega}_2 = \left(\frac{C}{A}-1\right)\omega_3\omega_1.$$
$$\dot{\omega}_3 = 0$$

(2.9)

Immediately, ω_3 integrates as a constant, and the (ω_1, ω_2) time-history integrates as two harmonic oscillators. Hughes [7] provides the (ω_1, ω_2) solution as

$$\omega_1(t) = \omega_{1,0}\cos(\Omega t) + \omega_{2,0}\sin(\Omega t)$$
$$\omega_2(t) = \omega_{2,0}\cos(\Omega t) - \omega_{1,0}\sin(\Omega t)$$

(2.10)

where Ω is a relative spin rate given as

$$\Omega = \left(1-\frac{C}{A}\right)\omega_{3,0}.$$

(2.11)

14

Equations (2.10) and (2.11) present a closed-form solution for the torque-free axisymmetric body, but the mapping to an attitude parameterization still remains to be solved. In general, a spacecraft will not be precisely axisymmetric, nor be operating in an environment without external torques. The relations above serve to demonstrate the complexity in Euler's equations, and the strong dependence the system has on spacecraft MOI and coupling among states.

2.1.3 Attitude Parameterization.

Shuster provides a broad survey of attitude representations in [25]. This section will present key highlights from [25] while augmenting with additional sources. The parameters focused on in this section are those used in the course of this research, namely Euler angles, quaternions, and Rodrigues parameters. The purpose of this section is to familiarize the reader with the terminology, difficulties, and complexity of parameter choices with respect to this research. During this research, the author will primarily make use of the quaternion parameterization.

2.1.3.1 Euler Angles.

One of the more common attitude representations are Euler angles, which describe the orientation of reference frame $\mathfrak{B}$ relative to another frame $\mathfrak{N}$ through three consecutive rotations [26]. The successive rotations are typically defined as (X, Y, Z) where X, Y, and Z represent axes of rotation. For example, a popular set of Euler angles in astrodynamics is the $(3, 1, 3)$ set that defines the orientation of an orbital plane with respect to the central body inertial frame.

Although Euler angles are easier to visualize for small rotations and have the minimum dimension required to specify an attitude, there is a computational singularity associated with their use. Symmetric rotations of the form (X, Y, X) have geometric singularities when the second rotation is 0 or 2π, as the first and third rotation are indistinguishable. Additionally, asymmetric rotations of the form

(X, Y, Z) will have singularities when the second rotation is $\pm\pi/2$, as the first and third rotations are again indistinguishable. In order to fully describe the attitude using a single Euler angle parameterization, one must have *a priori* knowledge of the operational pointing of the spacecraft; otherwise, one may require the employment of two or more sets of Euler angles [25].

2.1.3.2 Quaternions.

Euler's principal rotation theorem implies that rather than three consecutive motions, the orientation of a rigid body can be described by a single rotation through a principal angle about a principal axis [26]. Given a rotation matrix $\mathbf{R}$ that describes frame $\mathfrak{B}$ relative to frame $\mathfrak{N}$, the principal rotation angle Φ can be found as

$$\cos\Phi = \frac{1}{2}\left(\text{tr}(\mathbf{R}) - 1\right) \tag{2.12}$$

where tr is the trace operator (i.e., the sum of the diagonal terms of a matrix) and the principal rotation axis $\hat{e}$ can be found from

$$\hat{e} = \frac{1}{2}\begin{pmatrix} R_{23} - R_{32} \\ R_{31} - R_{13} \\ R_{12} - R_{21} \end{pmatrix}. \tag{2.13}$$

Equations (2.12) and (2.13) can be used to describe an identical attitude as an Euler angle set but will have two solutions including a short and long rotation about the axis to the desired orientation [26], which is not troublesome for numerical propagation schemes. A popular coordinate that employs the principal rotation axis and angle is the quaternion, which is expressed following the notation of Crassidis et al. [24] as

$$\mathbf{q} = \begin{pmatrix} \boldsymbol{\varrho} \\ q_4 \end{pmatrix} \tag{2.14}$$

where

$$\boldsymbol{\varrho} = \begin{bmatrix} q_1 & q_2 & q_3 \end{bmatrix}^T = \hat{e}\sin\Phi/2 \tag{2.15}$$

and

$$q_4 = \cos \Phi/2. \qquad (2.16)$$

The quaternion is a four-dimensional vector but only specifies three degrees of freedom (DOF) due to a unity norm constraint such that

$$\mathbf{q}^T \mathbf{q} = 1. \qquad (2.17)$$

The most prominent advantage of the quaternion parameterization is the lack of singularities in the kinematics, and successive rotations can be accomplished using quaternion multiplication [24]. However, one negative in the use of quaternions is a lack of attitude visualization due to the four-dimensional parameterization. Mathematical treatment and derivation of quaternions that has been cited frequently in the astrodynamics community can be found in Shuster [25] and is not replicated here. A philosophical examination of the quaternion and its historical development can be found in [27].

2.1.3.3 Rodrigues Parameters.

The Classical Rodrigues Parameters (CRP) essentially reduce the four-dimensionality of the quaternions to a three-dimensional set by normalizing the quaternion vector by q_4 [26]. Schaub and Junkins describe the CRPs as stereographic projects of the four-dimensional quaternion unit sphere to a three-dimensional hyperplane orthogonal to q_4 [28]. Since the normalization is performed with $q_4 = \cos \Phi/2$ in the denominator, the CRPs are singular for $\Phi = \pm\pi$, which is a broader operational range than the $\pm\pi/2$ range associated with Euler angles. The Modified Rodrigues Parameters (MRP) are similar to the CRPs in that they are fundamentally derived from the quaternions; however, the normalization occurs with a division by $(1 + q_4)$, which moves the singularity to $\pm 2\pi$, doubling the rotational range of the MRPs compared to the CRPs [26].

17

2.1.4 Quaternion Dynamics.

Discussed previously in Section 2.1.3.2, quaternions avoid the Euler angle singularities and will be the attitude parameterization used most often in this research. The rotation matrix can be determined from the quaternion through the following relationship using Crassidis' notation [24], while an equivalent representation can be found in Schaub [26],

$$\mathbf{R}(\mathbf{q}) = \left(q_4^2 - ||\boldsymbol{\varrho}||^2\right) \mathbf{1}_{3\times 3} + 2\boldsymbol{\varrho}\boldsymbol{\varrho}^T - 2q_4\boldsymbol{\varrho}^\times = \boldsymbol{\Xi}^T(\mathbf{q})\boldsymbol{\Psi}(\mathbf{q}) \tag{2.18}$$

where the matrices $\boldsymbol{\Xi}$ and $\boldsymbol{\Psi}$ are expressed as

$$\begin{aligned}
\boldsymbol{\Xi}(\mathbf{q}) &= \begin{bmatrix} q_4\mathbf{1}_{3\times 3} + \boldsymbol{\varrho}^\times \\ \boldsymbol{\varrho}^T \end{bmatrix} \\
\boldsymbol{\Psi}(\mathbf{q}) &= \begin{bmatrix} q_4\mathbf{1}_{3\times 3} - \boldsymbol{\varrho}^\times \\ -\boldsymbol{\varrho}^T \end{bmatrix}.
\end{aligned} \tag{2.19}$$

Using this matrix notation, Crassidis gives the quaternion kinematics as [24]

$$\dot{\mathbf{q}} = \frac{1}{2}\boldsymbol{\Xi}(\mathbf{q})\boldsymbol{\omega} = \frac{1}{2}\boldsymbol{\Omega}(\boldsymbol{\omega})\mathbf{q} \tag{2.20}$$

where the $\boldsymbol{\Omega}$ matrix is given as

$$\boldsymbol{\Omega}(\boldsymbol{\omega}) = \begin{bmatrix} -\boldsymbol{\omega}^\times & \boldsymbol{\omega} \\ -\boldsymbol{\omega}^T & 0 \end{bmatrix}. \tag{2.21}$$

Expanding Eq. (2.20) in matrix-vector form, the following equivalent expressions are found [29]

$$\begin{bmatrix} \dot{q}_1 \\ \dot{q}_2 \\ \dot{q}_3 \\ \dot{q}_4 \end{bmatrix} = \frac{1}{2} \begin{bmatrix} q_4 & -q_3 & q_2 \\ q_3 & q_4 & -q_1 \\ -q_2 & q_1 & q_4 \\ -q_1 & -q_2 & -q_3 \end{bmatrix} \begin{bmatrix} \omega_1 \\ \omega_2 \\ \omega_3 \end{bmatrix} = \frac{1}{2} \begin{bmatrix} 0 & \omega_3 & -\omega_2 & \omega_1 \\ -\omega_3 & 0 & \omega_1 & \omega_2 \\ \omega_2 & -\omega_1 & 0 & \omega_3 \\ -\omega_1 & -\omega_2 & -\omega_3 & 0 \end{bmatrix} \begin{bmatrix} q_1 \\ q_2 \\ q_3 \\ q_4 \end{bmatrix}. \tag{2.22}$$

Notation will differ throughout the literature, as various authors may organize the quaternion structure differently. One immediate advantage of the quaternion kinematics is the far-right expression in Eq. (2.22) is linear in terms of the quaternions. This allows for a linear approximation via a matrix exponential that can be used in a Jacobian. Integration for the attitude history requires a seven state vector, where four states are the quaternions, and the remaining states are the angular velocities.

The four states in the quaternion vector should not be confused with additional degrees of freedom for the rotational system. Given three values of a quaternion representation, the fourth can be found by solving for the constraint. However, there will be an ambiguity in the sign of the fourth element which is representative of the same rotation, but differs only by a "long way" and a "short way" to achieve the orientation, which can be easily distinguished.

2.1.5 Time Varying Moment of Inertia Effects.

Rigidity of the body was a key assumption in Euler's equations, which implies the time derivative of the MOI tensor is zero. Structural changes such as boom extensions or antenna deployment, or internal phenomena such as fuel slosh, may introduce a time variance to the MOI. That is

$$\frac{d}{dt}(\mathbf{I}) \neq \mathbf{0}_{3\times 3}. \tag{2.23}$$

Re-examining the first principles in Euler's equations, use of the transport theorem becomes slightly more complicated. Rather than re-deriving using angular momentum conservation arguments, Thakur, et al. [30], present the attitude dynamics of the nonrigid body as

$$\mathbf{I}(t)\dot{\boldsymbol{\omega}} = -\dot{\mathbf{I}}(t)\boldsymbol{\omega} - \boldsymbol{\omega}^{\times}\mathbf{I}(t)\boldsymbol{\omega} + \boldsymbol{M}, \tag{2.24}$$

where the time dependency is explicitly stated for the MOI but is assumed on $\boldsymbol{\omega}$. Comparing to the rigid body Euler's equations Eq.(2.3), the time-varying MOI

19

increases the coupling in the system and, depending on the structural dynamics, is likely to increase the nonlinearity of the system as well. Because properties of the MOI tensor are now time-dependent, the eigenvalues will now evolve according to a given set of structural dynamics, and the corresponding principal axes may evolve as well. Analytical solutions to Euler's equations with a time-varying MOI quickly become cumbersome, complex, and difficult to generalize [31], and in some cases can result in chaotic attitude motion [32]. However, for particular spacecraft geometries, controlled variable MOI has been demonstrated as a means of possible attitude control [33]. Thakur et al. provide time dependent MOI models for appendage deployment and fuel loss resulting from maneuvering [30; 34].

2.2   An Overview of Kalman Filtering

The physical phenomena that are immediately available for observation and measurement are not always the variables or states of interest. In the current spacecraft attitude problem, control and pointing requirements make a state vector of attitude parameters desirable, but noisy physical measurements such as gyro rates and magnetometer observations may only be available. This section will introduce classical sequential estimation techniques in the sense of the Kalman filter and its variants.

2.2.1   Linear Kalman Filter.

This section will present a top-level discussion of the linear Kalman filter. The Kalman filter is often termed *the* optimal estimator [35] and minimizes the expected value of the mean squared error and the trace of the covariance matrix. As a sequential estimator, the filter is recursive and propagates the previous time step based on stochastic properties and system dynamics. Though not presented here, [36] presents a classical scheme for linear Kalman filtering applied to attitude dynamics.

An inherent assumption in the linear Kalman filter are disturbance inputs and measurement errors that are distributed with a zero-mean Gaussian distribution as well as stationary and uncorrelated processes [37]. The linear Kalman filter can be divided into three main phases:

1. Propagate State and Covariance Estimates

2. Compute Gain

3. Update State and Covariance Estimates

Note that the three phases are sometimes combined into two phases, where propagation and gain computation are consolidated. Following the development in Stengel [37], the initial phase propagates the state estimate from the previous iteration using the dynamic system model, while ignoring new measurement data. The covariance estimate is also propagated using the system dynamics and process noise in this initial phase. The second phase is the computation of the Kalman gain using *a priori* knowledge, while also ignoring the measurements. The final update phase uses innovations from the measurement residuals along with the Kalman gain to update the previously propagated state estimates.

The linear Kalman filter process will now be detailed mathematically using a modification of Stengel's notation in [37]. Proofs concerning the minimization of the mean squared error and derivation of the Kalman gain can be found in most stochastic estimation texts. Given a discrete time linear system that evolves with the dynamics

$$\mathbf{x}_k = \mathbf{\Phi}_{k-1}\mathbf{x}_{k-1} + \mathbf{\Gamma}_{k-1}\mathbf{u}_{k-1} + \mathbf{\Lambda}_{k-1}\mathbf{w}_{k-1} \tag{2.25}$$

where $\mathbf{\Phi}$ is a state transition matrix, and $\mathbf{\Gamma}$ and $\mathbf{\Lambda}$ operate, respectively, on the system input $\mathbf{u}$ and system disturbance $\mathbf{w}$. The covariances of the state, disturbance vector, and measurement noise are assumed as $\mathbf{P}$, $\boldsymbol{Q}$, and $\mathbf{R}$, respectively. The

following algorithm will use the notation that a superscript $-$ or $+$ is the propagated or updated value at a given time step, respectively, and assumes an understanding that the states are estimated values. The state and covariance propagation are given as

$$\begin{aligned}
\mathbf{x}_k^- &= \mathbf{\Phi}_{k-1}\mathbf{x}_{k-1}^+ + \mathbf{\Gamma}_{k-1}\mathbf{u}_{k-1} \\
\mathbf{P}_k^- &= \mathbf{\Phi}_{k-1}^-\mathbf{P}_{k-1}^+\mathbf{\Phi}_{k-1}^T + \mathbf{Q}_{k-1}
\end{aligned} \tag{2.26}$$

A measurement vector $\mathbf{y}_k$ is assumed to be expressed by the linear mapping

$$\mathbf{y}_k = \mathbf{H}_k\mathbf{x}_k + \mathbf{n}_k \quad , \tag{2.27}$$

where $\mathbf{H}$ is a known mapping from state to observation and $\mathbf{n}_k$ is uncorrelated zero-mean Gaussian measurement noise with covariance $\mathbf{R}$. The Kalman gain $\mathbf{K}$ can now be calculated as the matrix gain that minimizes the trace of the covariance $\mathbf{P}$

$$\mathbf{K}_k = \mathbf{P}_k^{-(-1)}\mathbf{H}_k^T\left[\mathbf{H}_k\mathbf{P}_k^-\mathbf{H}_k^T + \mathbf{R}_k\right]^{-1}. \tag{2.28}$$

The Kalman gain requires the inversion of a matrix that is of the order of the observation vector. Having the Kalman gain, the state and covariance can now be updated using measurement data

$$\begin{aligned}
\mathbf{x}_k^+ &= \mathbf{x}_k^- + \mathbf{K}_k\left[\mathbf{y}_k - \mathbf{H}_k\mathbf{x}_k^-\right] \\
\mathbf{P}_k^+ &= \left[\mathbf{P}_k^{-(-1)} + \mathbf{H}_k^T\mathbf{R}_k^{-1}\mathbf{H}_k\right]^{-1}
\end{aligned} \tag{2.29}$$

If $\boldsymbol{\nu}$ is a vector of residuals such that $\boldsymbol{\nu} = \mathbf{y}_k - \mathbf{H}_k\mathbf{x}_k^-$, then the state update in Eq.(2.29) becomes

$$\mathbf{x}_k^+ = \mathbf{x}_k^- + \mathbf{K}_k\boldsymbol{\nu}. \tag{2.30}$$

The $\left(\mathbf{H}_k^T\mathbf{R}_k^{-1}\mathbf{H}_k\right)$ relation in the covariance update serves to illustrate the problem with measurement perfection, in that zero measurement noise results in a singular matrix inversion and an invalid update. The Kalman gain is a function of the relation between the stochastic input and the measurement mapping and noise,

and does not depend on the actual measurements. The measurement residuals only impact the update to the state estimate.

This section presented the linear Kalman filter, which assumes the system dynamics can be propagated as a linear system. The following sections relax this assumption and present estimation methods for nonlinear systems.

2.2.2   *Extended Kalman Filter.*

The linear Kalman filter in Section 2.2.1 relied on linear system dynamics. However, most problems of interest in astrodynamics and spacecraft attitude are nonlinear in nature (for example, orbit and attitude determination). The Extended Kalman Filter (EKF) is best applied to nonlinear estimation problems by linearizing the system dynamics about the most current estimate. The EKF typically has a longer computation time than the linear Kalman filter as a Jacobian and state transition matrix must be computed at each time step [38].

The EKF follows a nearly similar structure to the linear Kalman filter with slight differences. The propagation of the state and covariance requires integration of the $\mathbf{\Phi}(t)$ matrix, or State Transition Matrix (STM). The differential equation for the STM is given as

$$\frac{d}{dt}\mathbf{\Phi}(t) = \mathbf{A}\mathbf{\Phi}(t) = \frac{\partial \mathbf{f}}{\partial \mathbf{x}}\mathbf{\Phi}(t) \tag{2.31}$$

with the initial condition on the $\mathbf{\Phi}$ matrix as identity. The matrix $\mathbf{A}$ is the Jacobian of the system dynamics with respect to the state and requires evaluation at the current estimate. In dynamics regimes where nonlinearities are present, there is potential for the Jacobian to be a poor approximation of the system and contribute to filter divergence [38].

2.2.3   *Unscented Kalman Filter.*

As the governing equations for attitude dynamics are nonlinear, an EKF is more desirable over a linear Kalman filter. However, the EKF does have some drawbacks,

the most paramount being the loss of higher-order terms in the system dynamics [39] and often complicated Jacobians in the state-measurement relations. Julier and Uhlmann introduced the Unscented Kalman Filter (UKF) in [40] to avoid the linearization inherent in the EKF.

The system model for the UKF formulation assumes the form

$$\mathbf{x}_{k+1} = \mathbf{f}(\mathbf{x}_k, t_k) + \mathbf{w}_k$$
$$\mathbf{y}_k = \mathbf{h}(\mathbf{x}, t_k) + \mathbf{v}_k$$

(2.32)

where $\mathbf{f}$ and $\mathbf{h}$ are arbitrary nonlinear functions for the dynamics and measurements, respectively. The filter initializes the state estimate and covariance and then performs the *unscented transform*. The unscented transform assumes that a Gaussian distribution is easier to approximate than an arbitrary nonlinear function [40]. A set of sigma points $\boldsymbol{\chi}$ are deterministically selected such that their mean and covariance match that of the state. The UKF can be described using phases similar to the three phases of the linear Kalman filter [39]. The sigma points are calculated from *a priori* state statistics. A *posterior* mean and covariance are then determined from weighted combinations of the sigma points. A Kalman gain is found using the cross-correlation and innovation covariance matrices. The new state estimate is then found using traditional Kalman update equations.

Rather than discussing the UKF routine in textual form, Algorithm 1, provided at the end of this chapter, summarizes and outlines the mathematical steps for the unscented filter from [39; 40]. The (κ, α, β) parameters are heuristically chosen to allow tuning, but the literature provides some rules of thumb exist for tuning these parameters [40]. The α parameter controls the spread of the sigma points, β essentially controls the admission of prior knowledge in the filter, and κ is a scaling parameter [41]. The UKF is presented here in a pseudo-classical form, but the

unscented filter used in this research is that of Crassidis, et al., [16] and will be discussed later in Chapter 3.

2.3   Survey on Attitude Estimation

The purpose of this section is to discuss with the reader a variety of estimation methods available for satellite attitude determination. This brief survey is intended as a top-level discussion that is important in discussing this research. Chapter 3 relies on a development of a UKF, Chapter 4 determines attitude by the single-frame formulation, and Chapter 5 estimates MOI values that can be used to propagate dynamics in Chapter 3's filters. The author refers the reader to [24] for a thorough and mathematically rigorous survey of attitude estimation methods.

To define orientation in a three-dimensional space, one needs three independent parameters. A single vector measurement will provide two independent parameters, as a unit vector constraint removes a DOF making the problem underdetermined, while two vector measurements will provide at least four quantites, making the problem overdetermined [22]. Attitude estimation techniques can be described as deterministic, where two or more measurements are used to determine the attitude, or as stochastic, where observations are used to recursively estimate the attitude with statistical methods [22].

The following section describes commonly used attitude estimation techniques found in the literature and used in this research. The presented survey will minimize the use of mathematical descriptions and will provide textual discussion. A thorough review of early estimation techniques to include linear Kalman filtering can be found in [36].

2.3.1   Extended Kalman Filter.

The EKF is portrayed as the "workhorse" of satellite attitude determination [24], where a linearization of the nonlinear system is performed about the current best state

25

estimate. This linearization requires derivation and calculation of the Jacobian which could be computationally expensive depending on the system. Minimal representation EKFs have been used to estimate Rodrigues parameters and, consequently, MRPs [42]; however, this EKF realization has not been widely implemented [24]. The multiplicative EKF has been used to estimate attitude error vectors using quaternion multiplication to maintain the unit norm constraint on the quaternions, and several realizations exist depending on the attitude parameterization [24; 36]. A backwards smoother can also be applied to the EKF by minimizing a loss function in what is posed as a Maximum a Posteriori (MAP) estimation problem [24; 43]; however, the backwards smoother comes with a greater computational cost than other estimators.

2.3.2 *Solutions to Wahba's Problem.*

The previous section discussed the EKF, an attitude estimator that takes advantage of the system dynamics to propagate and update state and covariance estimates. This section focuses on the single frame estimation problem, where the objective is to find the rotation matrix that minimizes a particular cost function composed of unit vector measurements in two different reference frames. This section will provide a broad discussion on the single frame estimation problem, while Chapter 4 will provide a mathematical development of numerical solution methods and discuss more advanced solution techniques.

The attitude determination problem is either underdetermined or overdetermined [22]. This formulation leads to computing a rotation matrix (attitude) to minimize a loss (cost) function of these measurements. One loss function is often defined as Wahba's problem [20; 22; 24], and is given as

$$J\left(\mathbf{R}^{bi}\right) = \frac{1}{2} \sum_{k=1}^{N} w_k \left\|\mathbf{v}_{kb} - \mathbf{R}^{bi}\mathbf{v}_{ki}\right\|^2, \qquad (2.33)$$

where J is the loss function, k is the index for the N observations, w_k is the observation weight, $\mathbf{v}_{kb}$ is k^{th} vector of body frame components, $\mathbf{v}_{ki}$ is the kth vector of components

in the inertial frame, and $\mathbf{R}^{bi}$ is the rotation matrix to be found to minimize J. The original problem posed by Wahba posited the cost function slightly different as

$$J\left(\mathbf{R}^{bi}\right) = \frac{1}{2}\sum_{k=1}^{N}\left\|\mathbf{v}_{kb} - \mathbf{R}^{bi}\mathbf{v}_{ki}\right\|^{2}, \tag{2.34}$$

with the only difference between Eqs. (2.33) and (2.34) being the presences of sensor weights.

There are three commonly referenced solutions to this problem: (1) numerical minimization; (2) solution in the eigenspace known as the q-method; and (3) an eigenspace approximation method [23]. We will now discuss each in the order listed.

The numerical minimization problem typically seeks to minimize Wahba's problem directly by numerically solving for the optimal rotation matrix. Although the rotation matrix has nine components, the number of constraints require only three numbers to solve for, and the rotation matrix can be parameterized by these three numbers (e.g., Euler angles) [22]. This minimization generally involves the standard appendage of Lagrange multipliers with the unity norm quaternion constraint, a Jacobian, and a Newton-Raphson type iteration [22].

Davenport's q-method [21; 22] rewrites Wahba's minimization problem (min $J(\mathbf{R}^{bi})$) as a maximization of a gain function (max $g(\mathbf{q})$), where quaternions are the independent variables. Appending the quaternion norm constraint leads to an eigenvalue problem, where the eigenvector corresponds to the maximum eigenvalue [21; 22].

Shuster expanded Davenport's q-method with QUEST in an attempt to decrease the computational time required for eigenspace computations [23]. Rearranging the gain function derived from Wahba's problem, an initial guess for the optimal eigenvalue can be approximated as the sum of the weights w_k, and the corresponding eigenvector can be iteratively determined. Often, very few iterations are required for the QUEST solution to converge [23; 24]. However, when noise is present, more iterations may be required and convergence to the non-maximum eigenvalue is a

possibility discovered in [44] and discussed more in this research in Chapter 4. While less robust than the q-method, QUEST has proven reliable and computationally efficient [24]. Psiaki modified Shuster's work with Extended QUEST [45] to allow for the estimation of other states (e.g., gyro bias) by modifying the cost function and implementing information filtering algorithms. As mentioned earlier, this section was presented as part of this literature review as a primer. Chapter 4 will provide a more in-depth development of the problem. Next, we will discuss the recursive UKF used in Chapter 3.

2.3.3   *Unscented Kalman Filter for Attitude Estimation.*

Estimation methods that use the EKF are inherently reliant upon linearization of the nonlinear system about the most current state estimate and neglecting higher order terms [39]. The UKF is an extension of the linear Kalman filter that attempts to circumvent short-comings of the EKF, such as reducing linearization errors [39]. The UKF assumes the fundamental premise that a Gaussian distribution is easier to approximate than arbitrary nonlinear functions [24]. The UKF approximates the state as a Gaussian random variable with a sample of sigma points based on the current state estimate and covariance. The sigma points are propagated using the system dynamics, and the *a posteriori* state mean and covariance are determined by using the UKF. The UKF retains second-order accuracy over the EKF's first-order [24; 39]. Other advantages provided by the UKF over the EKF are its applicability to nonlinear functions while avoiding the creation or computation of the Jacobian matrix [16]. This allows an immediate extension to complex measurement-state relations without the need to compute the Jacobian.

For the attitude estimation problem, numerical error in direct application of the UKF yields a quaternion estimate that often violates the unit-norm constraint [24]. Vandyke, et al. [39], implement the three-element error quaternion in the state and

28

solve for the fourth component using the unit norm constraint. Crassidis, et al. [24], developed the USQUE algorithm where intermittent conversions are made between Rodrigues parameters while also estimating gyro biases from the measurements [24]. As the primary estimation routines employed in the adaptive estimation portion of this research, the UKF algorithm and USQUE methods will be discussed in more detail in Chapter 3.

2.3.4 Miscellaneous Estimation Techniques.

Although this section has surveyed some of the more common attitude estimation techniques, there are some less employed techniques worth mentioning. As an alternative to the EKF, the two-step optimal attitude estimation performs time- and measurement-updates to first-step estimates, while next minimizing a cost function for the orthogonal attitude matrix [24].

Other approaches worth mentioning are particle filters and observers. Particle filters form a broad field of estimators that are sub-optimal and use Monte Carlo simulations to propagate and updates particles based off sequential importance sampling or resampling. Nonlinear observers can also be applied when there is perfect knowledge of the observations [24; 46].

2.4 Survey on Adaptive Estimation Techniques

2.4.1 Adaptive Estimation in General.

Estimation routines must be equipped to account for modeling and measurement errors. Estimation confidence can be represented using statistical methods, such as the covariance to correlate estimation error among the states. Vallado [38], Kay [47], and Stengel [37] detail the fundamentals of estimation theory and its applications to multiple engineering fields. Common optimal estimation techniques assume that errors and noise are distributed in the Gaussian sense, and, do not easily allow for changes in the system dynamics. Multiple model adaptive estimation (MMAE)

approaches, though often referred to as sub-optimal, deviate from traditional filtering techniques and allow for the inclusion of non-Gaussian noise and changes in the dynamical modes of the system [37; 48].

Consider an observable system where there is uncertainty in some system parameter. MMAE generalizes the principle of defining hypotheses based on corresponding system characteristics (e.g., state transition matrices, measurement noise, initial estimates), and generating a filter based on each hypothesis. The filter that provides the "best" state estimate could then be used to identify the uncertain parameter and likely operational mode [37]. An example of parameter estimation in a nonlinear system can be found in Appendix C, where the author provides a nominal scenario of a re-entering satellite being tracked by ground radar with the objective of estimating the satellite's ballistic coefficient.

Li and Jilkov provide an exhaustive survey of multiple model adaptive estimation methods in [49]. Generally speaking, an adaptive estimation scheme can be divided into four main parts:

1. *Model-set determination*: The selection and design of the models or parameters included in the elemental filter bank.

2. *Cooperation strategy*: The interaction among the various filters in the bank, to include the pruning or merging of models.

3. *Conditional filtering*: The recursive estimation process based on an assumed probability distribution.

4. *Output processing*: The combination of individual filter estimates along with conditional filtering outputs for the overall state and covariance estimate.

Figure 2.1 provides a visualization of Li's interpretation of the the general adaptive estimation algorithm flow [49]. Along with the four generalized segments of an

adaptive estimation scheme, multiple model methods can also be viewed as having evolved through three distinct generations of algorithms [49; 50]. The first generation is the classical form most heavily used in this research. Pioneers of the first generation include Magill [51; 52], Lainiotis [53], and Maybeck [54]. This first generation used limited cooperation strategies and did not include pruning or merging. The ground radar target tracking problem affected the rise of the second generation of multiple-model algorithms, wherein there is interaction among the filters in the bank [49; 55], but often requires a reformulation of the problem as a Markov system with a specific probability transition matrix. The third and most recent generation incorporates cooperation among the filters in the bank, where poor performing models are removed (or pruned), and similar models are merged. This variable structure adaptive estimation effort has been led by Li et al. [49].

The following sections will examine specifically how adaptive estimation schemes have been applied to the areas of attitude dynamics and orbital mechanics.

2.4.2   Applications of Adaptive Estimation to Attitude Dynamics.

Rupp, et al. employed a bank of EKFs inside a MMAE architecture to detect sensor and actuator faults [56]. In this bank of filters, each filter represents a system model for a potential fault pattern. Simulation results for an aircraft aileron problem indicated that the MMAE architecture developed is capable of detecting faults [56]. In a similar set-up, Tudoroiu et al. employ a interactive bank of UKFs to detect faults in reaction wheel components of a spacecraft's Attitude Determination and Control System (ADCS) [57]. Their estimation algorithm is able to detect single, decoupled faulty modes and multiple faults including unexpected changes in the power supply bus and motor torque gain [57].

Bolandi and Saberi use a MMAE construct to tackle the attitude estimation problem using star sensors with unknown noise levels [58]. The authors assume a
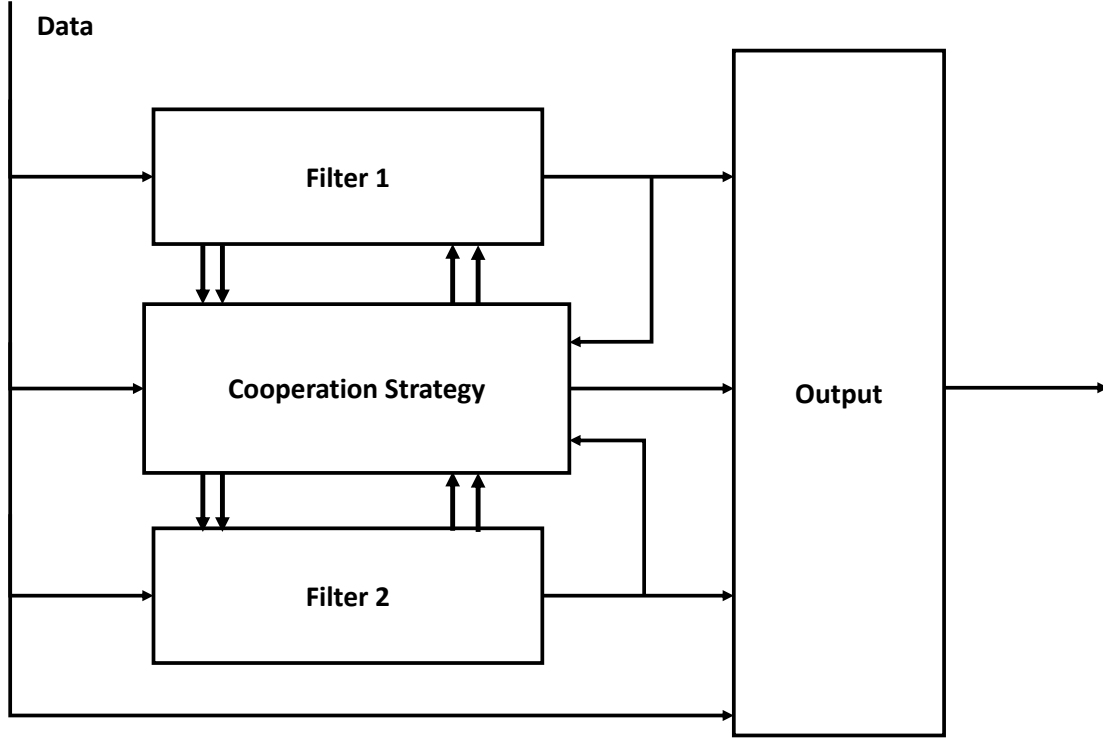
Figure 2.1: Recreation of Li and Jilkov's interpretation of the general multiple model algorithm with two filters.

rigid spacecraft with a pyramid configuration of four reaction-wheels and use eight models to investigate high and low noise values for attitude estimation about three axes. Using this construct, the authors are able to estimate attitude with accuracy on the order of 10^{-3} degrees during three slewing maneuvers [58].

Soken, et al. provided an in-orbit routine to estimate time-varying residual magnetic moments using an adaptive Kalman filter in [59]. Soken's filter adapts the level of covariance to converge on Residual Magnetic Moment (RMM) estimates following instantaneous changes [59]. Soken, et al., later sought a more autonomous adaptive algorithm and proposed a MMAE technique to estimate the RMM for small satellites [60]. Soken's MMAE routine constructs a bank of EKFs assuming different

32

levels of process noise and RMM estimates, and also proposes a novel likelihood function that combines filter agility with steady state behavior [60].

Linares employed MMAE to characterize the behavior RSOs using light curve data in [61]. A bank of multiple UKFs is used in the construct where each filter assumes a different control profile. RSOs are classified as intact or fragments, passive or active, and further characterized as spin stabilized, sun pointing, or Nadir pointing [61] based on a control profile. The coupling between RSO attitude and torques from non-conservative forces is exploited in [9], where light curve and orbit determination observations are taken from ground sites and propagated using an UKF. The attitude couplings enters the EOMs through a perturbing solar radiation pressure, and the MMAE filter bank hypotheses assume different RSO shapes to estimate to area-to-mass ratio for an object in GEO. A memoryless form of MMAE called "adaptive likelihood mixtures" is also introduced in [9] and is shown to detect abrupt data changes faster than other adaptive estimation methods. A comprehensive method is shown in [62] fusing astrometric and photometric data to determine RSO shape, attitude, and orbital states where two scenarios are successfully tested in the MMAE, one where the true system model is in the bank, and the other where the true model is a combination of models in the bank.

Lam and Crassidis developed an attitude determination system mixing various EKF models with different state dimensions and showed the MMAE scheme can reduce the effects of gyroscopic scale factors and misalignments compared to traditional EKF schemes [63]. In [64], the same authors expand upon the work in [63] to demonstrate the fusion of multiple sensor sources at differing sampling frequencies.

Hess et al. [19] investigated the application of MMAE to a satellite with time-varying MOI using on-board sensors including a three-axis magnetometer and gyroscopes. The work in [19] presented the preliminary results of the research

discussed in Chapter 3 of this dissertation. Besides the work presented in [19], adaptive estimation has not, to the knowledge of this author after an extensive literature review, been previously applied to the attitude estimation of a spacecraft with time-varying MOI.

2.4.3 Applications of Adaptive Estimation to Orbital Mechanics.

Recent work has shown some success in using MMAE to perform spacecraft translational maneuver detection [12–15]. Lee and Hwang [14] examine planar two-body Keplerian dynamics and characterize maneuvers by changes in classical orbital elements from ground observations. A bank of EKFs is used assuming different maneuvers in the system model, and numerical simulations demonstrated success in detecting maneuvers. In [15], Lee and Hwang extend the work in [14] by developing an adaptive estimation scheme with state-dependent probability transition models, and successfully demonstrated the algorithm on a maneuvering geostationary satellite. Goff et al. [13] investigated translational maneuver detection using both Interacting Multiple Model (IMM) and variable state dimension filters. The translational spacecraft state is tracked using ground observations, and once residual-based heuristic thresholds are exceeded, the state is extended to include the thrust vector as additional states. Two thresholds are recommended: (1) a filter-smoother consistency test used in post-processing; and (2) a maneuver detection threshold, similar to the Mahalanobis distance, used for more real-time detection based on heuristics. The IMM construct assumes various levels of process noise, which, when combined with covariance inflation, allows for success in maneuver detection and thrust estimation [13].

2.5 Survey on Spacecraft Moment of Inertia Estimation

The rotational dynamics of a rigid body are primarily a function of the current rotational state, external torques, and the MOI tensor. Pre-flight, the MOI is

estimated, but there will inevitably be changes in the MOI due to the space environment and operational needs. This section will briefly detail some of the open literature that examines MOI estimation.

Tanygin and Williams [65] demonstrate successful estimation of both the MOI and the spacecraft center of mass using coasting maneuvers and energy conservation techniques. The work by Tanygin and Williams was also experimentally verified on the STS-64 mission (September 1994) [65]. Similarly, conservation of angular momentum arguments are used to develop in-flight MOI estimation for the Cassini spacecraft using least-squares estimates when slewing telemetry is available [66]. The approach used in [66] builds upon Peck's work in [67]. Using angular momentum principles, Peck removed the need to determine the uncertainty in energy dissipation [66], [67]. Norman, Peck, and O'Shaughnessy [68] combine both angular momentum and energy conservation principles for on-board MOI and reaction wheel alignment estimation.

Thakur, Srikant, and Akella derive an adaptive attitude-tracking controller to estimate and compensate for time-variance in the MOI tensor [30]. In [30] and [34], Thakur, et al., also provide mathematical insight into the time-varying MOI that will be discussed in Chapter 3. A passive adaptive control scheme is also introduced in [46] assuming a constant MOI tensor by selecting a desired angular velocity for persistent excitation of the estimator. The persistency of excitation (PE) condition is found to promote exponential convergence of the MOI estimates and drives the tracking error to zero.

VanDyke, et al., employ a dual UKF to estimate both the spacecraft attitude and MOI [39]. The MOI parameter estimation is performed within a loop at each iteration, where the current state estimate is used to determine the MOI parameters, which are then fed back into the state estimator for the next iteration. Vandyke, et al., compare their results to a baseline EKF algorithm, showing that the UKF

consistently outperforms the EKF [39]. Further, the EKF demonstrated a tendency to diverge with poor initial MOI estimates. VanDyke's work assumed the MOI as constant parameters to be estimated using the dual UKF. Additionally, Bordany et al. [69] as well as Ferguson [70] approached the MOI estimation problem by using an EKF to estimate mass properties and thruster characteristics.

Wright developed a methodology to estimate the full MOI tensor using maneuver based estimation to approximate the MOI ellipsoid [71]. Wright implements a least-squares cost function on an over-determined set of measurements and minimizes the cost function by a static optimization method [71]. Wright's methodology was implemented on a terrestrial-based attitude simulator [72; 73] with significant MOI estimate improvements over previous methodologies [71].

Sheinfeld and Rock [74] propose a framework to estimate the MOI of a tumbling rigid body. The motivation in [74] is to incorporate the MOI estimate into the dynamics for the capture of the tumbling spacecraft. Sheinfeld's algorithm essentially becomes an overdetermined least-squares problem. Sheinfeld and Rock also made an important note that in the torque-free formulation of the problem, only the relative MOI ratios can be recovered, and scale factors must be determined by exploiting known torques and forces [74].

2.6 Survey on Heuristic Optimization

Heuristic optimization, or metaheuristics, is a generalized term for a subfield of stochastic optimization, wherein a degree of randomness is exploited and employed to some extent in the search for optimality [75]. This section is not intended to survey, either conceptually or mathematically, the entire field of metaheuristics, but rather focus on the two specific routines employed in Chapter 4 of this research. The justification in this narrow focus can be found in Luke's textbook [75], in which his list of detailed algorithms numbers 137 in total. The author refers the reader to [75; 76]

for an exhaustive survey of the field. Rather, this presented research attempts to solve the single frame attitude problem by using heuristic optimization rather than a classical method like Quaternion Estimation (QUEST), thereby avoiding singularities and exploiting inventive optimization and estimation routines.

2.6.1 Particle Swarm Optimization.

Eberhart and Kennedy [77] developed the metaheuristic PSO algorithm. The algorithm duplicates the random and unpredictable motion of a flock of birds gathering food [78]. An initial swarm is selected by random assignment of position and velocity vectors in the solution space to various particles. In this algorithm, position refers to the design variables through which the cost is being optimized, and velocity refers to updates to the design variables. An individual particle's position and velocity solution are updated by three mechanisms [78]:

1. *Inertial update*: an update proportional to the particle's own velocity in the previous iteration.

2. *Cognitive update*: an update to a specific particle that is directed toward the best position known to that particle.

3. *Social update*: an update to a specific particle that is directed toward the best position known to all particles in the swarm.

Mathematically, this update to a particle p's position $\mathbf{X}_p$ at the sth iteration is described using the global PSO version as [79]:

$$\mathbf{X}_p(s) = \mathbf{X}_p(s-1) + \mathbf{V}_p(s) \tag{2.35}$$

where $\mathbf{V}_p(s)$ is the velocity calculated from the swarm at iteration s as

$$\mathbf{V}_p(s) = \chi\left[\mathbf{V}_p(s-1) + c_1 z_1\left(\mathbf{p}_{\text{best}} - \mathbf{X}_p(s-1)\right) + c_2 z_2\left(\mathbf{g}_{\text{best}} - \mathbf{X}_p(s-1)\right)\right], \tag{2.36}$$

where c_1 is the cognitive parameter, c_2 is the social parameter, $\mathbf{p}_{\text{best}}$ is the best position visited by the individual particle, $\mathbf{g}_{\text{best}}$ is the best position visited by the entire swarm, z_1 and z_2 are uniformly distributed random numbers between zero and one, and χ is a constriction factor given as

$$\chi = \frac{2}{1 - \phi - \sqrt{\phi^2 - 4\phi}} \tag{2.37}$$

with $\phi = c_1 + c_2$. The three updates are used to iterate on the swarm until the a cost function differential is below a certain threshold, or through some similar tolerance check. Work has been done to reduce the tendency of the PSO algorithm to become stuck in local extrema, and to balance the weights of global and local searches [78; 80; 81]. Moreso, constrained optimization problems can be handled by the use of penalty functions, which assign additional costs to constraint violations [79; 82]. The PSO shares with other heuristic algorithms the ability to handle arbitrary cost functions and nonlinear systems, but provides for a less complex implementation [83].

Particle swarm optimization has seen applications in both spacecraft trajectory design as well as attitude control. In [78], Pontani and Conway use PSO to find optimal low-thrust planetary transfers. Pontani and Conway continue in [84] to use PSO to investigate optimal rendezvous trajectories in the Hill frame for relative satellite motion. Showalter extends the application of PSO to trajectory design to optimize spacecraft responsive theater maneuvers [79; 82]. Rahimi et al. [85] applied PSO to the spacecraft reentry problem to determine initial conditions to minimize total applied heating to the spacecraft. Hu et al. [86] applied and modified the PSO algorithm to optimize parameters in a flexible satellite attitude controller. Additionally, heuristic algorithms such as PSO have been employed to determine optimal Proportional Integral Derivative (PID) controller gain settings [87].

2.6.2 Genetic Algorithms.

The genetic algorithm was initially developed by Holland [88] while modeling natural adaptive processes [82]. An initial population is generated from some random distribution of the solution space, and future generations are generated by combinations of previous parent generations. The primary two methods of combination are selection and reproduction. Selection uses some problem specific metric to evaluate which current population members are used as generation parents, choosing the most optimal members. Reproduction involves mutation and crossover, where in mutation small changes are made to individuals, and in crossover pieces of parents solutions are combined [82].

The employment of genetic algorithms has seen success when there are a large number of design variables [89; 90] and multiple optimization objectives [91]. Mosher proposed the use of genetic algorithms in automating the search space of conceptual satellite design [90], and found that the use of evolutionary heuristic algorithms can expedite the design process. In [89] and [92] Thompson et al. implement a GA to design a constellation from a systems engineering perspective to design a disaggregated weather system with multiple objectives, constraints, and design variables. In [91], Diniz employed the GA to design a navigation satellite constellation minimizing dilution of precision and financial cost, while Abbate designed an imagery constellation with a GA in [93].

The heuristic genetic algorithm has also been applied to singular spacecraft orbit and trajectory design. Abdelkhalik and Mortari [94] used the GA solution as a warm start to classical optimization methods to determine an optimal orbit for given targets and imaging capabilities. Kim and Spencer [95] employ a GA to determine optimal satellite rendezvous conditions.

Alfriend et al. [96] posed the geosynchronous satellite servicing problem as a traveling salesman problem. The *traveling salesman problem* is a classical problem in mathematics determining the optimal path for a salesman to take given a certain number of cities to travel among. Alfriend et al. found the optimal geosynchronous servicing route by brute-force permutations on the possible servicing routes [96]. Zhou et al. later used a genetic algorithm to determine the optimal servicing route, noting that as the number of satellites to service increases, the approach in [96] becomes numerically exhaustive when compared to the GA search pattern.

2.6.3 Conclusions.

In this chapter, we discussed a broad background on topics of importance to the presented research. This chapter discussed classical rigid body dynamics, and expanded on the state of the art of attitude estimation, adaptive estimation, and heuristic optimization. Next, Chapters 3, 4, and 5 each present the three distinct components of this dissertation. One will notice immediately some repetition due to the dissertation format selected where Chapters 3, 4, and 5 stand as complete discussions to themselves, ultimately becoming articles.

Algorithm 1: Unscented Kalman Filter algorithm

Given $\hat{\mathbf{x}}_{k-1}^+$ and covariance $\mathbf{P}_{xx,k-1}^+$ estimates at epoch time t_{k-1}

1. Calculate sigma points from *a priori* mean and covariance:

$$\boldsymbol{\chi}_{k-1} = \left[\hat{\mathbf{x}}_{k-1}^+ \quad \hat{\mathbf{x}}_{k-1}^+ + \left(\sqrt{(n+\kappa)\,\mathbf{P}_{xx,k-1}^+} \right)_i \quad \hat{\mathbf{x}}_{k-1}^+ - \left(\sqrt{(n+\kappa)\,\mathbf{P}_{xx,k-1}^+} \right)_i \right]$$

using Cholesky decomposition and $(.)_i$ indicates row or column of the matrix.

2. Calculate weights, where α, β, κ are heuristically tuned:

$$W_0^m = \frac{\kappa}{n+\kappa}$$

$$W_0^c = \frac{\kappa}{n+\kappa} + 1 - \alpha^2 + \beta$$

$$W_i^m = W_i^c = \frac{1}{2(n+\kappa)} \text{ for } i = 1, ..2n$$

3. Propagate sigma points individually using nonlinear state equations:

$$\boldsymbol{\chi}_{k|k-1}^{(i)} = \mathbf{f}\left(\boldsymbol{\chi}_{k-1}^{(i)} \right)$$

4. Calculate propagated state:

$$\hat{\bar{\mathbf{x}}}_k^- = \sum_{i=0}^{2n} W_i^m \boldsymbol{\chi}_{k|k-1}^{(i)}$$

5. Calculate propagated covariance:

$$\mathbf{P}_{xx,k}^- = \sum_{i=0}^{2n} W_i^c \left(\boldsymbol{\chi}_{k|k-1}^{(i)} - \hat{\bar{\mathbf{x}}}_k^- \right) \left(\boldsymbol{\chi}_{k|k-1}^{(i)} - \hat{\bar{\mathbf{x}}}_k^- \right)^T + \boldsymbol{Q}_{k-1}$$

6. Transform sigma points to observations using nonlinear measurement transformation $h()$:

$$\boldsymbol{\Gamma}_{k|k-1}^{(i)} = \mathbf{h}\left(\boldsymbol{\chi}_{k|k-1}^{(i)} \right)$$

7. Calculate expected measurement from sigma points

$$\hat{\mathbf{Y}}_k = \sum_{i=0}^{2n} W_i^m \boldsymbol{\Gamma}_{k|k-1}^{(i)}$$

8. Calculate the predicted observation covariance:

$$\mathbf{P}_{yy} = \sum_{i=0}^{2n} W_i^c \left(\boldsymbol{\Gamma}_{k|k-1}^{(i)} - \hat{\mathbf{Y}}_k = \right) \left(\boldsymbol{\Gamma}_{k|k-1}^{(i)} - \hat{\mathbf{Y}}_k \right)^T + \mathbf{R}_k$$

9. Calculate the predicted (innovation) cross covariance:

$$\mathbf{P}_{xy} = \sum_{i=0}^{2n} W_i^c \left(\boldsymbol{\chi}_{k|k-1}^{(i)} - \hat{\bar{\mathbf{x}}}_k^- \right) \left(\boldsymbol{\Gamma}_{k|k-1}^{(i)} - \hat{\mathbf{Y}}_k \right)^T$$

10. Update the estimate with traditional linear Kalman filter update equations:

$$\boldsymbol{\nu} = \mathbf{Y} - \hat{\mathbf{Y}}_k$$

$$\mathbf{K}_k = \mathbf{P}_{xy} \mathbf{P}_{yy}^{-1}$$

$$\hat{\mathbf{x}}_k^+ = \hat{\bar{\mathbf{x}}}_k^- + \mathbf{K}_k \boldsymbol{\nu}$$

$$\mathbf{P}_{xx,k}^+ = \mathbf{P}_{xx,k}^- - \mathbf{K}_k \mathbf{P}_{yy} \mathbf{K}_k^T$$

III. Adaptive Estimation of Nonlinear Spacecraft Attitude Dynamics with Time Varying Moments of Inertia

In this chapter, a series of scenarios were constructed to evaluate the performance of various adaptive estimation routines in identifying and estimating a spacecraft's time varying MOI. To the extent of the author's knowledge, this effort is the first application of adaptive estimation to the case of a variable spacecraft MOI using streaming attitude data. A methodology is developed to detect sudden MOI changes using a bank of Unscented Kalman Filters as a numerical testbed for future real-world implementation. A hybrid adaptive estimation algorithm to detect sudden parameter changes in nonlinear systems is developed combining two state of the art routines. As previously mentioned, the reader may notice repetition between the presented motivation and background. Section 3.2 refers the reader to relevant background material in Chapter 2. New material is presented beginning with the methodology in Section 3.3.

3.1 Introduction and Motivation

The NSSS highlights the vital role of space in ISR, power projection, diplomacy, and military operations [1]. Further, the NSSS details the increasingly *congested, contested*, and *competitive* space environment and the need to maintain the strategic national security advantages afforded by space. The growing global domain of space operations requires an improvement in shared SSA, and the NSSS recommends the US invest its knowledge base to foster SSA cooperation while protecting US and partner space capabilities [1].

The SSA mission is becoming increasingly difficult when considering the trend towards smaller space vehicles [3], discussion of disaggregated mission sets [4], as well as debris created from collisions [5], ASAT testing [1], and catastrophic events.

Further difficulties facing the SSA mission are the methods by which the JSpOC tracks and propagates RSOs. In 2011, AFSPC tasked the NRC to "assess (their) astrodynamics standards...and their effectiveness..."[6]. Nongravitational effects (e.g., solar radiation pressure, atmospheric drag) perturb the nominal Keplerian motion of an object with a wide range of effects depending on the position and orientation of the object. AFSPC employs a number of astrodynamics algorithms to generate ephemerides with varying degrees of accuracy and inclusions of perturbing forces, which directly effects computational time. The analytic models in the more commonly known SGP4 and SP numerical integration techniques do not take into account certain key satellite properties, such as attitude and shape, and additions of these states could improve orbit predictions [6].

The NRC found that for the nonlinear governing equations in astrodynamics, advanced estimation techniques should be employed to characterize state estimates and their uncertainties [6]. Space is a data-sparse environment, and, consequently, convergence times for state estimators and filters can be of considerable duration. Multiple model filters have been shown to be capable of converging on state estimates with limited data [6; 62]. Moreover, multiple model techniques have also demonstrated operational efficacy in estimating the states of maneuvering missiles and aircraft where sudden changes in dynamics are experienced [6; 10; 11]. Sudden dynamical changes are not always deterministic. Unplanned changes to spacecraft's structure can result from debris, external actors, or hardware faults. For example, the recent 2016 loss of the JAXA X-ray science satellite *Hitomi* has been attributed to human error, possible payload deployment faults, and attitude control logic malfunction [8]. Adaptive estimation techniques applied to the available streaming attitude data could have potentially identified the fault through various filters assuming different MOI modes.

3.2 Background

The current research on adaptive estimation examines the fields of spacecraft attitude dynamics, time-varying moments of inertia, attitude estimation, multiple model adaptive estimation, and stochastic filtering. For background information, the reader is referred to Section 2.1 regarding attitude dynamics, Section 2.1.5 for time-varying moments of inertia, Section 2.3 for attitude estimation, Section 2.4 for multiple model adaptive estimation, and Section 2.2 for stochastic filtering.

3.3 Methodology

The following section will provide the methodology and mathematical algorithms for the numerical experiments validating the use of adaptive estimation for spacecraft attitude determination and MOI estimates. Crassidis and Markley's unscented quaternion estimator is presented, followed by a discussion of the various adaptive estimation routines used. Next, the magnetometer and gyro sensor model used in this research is introduced. The spacecraft MOI model is developed, and the flow of numerical experiments is discussed.

3.3.1 Unscented Quaternion Estimation.

Crassidis and Markley previously constructed a UKF routine for attitude estimation that is parameterized by the quaternion called the Unscented Quaternion Estimtor (USQUE) [16]. The standard UKF algorithm as established by Julier and Uhlmann [40; 41] is employed in USQUE; however, as the predicted attitude quaternion is a weighted sum of filtered estimates, there is no guarantee of satisfying the quaternion unit-norm constraint [16]. Thus, intermediate conversions between error quaternions and error Generalized Rodrigues Parameters (GRPs) are used to maintain the unit-norm constraint. Although the Extended Kalman Filter (EKF) has been the "workhorse" of attitude estimation, Crassidis offers four advantages of the UKF over the EKF: (1) the USQUE has a lower expected error than the EKF,

(2) application to functions that are not differentiable, (3) avoidance of the Jacobian derivation, and (4) applicability to higher-order expansions than the EKF [16]. This section will briefly detail the USQUE algorithm, while the fundamentals of unscented filtering, such as the $2n + 1$ sigma point calculation, can be found in the works by Julier and Uhlmann [40; 41] and are also detailed in Algorithm 1 in Chapter 2. The estimation routine presented here will vary from the classical USQUE method in that the angular velocities are being included as states. Further, for initial results in this research, sensor gyroscopic measurements are assumed as unbiased, thus precluding the need to include bias estimates as sigma points. A significant portion of the USQUE algorithm relies on quaternion mathematics which are briefly described in this section; for a more thorough overview of quaternion operations, the reader is directed to Shuster [27] or Arribas, et al. [97].

First, a set of sigma points corresponding to the error GRPs $\boldsymbol{\chi}_k^{\delta p}$ is constructed, and then converted to local error quaternions. Denoted by $\delta \mathbf{q}_k^-(i)$, the local error quaternion associated with the ith error GRP at time step k is constructed as [16]

$$\delta \mathbf{q}_k^-(i) = \begin{bmatrix} \delta \boldsymbol{\varrho}_k^-(i) \\ \delta q_{4_k}^-(i) \end{bmatrix}. \tag{3.1}$$

The local error quaternion components $\delta \boldsymbol{\varrho}_k^-(i)$ and $\delta q_{4_k}^-(i)$ are calculated as [16]

$$\delta \boldsymbol{\varrho}_k^-(i) = f^{-1} \left[a + \delta q_{4_k}^-(i) \right] \boldsymbol{\chi}_k^{\delta p}(i)$$

$$\delta q_{4_k}^-(i) = \frac{-a \left\| \boldsymbol{\chi}_k^{\delta p}(i) \right\|^2 + f \sqrt{f^2 + (1 - a^2) \left\| \boldsymbol{\chi}_k^{\delta p}(i) \right\|^2}}{f^2 + \left\| \boldsymbol{\chi}_k^{\delta p}(i) \right\|^2}. \tag{3.2}$$

Here, a is a parameter between 0 and 1, f is a scaling factor, and $i = 0, 1, \ldots 2n$ represents the $(2n+1)$ sigma points. Both of the a and f parameters can heuristically be tuned for the filter, while setting f to $2(a + 1)$ yields attitude error covariance on the order of roll, pitch, and yaw angle errors [62]. Having a representation of the

local error quaternion, a quaternion sigma point can be constructed using quaternion multiplication

$$\hat{\mathbf{q}}_k^-(i) = \delta\mathbf{q}_k^-(i) \otimes \hat{\mathbf{q}}_k^-(0), \tag{3.3}$$

where $\hat{\mathbf{q}}_k^-(0)$ is the *a priori* quaternion estimate resulting from propagating the previous time step. The quaternion multiplication is taken as

$$\mathbf{q}_a \otimes \mathbf{q}_b = \begin{bmatrix} \mathbf{\Psi}(\mathbf{q}_a) & \mathbf{q}_b \end{bmatrix} \mathbf{q}_b. \tag{3.4}$$

Having assembled a set of sigma points now consisting of quaternions and angular velocities, the sigma points are propagated through the nonlinear system dynamics such that

$$\dot{\boldsymbol{\chi}}(i) = \mathbf{f}(\boldsymbol{\chi}(i), \hat{\mathbf{q}}(i)), \tag{3.5}$$

where $\mathbf{f}(\cdot)$ represents the assumed dynamics of the system. For the rigid body example with constant MOI, this would simply be Euler's equations. The mean quaternion sigma point $\hat{\mathbf{q}}_{k+1}^-(0)$ from the propagation is stored, and serves as the *a priori* estimate for the next time step $k+1$. The error quaternion associated with each propagated quaternion sigma point is also calculated from $\hat{\mathbf{q}}_{k+1}^-(0)$ using

$$\delta\hat{\mathbf{q}}_{k+1}^-(i) = \hat{\mathbf{q}}_{k+1}^-(i) \otimes \left[\hat{\mathbf{q}}_{k+1}^-(0)\right]^{-1}. \tag{3.6}$$

The conjugate or inverse quaternion $[\mathbf{q}]^{-1}$ is given as

$$[\mathbf{q}]^{-1} = \begin{bmatrix} -\boldsymbol{\varrho} \\ q_4 \end{bmatrix}. \tag{3.7}$$

Note that, as expected, a quaternion times its inverse produces the identity quaternion. The error GRP points at time step $k+1$ can now be determined from

$$\delta\mathbf{p}_{k+1}^-(i) = f\frac{\delta\boldsymbol{\varrho}_{k+1}^-(i)}{a + \delta\hat{q}_{4_{k+1}}^-(i)}. \tag{3.8}$$

Now there is a complete set of sigma points with care taken to maintain a unit norm constraint. The sigma points are now implemented in the standard UKF state and

covariance estimation scheme, briefly detailed here. The weighted sum of sigma points yields the mean state estimate as [62]

$$\hat{\mathbf{x}}_{k+1}^- = \sum_{i=0}^{2n} W_i^{\text{mean}} \boldsymbol{\chi}_{k+1}(i), \tag{3.9}$$

and the state covariance $\mathbf{P}_{k+1}^{xx}$ is calculated from a weighted sum as

$$\mathbf{P}_{k+1}^{xx} = \mathbf{Q}_{k+1} + \sum_{i=0}^{2n} W_i^{\text{cov}} \left(\boldsymbol{\chi}_{k+1}(i) - \mathbf{x}_{k+1}^- \right) \left(\boldsymbol{\chi}_{k+1}(i) - \mathbf{x}_{k+1}^- \right)^T, \tag{3.10}$$

where $\mathbf{Q}_{k+1}$ is the process noise covariance. The weights W_i^{mean} and W_i^{cov} can be heuristically chosen for proper tuning, or to match higher order statistical moments.

The information gained from the available measurements can now be used to innovate the state estimate. Let the measurement state vector be denoted as $\tilde{\mathbf{y}}$. Each sigma point construction (consisting of quaternions rather than GRPs) can be used to compute expected measurements using a given measurement relation $\mathbf{h}()$. For the ith sigma point, the corresponding output can be given as [62]

$$\boldsymbol{\gamma}_{k+1}(i) = \mathbf{h} \left(\boldsymbol{\chi}_{k+1}(i), \hat{\mathbf{q}}_k^-(i) \right). \tag{3.11}$$

Similar to Eq. (3.9), the output estimate can be computed as a weighted sum as

$$\hat{\mathbf{y}}_{k+1}^- = \sum_{i=0}^{2n} W_i^{\text{mean}} \boldsymbol{\gamma}_{k+1}(i). \tag{3.12}$$

The difference between the actual measurement vector $\tilde{\mathbf{y}}_{k+1}$ and the output estimate $\hat{\mathbf{y}}_{k+1}^-$ is the residual $\boldsymbol{\nu}_{k+1}$ for this time step. The residual covariance $\mathbf{P}_{k+1}^{\nu\nu}$ and cross-correlation $\mathbf{P}_{k+1}^{xy}$ covariances are now given as [62]

$$\begin{aligned} \mathbf{P}_{k+1}^{\nu\nu} &= \mathbf{R}_{k+1} + \sum_{i=0}^{2n} W_i^{\text{cov}} \left(\boldsymbol{\gamma}_{k+1}(i) - \hat{\mathbf{y}}_{k+1}^- \right) \left(\boldsymbol{\gamma}_{k+1}(i) - \hat{\mathbf{y}}_{k+1}^- \right)^T \\ \mathbf{P}_{k+1}^{xy} &= \sum_{i=0}^{2n} W_i^{\text{cov}} \left(\boldsymbol{\chi}_{k+1}(i) - \mathbf{x}_{k+1}^- \right) \left(\boldsymbol{\gamma}_{k+1}(i) - \hat{\mathbf{y}}_{k+1}^- \right)^T \end{aligned} \tag{3.13}$$

The remaining steps now exploit the information available in the estimate covariances to calculate a Kalman gain to update the state estimate. The Kalman gain is

computed using the classical relation

$$\mathbf{K}_{k+1} = \mathbf{P}_{k+1}^{xy} \left(\mathbf{P}_{k+1}^{\nu\nu} \right)^{-1}, \tag{3.14}$$

and the state (with attitude represented as error GRPs) is updated accordingly by

$$\hat{\mathbf{x}}_{k+1}^{+} = \hat{\mathbf{x}}_{k+1}^{-} + \mathbf{K}_{k+1} \boldsymbol{\nu}_{k+1}, \tag{3.15}$$

The last step now involves transforming the newly updated error GRP to update the quaternion estimate. Already having the *a priori* quaternion estimate $\hat{\mathbf{q}}_{k+1}^{-}(0)$, the error GRP is converted to the error quaternion $\delta\hat{\mathbf{q}}_{k+1}$ using Eq. (3.2), and then producing the updated quaternion with

$$\hat{\mathbf{q}}_{k+1}^{+} = \delta\hat{\mathbf{q}}_{k+1} \otimes \hat{\mathbf{q}}_{k+1}^{-}(0). \tag{3.16}$$

3.3.2   *Adaptive Estimation Methods.*

The following section will mathematically describe the adaptive estimation routines used in this research. The classical MMAE algorithm is first detailed, followed by Linares' modification of the recursive weighting scheme in the Adaptive Likelihood Mixture (ALM) method. Next, Soken's modification of the MMAE Probability Distribution Function (PDF) is presented where sudden changes are sought by implementing a psuedo low-pass filter in the scheme. Finally, a hybrid of the Soken and ALM scheme developed in this research is presented and discussed.

3.3.2.1   *Classical Multiple Model Adaptive Estimation.*

In this section, the MMAE algorithm will be shown following Stengel [37], Marschke and Crassidis [98], and Linares [62]. Given a vector of parameters $\mathbf{p}$ that is assumed constant during a particular sampling or adaptation interval, the goal of the (MMAE) process is to determine the conditional PDF of the jth element of $\mathbf{p}$ given the current measurement $\tilde{\mathbf{y}}_k$. The conditional probability of a particular parameter or assumed dynamics model given a measurement sequence will be the metric to

select likely models. The measurement vector enters the bank of filters, each with its own assumed model and output estimates. Additionally, a filter-specific covariance estimate will be output as in most standard estimation routines.

The following probability equations use the convention that a superscript (l) indicates the value is associated with model (l), while a subscript (k) indicates the variable is associated with time-step k. For example, $\hat{\mathbf{x}}_k^{(l)}$ is the state estimate associated with model (l) at time-step k. The conditional probability of an individual bank model given a measurement vector at time k can be found via Bayes' rule and Kalman recursion as [98]

$$p\left(\mathbf{p}^{(l)}|\tilde{\mathbf{y}}_k\right) = \frac{p\left(\tilde{\mathbf{y}}_k|\hat{\mathbf{x}}_k^{-(l)}\right) p\left(\mathbf{p}^{(l)}|\tilde{\mathbf{y}}_{k-1}\right)}{\sum\limits_{j=1}^{M}\left[p\left(\tilde{\mathbf{y}}_k|\hat{\mathbf{x}}_k^{-(j)}\right) p\left(\mathbf{p}^{(j)}|\tilde{\mathbf{y}}_{k-1}\right)\right]}, \tag{3.17}$$

where M is the number of filters in the bank. There is an inherent recursive relation in the algorithm, as $p\left(\mathbf{p}^{(l)}|\tilde{\mathbf{y}}_k\right)$ is a direct function of $p\left(\mathbf{p}^{(l)}|\tilde{\mathbf{y}}_{k-1}\right)$. The $p\left(\tilde{\mathbf{y}}_k|\hat{\mathbf{x}}_k^{-(l)}\right)$ term is the likelihood of an observed measurement given the estimated state from each filter. A standard PDF used in the literature is a multivariate Gaussian using the residuals ν and estimated innovation covariance $\mathbf{P}_{\nu\nu}$, given as

$$p\left(\tilde{\mathbf{y}}_k|\hat{\mathbf{x}}_k^{-(l)}\right) = \frac{1}{(2\pi)^{n/2}\det(\mathbf{P}_{\nu,k}^{(l)})^{1/2}} \exp\left(-\frac{1}{2}\boldsymbol{\nu}_k^{(l)T}\mathbf{P}_{\nu\nu,k}^{-1(l)}\boldsymbol{\nu}_k^{(l)}\right). \tag{3.18}$$

Eq. 3.18 is a multivariate Gaussian distribution that is centered around a zero-mean residual vector, implying that the PDF is examining where the n-dimensional residual vector lies along the n-dimensional normal distribution with a given covariance. Eq. 3.18 is computationally less expensive for single state measurements as matrix inversions are reciprocals, and the determinant of a scalar is a scalar. Whereas for an n-dimensional residual vector, the covariance inversion requires approximately $O(n^3)$ operations, and the covariance determinant also requires approximately $O(n^3)$ operations. Further examining Eq. (3.18), models with lower residuals will increase

the probability, while smaller values of $\det(\mathbf{P}_{\nu\nu,k}^{(l)})^{1/2}$ (that is, a smaller variance) will also increase the likeliness of a specific model. Near-singular covariance values will provide difficulties for the algorithm.

The conditional probabilities can now be cast into weights to produce weighted state estimates and covariances as a function of the multiple models in the bank. A common recursion relation for the calculation of the weight $\mathbf{w}_k^{(l)}$ vector is

$$\mathbf{w}_k^{(l)} = \mathbf{w}_{k-1}^{(l)} p\left(\tilde{\mathbf{y}}_k | \hat{\mathbf{x}}_k^{-(l)}\right). \tag{3.19}$$

An initial value for the weight must be assumed, and equal weighting is often appropriate unless prior knowledge is known to initialize otherwise. Weighted sums of the filter estimates can now be used to estimate the conditional mean state $\hat{x}_k$, parameter estimate $\hat{\mathbf{p}}_k$, and state error covariance $\mathbf{P}_{xx,k}^-$ from the following

$$
\begin{aligned}
\hat{\mathbf{x}}_k &= \sum_{l=1}^{M} \mathbf{w}_k^{(l)} \hat{\mathbf{x}}_k^{-(l)} \\
\hat{\mathbf{p}}_k &= \sum_{l=1}^{M} \mathbf{w}_k^{(l)} \mathbf{p}^{(l)} \\
\mathbf{P}_k^{xx} &= \sum_{l=1}^{M} \mathbf{w}_k^{(l)} \left[\left(\hat{\mathbf{x}}_k^{-(l)} - \hat{\mathbf{x}}_k^-\right) \left(\hat{\mathbf{x}}_k^{-(l)} - \hat{\mathbf{x}}_k^-\right)^T + \mathbf{P}_{xx,k}^{-(l)} \right]
\end{aligned}
\tag{3.20}
$$

Eq. (3.20) concludes the estimation routine at time-step k. The new state and covariance estimates are then used as inputs for the next iteration. The covariance relations can provide bounds on the parameter estimates in terms of standard deviations σ. The estimation outputs allow for easy visualization of a time history of the state estimate and its 3σ boundaries. The bank of filters in the MMAE framework can assume a variety of modes to capture the parameter, but computational time will increase with additional hypotheses. Figure 3.1 provides a visualization of the classical MMAE algorithm.
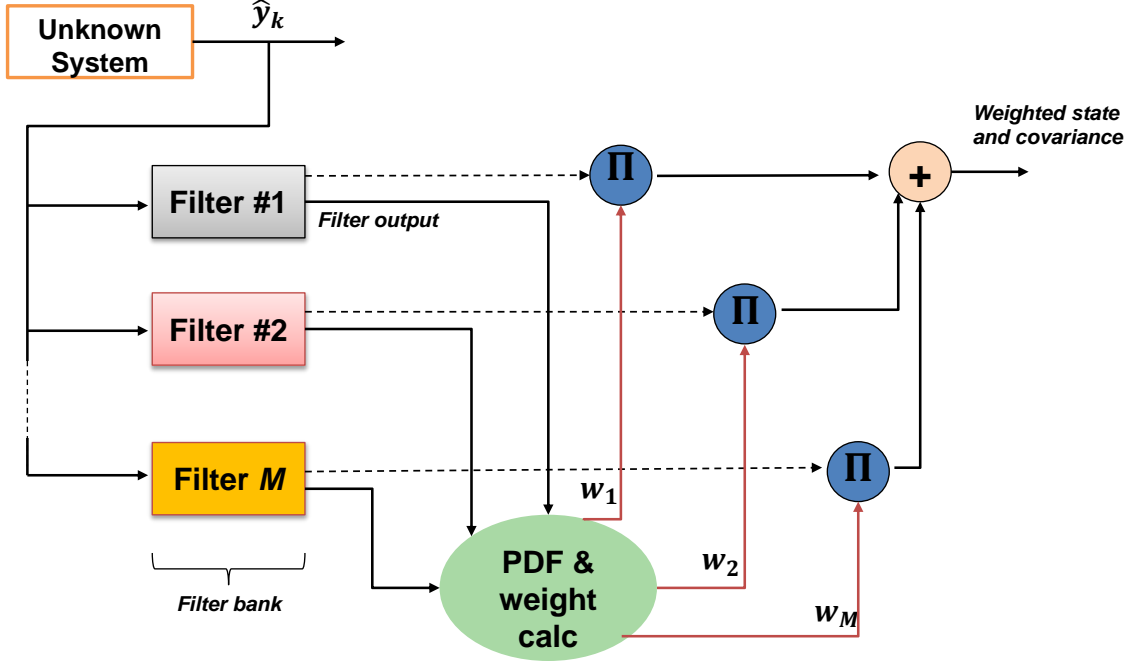
Figure 3.1: Visualization of the classical MMAE algorithm.

3.3.2.2 *Adaptive Likelihood Mixtures.*

Linares modified and presented the likelihood functions of the classical MMAE scheme in an algorithm proposed as ALM [9]. The main motivation in the ALM development was to decrease the memory of the likelihood ratios. Noting in Eq. (3.19), the weighting calculation is recursive and has a memory that retains information from the beginning of the adaption. The ALM method innovates the MMAE scheme by weighing models using current performance and measurements, and by reinitializing each filter in the bank by the weighted state and covariance estimates [9]. Each model is initialized with an equal weighting and probability, and the current weight ascribed to model (l) at time step (k), rather than being recursively calculated, is found by

$$w_k^{(l)} = p\left(\tilde{\mathbf{y}}_{k-1}|\hat{\mathbf{x}}_{k-1}^{+(l)}\right), \tag{3.21}$$

where the PDF in Eq. (3.21) is the Gaussian calculation from Eq. (3.18). The recursion is removed now using only the current PDF values, and the weights are normalized by

$$w_k^{(l)} = \frac{w_k^{(l)}}{\sum_{j=1}^{M} w_k^{(j)}}, \tag{3.22}$$

where j is the elemental filter index. The state and covariance estimates are then found using the MMAE formulation in Eq. (3.20), and the individual filter state and covariance estimates at time step $(k+1)$ are reset as the weighted state and covariance estimates from time step (k). Linares' ALM development now provides a reduced memory multiple model scheme that is better suited for sudden changes in system dynamics over long propagation intervals than the classical MMAE algorithm [9]. However, for short propagation intervals the ALM scheme will tend to equalize models [9].

3.3.2.3 Soken's Likelihood Function.

In [60], Soken et al. modified the likelihood function of the classical MMAE scheme to account for steady-state errors and the agility of the filter. The remainder of the classical MMAE algorithm remains the same as described in Section 3.3.2.1. Using the notation from the current research, Soken's likelihood function takes the form

$$p\left(\mathbf{p}^{(l)}|\tilde{\mathbf{y}}_k^{-(l)}\right) = \frac{\exp\left(-q_{i,k}^{(l)} - q_{2,k}^{(l)}\right)}{\sum_{j=1}^{M}\left[\exp\left(-q_{i,k}^{(j)} - q_{2,k}^{(j)}\right)\right]}, \tag{3.23}$$

where $q_{1,k}^{(l)}$ is a measure of steady-state error and $q_{2,k}^{(l)}$ accounts for the agility of the filter [60]. Here, $q_{j,k}^{(l)}$ is a function input and should not be confused with the quaternion or components of the quaternion. The steady-state error is accounted for by first establishing a moving window of size μ. Soken's algorithm incorporates the parameter as a state, and since the current research decouples the parameter from the state vector, Soken's algorithm must be modified slightly. This modification

produces a novelty in that the state dimension remains the same, and the Soken scheme is adapted to decouple the parameter from the state vector. A moving average parameter estimate $\hat{\mathbf{p}}_{\mathrm{mean},k}$ is defined as the average of the weighted estimates over the previous μ time steps as

$$\hat{\mathbf{p}}_{\mathrm{mean},k} = \frac{1}{\mu} \sum_{j=k-\mu+1}^{k} \hat{\mathbf{p}}_j. \tag{3.24}$$

Given that each filter is assuming a parameter value $\mathbf{p}^{(l)}$, a scalar filter specific error metric can be calculated as

$$Z_k^{(l)} = \left(\hat{\mathbf{p}}_{\mathrm{mean},k} - \mathbf{p}^{(l)}\right)^T \left(\hat{\mathbf{p}}_{\mathrm{mean},k} - \mathbf{p}^{(l)}\right). \tag{3.25}$$

The error metric is then filtered with a pseudo low-pass filter scheme

$$g_{1,k}^{(l)} = \lambda_1 g_{1,k-1}^{(l)} + (1 - \lambda_1) Z_k^{(l)}, \tag{3.26}$$

where λ_1 controls the the amount of recursiveness and impact of the error metric. Lastly, the likelihood function input is scaled to fall into a range $[0, a]$ as

$$q_{1,k}^{(l)} = \frac{a \left(g_{1,k}^{(l)} - \min\left(\mathbf{g}_{1,k}\right)\right)}{\max\left(\mathbf{g}_{1,k}\right) - \min\left(\mathbf{g}_{1,k}\right)} \tag{3.27}$$

The filter agility is accounted for by examining the individual filter innovation covariances by the metric

$$\mathrm{En}_k^{(l)} = \frac{1}{\sqrt{M}} \mathbf{1}_m^T \left[\mathbf{H}\mathbf{P}_{k-1/k}^{(l)}\mathbf{H}^T + \mathbf{R}_k\right]^{-1/2} \left[\tilde{\mathbf{y}}_k - \hat{\mathbf{y}}^{(l)}\right], \tag{3.28}$$

where M is the number of filters in the bank, $\mathbf{1}_m$ is an $M \times 1$ vector of ones, and the other values have previously been described. However, Soken's innovation metric is prescribed for an EKF and must be adopted for the current UKF implementation. The first bracketed term in Eq. (3.28) is the innovation covariance $\mathbf{P}_{\nu\nu}$, and the second bracketed term in Eq. (3.28) is the innovation or residual $\boldsymbol{\nu}$. Using the UKF notation, the innovation metric is then calculated as

$$\mathrm{En}_k^{(l)} = \frac{1}{\sqrt{M}} \mathbf{1}_m^T \mathbf{P}_{\nu\nu,k}^{(l)-1/2} \boldsymbol{\nu}_k^{(l)}. \tag{3.29}$$

A pseudo low-pass filter is then applied to the innovation metric, and a recursive relation gives non-normalized value

$$g_{2,k}^{(l)} = \lambda_2 g_{2,k-1}^{(l)} + (1 - \lambda_2) \operatorname{En}_k^{(l)}, \tag{3.30}$$

where λ_2 is a tuning parameter similar to λ_1. A scaling parameter β is then introduced such that the likelihood function input is

$$q_{2,k}^{(l)} = \frac{|g_{2,k}^{(l)}|}{\beta}. \tag{3.31}$$

The likelihood inputs $g_{1,k}^{(l)}$ and $g_{2,k}^{(l)}$ are calculated for each filter (l) and used to determine the normalized likelihood value.

3.3.2.4 A Hybrid Likelihood Mixture Method.

A portion of this research examined the combination of the ALM algorithm described in Section 3.3.2.2 and the Soken likelihood model described in Section 3.3.2.3. This hybrid likelihood mixture method replaces the likelihood quotient calculation in the classical MMAE structure with the Soken likelihood calculation discussed previously. Additionally, rather than each filter self-initializing with its own state and covariance estimates, the filters are all re-initialized with the current weighted state and covariance estimate from the adaptive estimation process. Additionally, the model weights are calculated using the memoryless method provided by ALM. The hybrid likelihood mixture method is summarized in Algorithm 2.

3.3.3 Sensor Model.

To simulate available on-orbit measurements, this numerical experiment assumes the availability of Three Axis Magnetometer (TAM) data as well as gyroscope data providing angular rates. Deterministically speaking, a single TAM is typically not capable of providing attitude estimates, but in a recursive stochastic filtering sense, a single TAM is able to allow estimate convergence [99].

Algorithm 2: Hybrid Likelihood Mixture Method

Given $\hat{\mathbf{x}}_{k-1}^+$, measurement vector $\tilde{\mathbf{y}}_k$, and covariance $\mathbf{P}_{xx,k-1}^+$ estimates at time t_{k-1} and a filter bank of multiple models

1 Initialize filters $1, 2, ..., M$ with state and covariance estimates

2 For filters $1, 2, ..., M$, calculate residuals $\boldsymbol{\nu}$, innovation covariance $\mathbf{P}_{\nu\nu}$, state and covariance estimates according to individual filter rules

3 Calculate likelihood values $p\left(\mathbf{p}^{(l)}|\tilde{\mathbf{y}}_k^{-(l)}\right)$ according to Eq. (3.23)

4 Calculate model weights $w_k^{(l)}$ according to Eqs.(3.21) and (3.22).

5 Calculate weighted state, covariance, and parameter estimates for time step t_k using Eq. (3.20).

6 Re-initialize filters $1, 2, ..., M$ with weighted estimates, repeat algorithm.

To demonstrate a proof of concept in this research, an unbiased TAM is used along with inertial gyroscopes. The TAM measures the magnetic field of the Earth in the spacecraft body frame, while the gyroscopes provide the angular rate measurements with respect to an inertial frame. The Earth's magnetic field can be expressed in the spacecraft's orbital frame with a simple dipole model as [99]

$$
\begin{aligned}
B_1(t) &= \frac{M_e}{r_0^3}\left[\mathrm{c}_\omega\left[\cos\left(\epsilon\right)\sin\left(i\right) - \sin(\epsilon)\cos\left(i\right)\cos\left(\omega_e t\right)\right] - \mathrm{s}_\omega\sin\left(\epsilon\right)\sin\left(\omega_e t\right)\right] \\
B_2(t) &= -\frac{M_e}{r_0^3}\left[\cos(\epsilon)\cos(i) + \sin(\epsilon)\sin(i)\cos(\omega_e t)\right] \qquad\qquad . \quad (3.32) \\
B_3(t) &= \frac{2M_e}{r_0^3}\left[\mathrm{s}_\omega\left[\cos\left(\epsilon\right)\sin\left(i\right) - \sin(\epsilon)\cos\left(i\right)\cos\left(\omega_e t\right)\right] + 2\mathrm{c}_\omega\sin\left(\epsilon\right)\sin\left(\omega_e t\right)\right]
\end{aligned}
$$

where M_e is the magnetic dipole moment of the Earth, r_0 is the orbital radius of the spacecraft, ω_0 is mean motion of the spacecraft, i is the orbital inclination, ϵ is the magnetic dipole tilt, c_ω is $\cos\left(\omega_0 t\right)$, s_ω is $\sin\left(\omega_0 t\right)$ and ω_e is the spin rate of the Earth. Since this magnetic field is given in the orbital frame and the spacecraft measures the

magnetic field expressed in the body frame, the TAM measurement is then given as

$$\tilde{\mathbf{y}}_{\text{TAM}} = \mathbf{R}_{BO}(\mathbf{q}(t)) \begin{bmatrix} B_1(t) \\ B_2(t) \\ B_3(t) \end{bmatrix} + \mathbf{v}_{TAM}, \tag{3.33}$$

where $\mathbf{R}_{BO}$ is the rotation matrix from the orbital frame to the spacecraft body frame using the current quaternion, and $\mathbf{v}_{\text{TAM}}$ is zero-mean Gaussian measurement noise with covariance assumed as $\sigma^2_{\text{TAM}}\mathbf{1}_{3\times3}$.

As the rotation matrix $\mathbf{R}_{BO}$ is a function of the quaternion defining the orientation of the body frame with respect to the orbital frame, the quaternion dynamics must be modified slightly to include the rotation of the orbital frame. The EOMs used for the quaternion are now [99]

$$\begin{aligned} \dot{q}_1(t) &= \frac{1}{2}\left[\omega_1(t)q_4(t) - \omega_2(t)q_3(t) + \omega_3(t)q_2(t) + \omega_0(t)q_3(t)\right] \\ \dot{q}_2(t) &= \frac{1}{2}\left[\omega_1(t)q_3(t) + \omega_2(t)q_4(t) - \omega_3(t)q_1(t) + \omega_0(t)q_4(t)\right] \\ \dot{q}_3(t) &= \frac{1}{2}\left[-\omega_1(t)q_2(t) + \omega_2(t)q_1(t) + \omega_3(t)q_4(t) - \omega_0(t)q_1(t)\right] \\ \dot{q}_4(t) &= \frac{1}{2}\left[-\omega_1(t)q_1(t) - \omega_2(t)q_2(t) - \omega_3(t)q_3(t) - \omega_0(t)q_2(t)\right] \end{aligned}, \tag{3.34}$$

and the rotation matrix $\mathbf{R}_{BO}$ is given as [99]

$$\mathbf{R}_{BO} = \begin{bmatrix} q_1^2 - q_2^2 - q_3^2 + q_4^2 & 2(q_1q_2 + q_3q_4) & 2(q_1q_3 - q_2q_4) \\ 2(q_1q_2 - q_3q_4) & q_2^2 - q_1^2 - q_3^2 + q_4^2 & 2(q_2q_3 + q_1q_4) \\ 2(q_1q_3 + q_2q_4) & 2(q_2q_3 - q_1q_4) & q_3^2 - q_1^2 - q_2^2 + q_4^2 \end{bmatrix}. \tag{3.35}$$

TAM measurements can now be generated using Eqs. (3.32) - (3.35) and corrupted with the appropriate Gaussian noise to simulate TAM measurements observed by the spacecraft.

Additionally, gyroscopic measurements are assumed available. Inertial gyros will also be employed on-board for the attitude estimation routine. Inertial gyros provide measurements of the angular velocity of the spacecraft body frame with respect to

the inertial frame, while expressed in the body frame. For this numerical experiment, the gyros are assumed to have zero-bias, although the USQUE method [16] assumes a bias whose time rate derivative is zero-mean Gaussian. The gyros will, however, be susceptible to measurement noise. The measurements observed by the spacecraft can then be expressed as

$$\tilde{\mathbf{y}}_{\text{GYRO}} = \tilde{\boldsymbol{\omega}} = \boldsymbol{\omega} + \mathbf{v}_{\text{GYRO}}, \tag{3.36}$$

where $\boldsymbol{\omega}$ is the true angular velocity and $\mathbf{v}_{\text{GYRO}}$ is zero-mean Gaussian measurement noise with covariance assumed as $\sigma_{\text{GYRO}}^2 \mathbf{1}_{3\times3}$. The true angular velocity will be simulated through numerical integration, while the appropriate noise will be added to produce the observations.

To summarize the preceding measurement discussion, the complete measurement vector is given as

$$\tilde{\mathbf{y}} = \begin{bmatrix} \tilde{\mathbf{y}}_{\text{TAM}} \\ \tilde{\mathbf{y}}_{\text{GYRO}} \end{bmatrix}. \tag{3.37}$$

The observation function $\mathbf{h}(\mathbf{x})$ is taken as the TAM measurement function and an identity multiplication on the angular velocities (assuming direct observation of the angular rate states that is only corrupted by the measurement noise).

3.3.4 Spacecraft Moment of Inertia Model.

A spacecraft model with separating and rotating payloads was developed by Leve, et al. [100] and is replicated here. Assume a particular spacecraft consists of a main bus, three separating payloads, a potentially rotating solar panel, and a large payload capable of large gimbal angles. A graphical depection is provided in Figure 3.2.

The MOI $\mathbf{I}$ of the overall system is taken as the sum of the individual components as

$$\mathbf{I} = \mathbf{I}_B + \mathbf{I}_S + \mathbf{I}_{SP} + \mathbf{I}_{PL}, \tag{3.38}$$
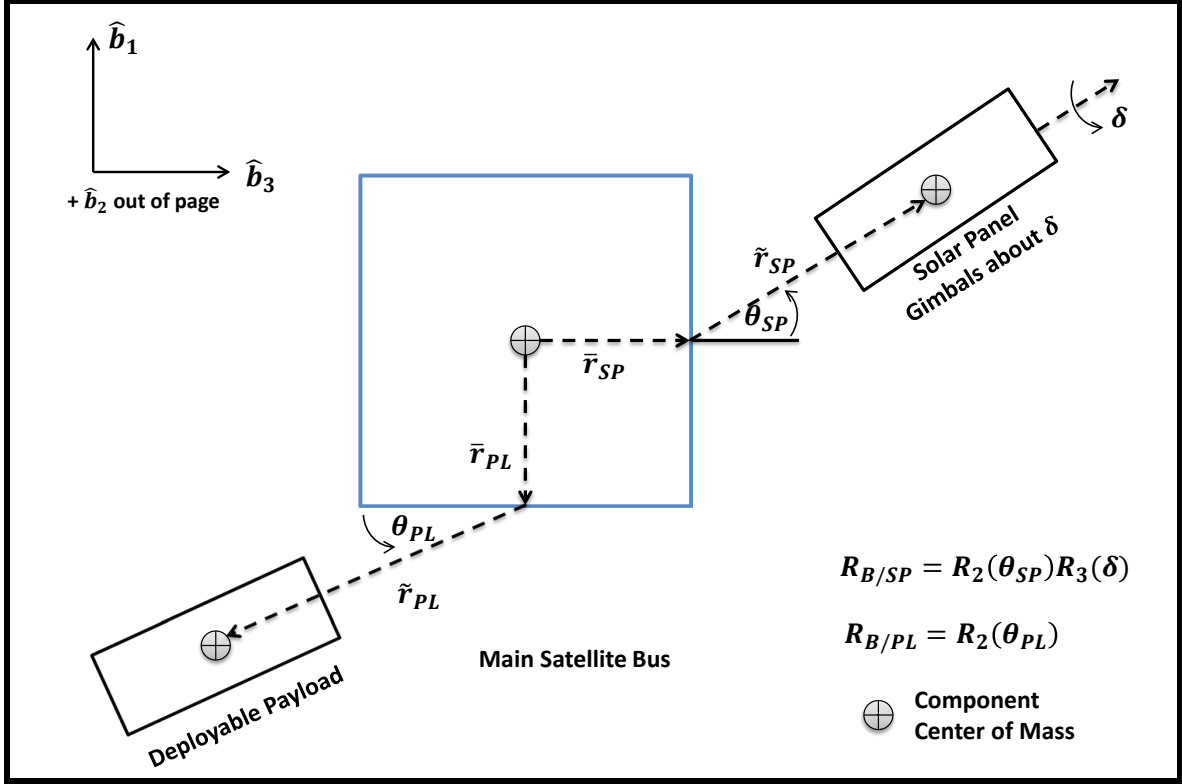
Figure 3.2: A notional diagram of a spacecraft with deployable rotating payload, solar panels, and (not shown) separable payloads used in Chapter 3 for numerical simulations [100].

where $\mathbf{I}_B$ is the primary bus MOI in the body frame, $\mathbf{I}_S$ is the total MOI of the separable payloads, $\mathbf{I}_{SP}$ is the MOI of the solar panel, and $\mathbf{I}_{PL}$ is the MOI of a deployable, gimbaling payload. The primary bus MOI will be taken as a constant in the body frame, and the other components will be expressed in the body frame. The rotation of the MOI matrix from one frame to another is known to require a pre- and post-matrix multiplication.

The MOI of the individual components will be calculated using the skew-symmetric formulation of the parallel axis theorem. The total MOI contribution

of the separable payloads is

$$\mathbf{I}_S = \sum_{i=1}^{3} \left(\mathbf{I}_{S,i} - m_{S,i} \hat{\mathbf{r}}_{S,i}^{\times} \hat{\mathbf{r}}_{S,i}^{\times} \right), \tag{3.39}$$

where $\mathbf{I}_{S,i}$ is the MOI of the payload expressed in the body frame, $m_{S,i}$ is the mass of payload i, and $\hat{\mathbf{r}}_{S,i}^{\times}$ is the skew-symmetric matrix consisting of the constant moment arm for separable payload i until separation. Separations will be treated as discontinuous changes in the payload mass and MOI and it is assumed translational motion is either unaffected or is controlled to remain nominal on-board the spacecraft.

The MOI contributions of the solar panel and rotating payload follow a similar development. The MOI matrix for the individual components is expressed in their respective references frames, and requires a rotation to the spacecraft body frame. Additionally, moment arms that are constant in the component frame are not necessarily constant when the payloads are rotating and also require a rotation. Finally, the skew-symmetric form of the parallel axis theorem is applied. For the solar panel SP and rotating payload PL, the MOI matrices are calculated using

$$\begin{aligned}
\mathbf{I}_{SP} &= \mathbf{R}_{B/SP} \left(\mathbf{I}_{SP,0} - m_{SP} \tilde{\mathbf{r}}_{SP}^{\times} \tilde{\mathbf{r}}_{SP}^{\times} \right) \mathbf{R}_{B/SP}^{T} - m_{SP} \bar{\mathbf{r}}_{SP}^{\times} \bar{\mathbf{r}}_{SP}^{\times} \\
\mathbf{I}_{PL} &= \mathbf{R}_{B/PL} \left(\mathbf{I}_{PL,0} - m_{PL} \tilde{\mathbf{r}}_{PL}^{\times} \tilde{\mathbf{r}}_{PL}^{\times} \right) \mathbf{R}_{B/PL}^{T} - m_{PL} \bar{\mathbf{r}}_{PL}^{\times} \bar{\mathbf{r}}_{PL}^{\times}
\end{aligned} \tag{3.40}$$

where $\mathbf{R}_{B/SP}$ and $\mathbf{R}_{B/PL}$ are the time-varying rotation matrices between, respectively, the body and solar panel frame and the body and rotating payload frame, m_{SP} and m_{PL} are the masses of the solar panel and rotating payload, $\mathbf{I}_{SP,0}$ and $\mathbf{I}_{PL,0}$ are the MOI of the solar panel and rotating payload in their respective reference frames, $\tilde{\mathbf{r}}_{SP}^{\times}$ is a skew-symmetric matrix of a constant moment arm in the solar panel frame, and $\tilde{\mathbf{r}}_{SP}^{\times}$ is a skew-symmetric matrix of a constant moment arm in the spacecraft body

frame. The time-varying rotation matrices are defined as

$$\mathbf{R}_{B/SP} = \mathbf{R}_2\left(\theta_{SP}\right)\mathbf{R}_3\left(\delta\right) = \begin{bmatrix} \cos\left(\theta_{SP}\right) & 0 & -\sin\left(\theta_{SP}\right) \\ 0 & 1 & 0 \\ \sin\left(\theta_{SP}\right) & 0 & \cos\left(\theta_{SP}\right) \end{bmatrix} \begin{bmatrix} \cos\left(\delta\right) & \sin\left(\delta\right) & 0 \\ -\sin\left(\delta\right) & \cos\left(\delta\right) & 0 \\ 0 & 0 & 1 \end{bmatrix}$$

$$\mathbf{R}_{B/PL} = \mathbf{R}_2\left(\theta_{PL}\right) = \begin{bmatrix} \cos\left(\theta_{PL}\right) & 0 & -\sin\left(\theta_{PL}\right) \\ 0 & 1 & 0 \\ \sin\left(\theta_{PL}\right) & 0 & \cos\left(\theta_{PL}\right) \end{bmatrix}$$

$$\text{(3.41)}$$

Here, θ_{SP}, δ, and θ_{PL} are the solar panel input angle, solar panel gimbal angle, and rotating payload input angle. The time derivatives of the rotation matrices can be found by simply differentiating component-wise or calculated in matrix form as

$$\dot{\mathbf{R}}_{B/SP} = \dot{\mathbf{R}}_2\left(\theta_{SP}\right)\mathbf{R}_3\left(\delta\right) + \mathbf{R}_2\left(\theta_{SP}\right)\dot{\mathbf{R}}_3\left(\delta\right)$$
$$\dot{\mathbf{R}}_{B/PL} = \dot{\mathbf{R}}_3\left(\theta_{PL}\right)$$

$$\text{(3.42)}$$

The time variation in the spacecraft MOI can now be found by differentiating Eq. (3.38) as

$$\dot{\mathbf{I}} = \dot{\mathbf{I}}_B + \dot{\mathbf{I}}_S + \dot{\mathbf{I}}_{SP} + \dot{\mathbf{I}}_{PL}. \tag{3.43}$$

The primary bus MOI is taken as a constant such that $\dot{\mathbf{I}}_B$ is zero, and the separable MOI changes are treated as discontinuities, so the $\dot{\mathbf{I}}_S$ term is neglected. The MOI time dependency is now only a function of the solar panel and rotating payload MOI contributions, which are primarily functions of the direction cosines between the body and component frames. For brevity, the following MOI terms are defined

$$\mathbf{I}'_{SP} = \mathbf{I}_{SP,0} - m_{SP}\tilde{\mathbf{r}}_{SP}^{\times}\tilde{\mathbf{r}}_{SP}^{\times}$$
$$\mathbf{I}'_{PL} = \mathbf{I}_{PL,0} - m_{PL}\tilde{\mathbf{r}}_{PL}^{\times}\tilde{\mathbf{r}}_{PL}^{\times}$$

$$\text{(3.44)}$$

such that the solar panel and payload MOI are more compactly expressed as

$$\mathbf{I}_{SP} = \mathbf{R}_{B/SP}\mathbf{I}'_{SP}\mathbf{R}_{B/SP}^T - m_{SP}\bar{\mathbf{r}}_{SP}^{\times}\bar{\mathbf{r}}_{SP}^{\times}$$
$$\mathbf{I}_{PL} = \mathbf{R}_{B/PL}\mathbf{I}'_{PL}\mathbf{R}_{B/PL}^T - m_{PL}\bar{\mathbf{r}}_{PL}^{\times}\bar{\mathbf{r}}_{PL}^{\times}$$

$$\text{(3.45)}$$

60

The time-derivative can now be calculated as

$$\dot{\mathbf{I}}_{SP} = \dot{\mathbf{R}}_{B/SP}\mathbf{I}'_{SP}\mathbf{R}^T_{B/SP} + \mathbf{R}_{B/SP}\mathbf{I}'_{SP}\dot{\mathbf{R}}^T_{B/SP}$$
$$\dot{\mathbf{I}}_{PL} = \dot{\mathbf{R}}_{B/PL}\mathbf{I}'_{PL}\mathbf{R}^T_{B/PL} + \mathbf{R}_{B/PL}\mathbf{I}'_{PL}\dot{\mathbf{R}}^T_{B/PL} \qquad (3.46)$$

The time-dependency of the spacecraft MOI is entirely a function of the variation of the direction cosines or, when applicable, the instantaneous payload separation. This coupling will allow for identification of solar panel and rotating payload inputs based on either a filter bank consisting of either possible payload input scenarios or a bank consisting of possible MOI configurations based on the current payload configuration of the spacecraft. Further, a note must be made concerning the numerical difficulties now faced. Care must be taken to ensure the principal MOI satisfies the triangle inequality for each MOI model for all time. Additionally, considering computation time, a single UKF propagates $2n+1$ sigma points. For m filters in the bank, $m(2n+1)$ points are now being propagated. When the MOI is included for as a time-varying 3×3 matrix, n increases to $n + 9$, and the computation costs increase accordingly.

3.3.5 Descriptions of Numerical Experiments and Common Parameters.

The following section will provide a description of the numerical experiments performed in this research. Three main scenarios are presented. The first demonstrates the utility of adaptive estimation is determining principal MOI ratios. The second scenario investigates the correct identification of payload input commands. The final scenario investigates a series of payload separations and a comparative study of various adaptive estimation schemes and their ability to detect sudden structural changes. Parameters that differ will be discussed in Sections 3.4.1 through 3.4.3 such as filter banks and initial conditions. The TAM measurements are assumed to be Gaussian distributed with a noise value (σ_{TAM}) of 300 nT [19]. The gyro measurements are assumed Gaussian distributed with noise values (σ_ω) detailed

in their respective results section. The measurement noise matrix $\mathbf{R}_k$ is assumed constant as

$$\mathbf{R}_k = \begin{bmatrix} \sigma_{\text{TAM}}^2 \cdot \mathbf{1}_{3\times 3} & \mathbf{0}_{3\times 3} \\ \mathbf{0}_{3\times 3} & \sigma_\omega^2 \cdot \mathbf{1}_{3\times 3} \end{bmatrix}. \tag{3.47}$$

The process noise in this experiment adapts a modified version of the process noise given in the USQUE method, where $\mathbf{Q}_{k+1}$ is given as [16]

$$\mathbf{Q}_{k+1} = \begin{bmatrix} \sigma_\omega^2 \cdot \Delta t \cdot \mathbf{1}_{3\times 3} & \mathbf{0}_{3\times 3} \\ \mathbf{0}_{3\times 3} & \sigma_\omega^2 \cdot \Delta t \cdot \mathbf{1}_{3\times 3} \end{bmatrix}. \tag{3.48}$$

Note, the process noise in the USQUE method also has a gyro bias term [16], but this bias term is assumed zero in this research as the gyro is assumed unbiased. As an initial testbed, this is valid, as future real-world experiments will examine direct quaternion measurements. The spacecraft is assumed to be in LEO at a 400 km altitude. Only Keplerian two-body motion is considered, and perfect knowledge of the orbital parameters is assumed for the magnetometer relations. Other parameters used in the magnetometer simulation are given in Table 3.1. Individual scenario initial conditions will be described in their respective results section.

3.3.6 Nominal Flow of Numerical Experiments.

Truth data will be generated from a set of initial conditions and the true dynamics model through numerical integration. The governing truth model will be determined by the specific numerical experiment being performed. Having simulated the true state and parameter values, TAM and gyroscopic measurements will be calculated using the measurement relation $\mathbf{h}(\mathbf{x})$. The true measurements will then be corrupted by a given amount of measurement noise that is distributed zero-mean Gaussian. These measurements now serve as input to a parallel bank of filters, each assuming a different dynamics model that will be described in the specific experiment. Although each filter assumes a different dynamics model, the general form of each filter will

Table 3.1: Simulation parameters used for magnetometer measurements and orbital characteristics.

Parameter	Value
Magnetic Dipole Tilt (deg)	11.7
Magnetic Dipole Moment (Wb-m)	$7.943E15$
Orbital Altitude (km)	400
Orbital Inclination (deg)	45
Gravitational Parameter (m^3/s^2)	$3.9860E14$
Earth Rotational Rate (rad/s)	$7.29E-5$

follow the USQUE method, where the sigma points are numerically propagated to maintain the unit quaternion norm according to the specific filter's assumed dynamics. The residuals and innovation covariance from each filter will then be input to the particular adaptive estimation scheme for evaluation.

3.3.7 Comparison Metrics.

Numerical simulations immediately provide a truth comparison, and there are immediate error metrics available. The error in the quaternion estimate $\mathbf{q}_e$ will be taken as the 2-norm of difference between the identity quaternion $\mathbf{q}_1$ and the quaternion product of the quaternion estimate $\hat{\mathbf{q}}$ at time step k and the inverse of the true quaternion at the same time step. Mathematically, this is expressed as

$$\mathbf{q}_e(t_k) = \left|\left| \mathbf{q}_1 - \hat{\mathbf{q}}(t_k) \cdot \mathbf{q}^{-1}(t_k) \right|\right|. \tag{3.49}$$

If the estimate $\hat{\mathbf{q}}$ is near the true value $\mathbf{q}$, then the product of the the estimate and the inverse of the true value will be near identity, and the 2-norm of the difference provides a comparison metric.

The angular velocity error will simply be the 2-norm of the vector difference between the estimated angular velocity from the filter and the true angular velocity from the truth simulation. The error in the MOI will be taken as the norm of the difference between the diagonal elements of the adaptive MOI estimate matrix and the true MOI matrix.

A metric specifically used for Scenario 3 will be the percentage of time a particular adaptive estimation scheme is classifying the correct operational mode. Given a set of likelihoods at a time step, the bank model with the maximum likelihood will be taken as the estimated operational mode. The percentage of correct mode identifications using the maximum likelihood model will then be taken as a metric for comparison.

3.4 Results and Discussion

The following section details the results and provides a discussion resulting the previously described three scenarios. Each section will first reintroduce the scenario verbally, and then numerically describe the specific parameters of each scenario. The various filter hypotheses in each bank are described. A brief overview of the specific numerical methodology for each experiment is described. Results and discussion are then presented for each scenario.

3.4.1 Results from Scenario 1: Principal MOI Estimation.

Scenario 1 examines the identification of the correct principal MOI in a bank of possible, realistic values. The application of this scenario alludes to a bank of possible operational modes or configurations, each with their respective MOI that is known to the user. Using streaming attitude data, the intent is to identify the correct MOI ratio using MMAE. In this context, for torque-free rigid body motion, only the relative MOI ratio can be estimated as discussed later in Chapter 5. Scenario 1 does not use the time-varying MOI model develiped in Section 3.3.4, but rather investigates nominal, physically realizable MOI values. A scenario time of five

64

minutes is used with a constant time step Δt of one second. Four gyro noise levels of $\sigma_\omega = 10^{-4}, 10^{-3}, 10^{-2}$, and 10^{-1} deg/s are examined. The initial spacecraft angular velocity and quaternion used in this scenario are

$$
\begin{aligned}
\boldsymbol{\omega}_0 &= \begin{bmatrix} 3 & 1.5 & 1 \end{bmatrix}^T \text{deg/s} \\
\mathbf{q}_0 &= \begin{bmatrix} 0 & 0 & 0 & 1 \end{bmatrix}^T
\end{aligned}
. \tag{3.50}
$$

Initial estimation errors of 5% are added to both the angular velocity and quaternion for additional realism in initial estimates. Since the unscented filter is actually estimating the GRPs for the attitude states, and intermediate conversions are performed for the quaternions, the attitude covariance is actually describing the GRPs. The initial GRP covariance $\mathbf{P}_0^{pp}$ and initial angular velocity covariance $\mathbf{P}_0^{\omega\omega}$ are given as

$$
\begin{aligned}
\mathbf{P}_0^{pp} &= 0.0087 \cdot \mathbf{1}_{3\times3} \\
\mathbf{P}_0^{\omega\omega} &= 0.0174 \cdot \mathbf{1}_{3\times3}
\end{aligned}
. \tag{3.51}
$$

The filter bank assumes five different MOI configurations detailed along with their respective relative MOI ratios in Table 3.2. The true model is an axisymmetric rigid body, while the other four models are asymmetric shapes representative of physically realizable systems. Care has been taken to ensure the MOI values do not violate the triangle inequality relationship among the principal moments of inertia. From a theoretical standpoint, this particular axisymmetric body configuration will result in a constant rotation about the body-1 axis, implying that $\dot{\omega}_1 = 0$ which will limit some of the information available to the estimator.

Figure 3.3 displays the results of a realization of the current scenario under the four different noise levels. For noise levels below $O(10^{-2})$, the adaptive estimation scheme is able to identify, with confidence, the true model in the bank in less than 15 seconds (or 15 time-steps since Δt is a constant step of one second). Figure 3.4
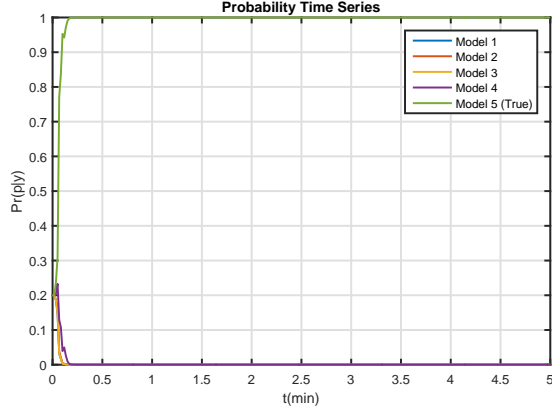
(a) $\sigma_\omega = 10^{-4}$ deg/s
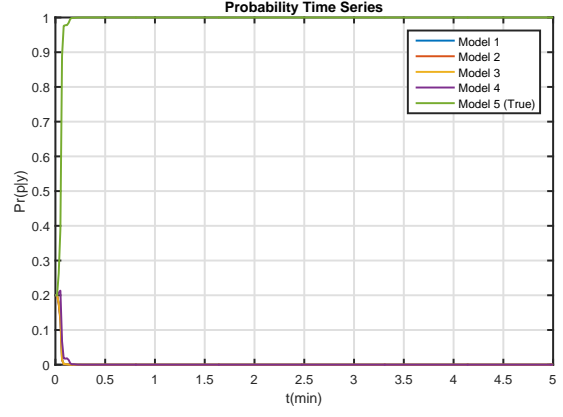
(b) $\sigma_\omega = 10^{-3}$ deg/s
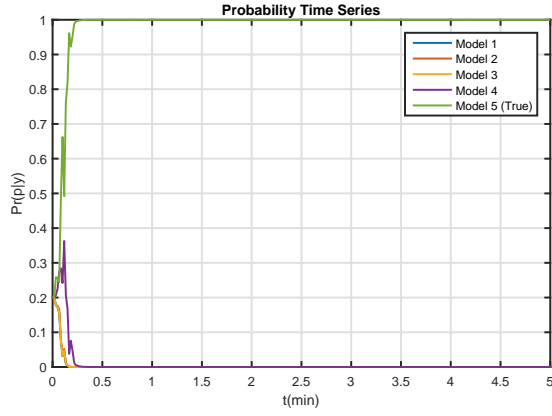
(c) $\sigma_\omega = 10^{-2}$ deg/s
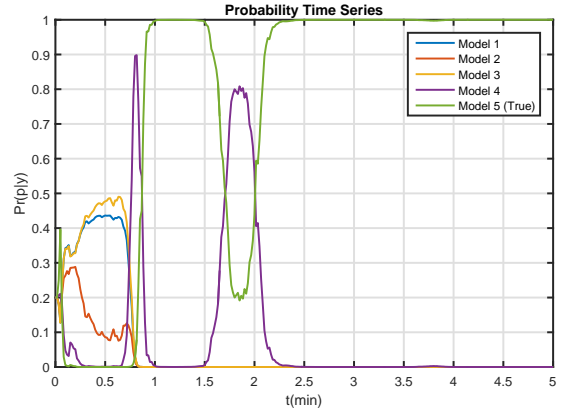
(d) $\sigma_\omega = 10^{-1}$ deg/s

Figure 3.3: Probability time series from a realization of Scenario 1 under four different gyro noise levels.

Table 3.2: Filter bank for Scenario 1: Principal MOI Estimation.

Filter	Assumed MOI in Filter (kg-m^2)	Associated MOI Ratios
1	$\mathbf{I}_1 = \text{diag}\left([500, 350, 150]^T\right)$	$\mathbf{p}_1 = [0.4000, -1.0000, -1.0000]^T$
2	$\mathbf{I}_2 = \text{diag}\left([210, 110, 95]^T\right)$	$\mathbf{p}_2 = [0.0750, -0.9545, 0.9474]^T$
3	$\mathbf{I}_3 = \text{diag}\left([140, 100, 40]^T\right)$	$\mathbf{p}_3 = [0.4286, -1.0000, 1.0000]^T$
4	$\mathbf{I}_4 = \text{diag}\left([500, 300, 290]^T\right)$	$\mathbf{p}_4 = [0.0200, -0.7000, 0.6897]^T$
5 (True)	$\mathbf{I}_5 = \text{diag}\left([200, 150, 150]^T\right)$	$\mathbf{p}_5 = [0, -0.3333, 0.3333]^T$

displays the estimation errors in angular velocity, attitude, MOI, and a probability time series for a realization using a noise level of $\sigma_\omega \sim O(10^{-2})$. The adaptive estimation scheme identifies the correct model again within 15 seconds, the quaternion error remains on the order of $O(10^{-4})$ and the angular velocity error is on the order of the measurement noise. As the correct model is identified, the adaptive weighting scheme calculates the MOI with a high degree of accuracy.

However, for the noise level where $\sigma_\omega \sim O(10^{-1})$, there is competition among the models. Notably, the MMAE scheme has difficulty in discerning between Model 4, an incorrect model, and Model 5, the true MOI for this scenario. This difficulty in model identification is attributed to two explanations. The first is that, other than Model 5, Model 4 is the closest parameter value to the truth, when examining the relative MOI ratio. Taking the 2-norm of the vector difference of relative MOI ratios, Model 4 has an error of approximately 0.51, compared to Models 1,2, and 3, whose errors are, respectively, 1.02, 0.88, and 1.04. The additional, and possibly coupled, cause of the conflict between Models 4 and 5 is attributed to the noise level in this scenario. Figure 3.5 displays the true values of $\dot{\boldsymbol{\omega}}$ compared to the four different noise levels that have been scaled by the time step. According to Figure 3.5, the changes
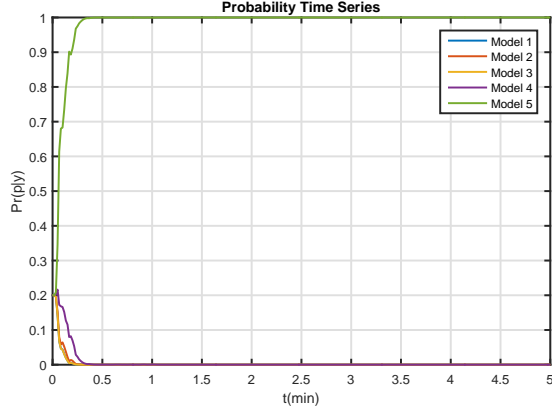
(a) Probability time series
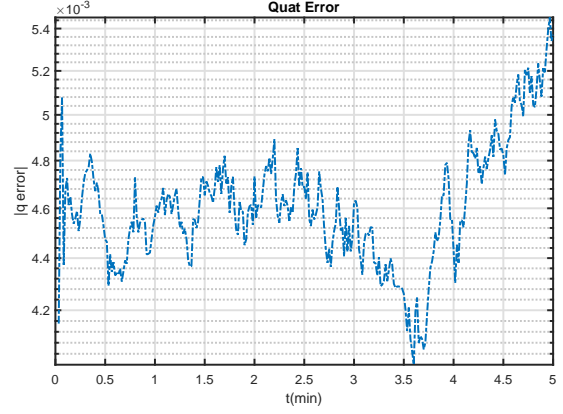
(b) Angular velocity estimation error
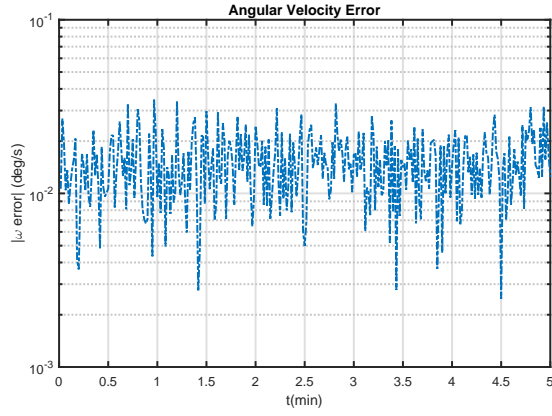
(c) Quaternion estimation error
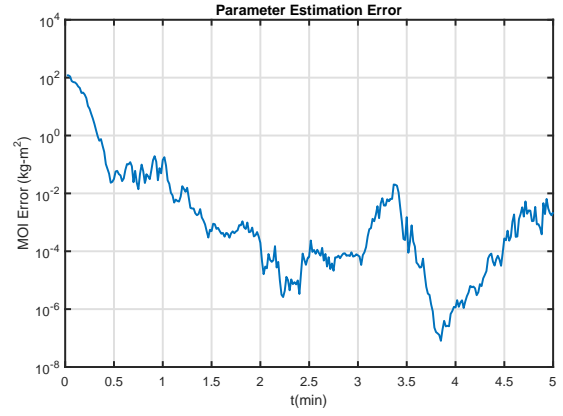
(d) MOI estimation error

Figure 3.4: Adaptive estimation results for Scenario 1 showing the probability time series and estimation errors in angular velocity, attitude, MOI, for a realization using a noise level of $\sigma_\omega \sim O(10^{-2})$.

in the dynamics of the system over time are below the noise floor allowed by the gyro measurements.
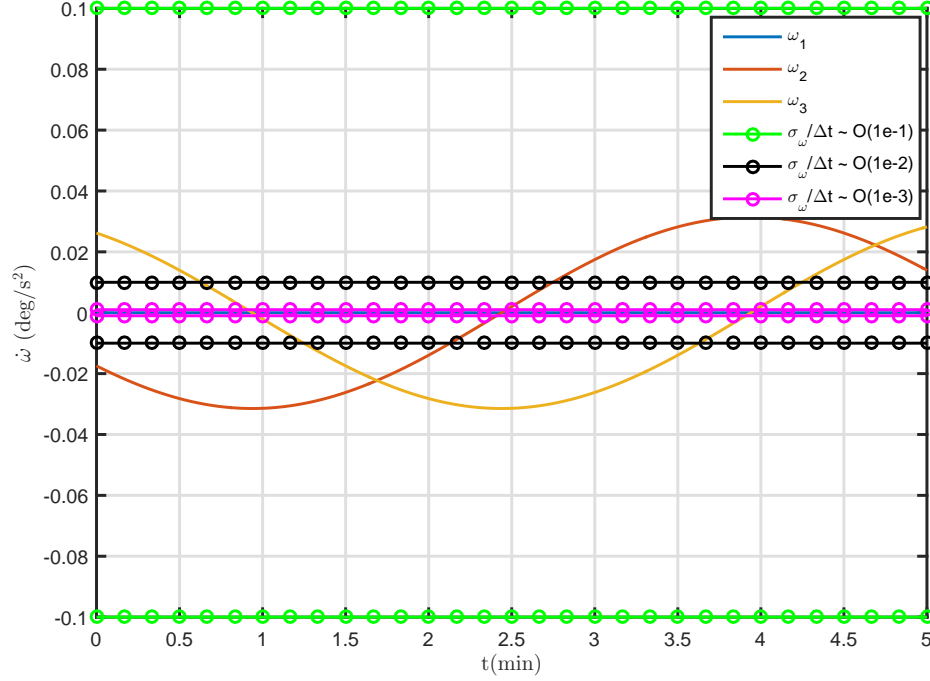
Figure 3.5: Comparison of noise levels to the true $\dot{\boldsymbol{\omega}}$ time history for Scenario 1, indicating that the changes in system dynamics and parameters that are greater than noise levels are difficult for the adaptive estimation scheme to detect.

This implies that for the given noise level, the adaptive estimation scheme may not be able to differentiate between system changes and system noise. From this, a key result from Scenario 1 is the notion that the adaptive estimation scheme might only account for system changes above a given threshold, otherwise these changes may be compensated for in gain calculations that are, in reality, attributable to system parameter changes. An additional result from Scenario 1's numerical experiment is that the MOI can be estimated from a bank of UKFs in a MMAE formulation using the particular measurement functions, a result that, to the author's knowledge, has

not been previously found. This observation implies this is the first contribution to the field in using banks of UKFs to estimate the MOI using onboard sensors. A final result from Scenario 1 also examined the impact of relative MOI ratios, and that for torque free rigid body motion, a body may be, in magnitude, significantly different in MOI, but if the relative MOI ratios are near, the rotational motion may be similar and difficult to discern in a filtering scheme.

3.4.2 Results from Scenario 2: Payload Input Command Identification.

Scenario 2 examines the identification of a commanded input to a payload. The application of this scenario alludes to potential known operational modes of spacecraft, and the utility of streaming attitude data to identify this mode via adaptive estimation. All other mass and MOI components of the spacecraft are assumed known, with the exception of the commanded input to the particular payload. The assumed MOI components can be found in more detail in Appendix A. Although this experiment is based on on-board sensors, the same principals will apply to ground-based algorithms using the same measurements, or post processing using the given measurements. The classical MMAE method as well as ALM will be applied to this scenario.

A scenario time of five minutes is used with a constant time step of two seconds. The initial spacecraft angular velocity and quaternion used in this scenario are

$$
\begin{aligned}
\boldsymbol{\omega}_0 &= \begin{bmatrix} 3 & 1.5 & 1 \end{bmatrix}^T \text{ deg/s} \\
\mathbf{q}_0 &= \begin{bmatrix} 0 & 0 & 0 & 1 \end{bmatrix}^T
\end{aligned}
\tag{3.52}
$$

Initial estimation errors of 5% are added to both the angular velocity and quaternion for additional realism in initial estimates. Since the unscented filter is actually estimating the GRPs for the attitude states, and intermediate conversions are performed for the quaternions, the attitude covariance is actually describing the

70

GRPs. The initial GRP covariance $\mathbf{P}_0^{pp}$ and initial angular velocity covariance $\mathbf{P}_0^{\omega\omega}$ are given as

$$\mathbf{P}_0^{pp} = 0.0087 \cdot \mathbf{1}_{3\times3}$$
$$\mathbf{P}_0^{\omega\omega} = 0.0174 \cdot \mathbf{1}_{3\times3} \ \text{deg}^2/\text{s}^2$$

(3.53)

The filter bank assumes eight different MOI configurations detailed in Table 3.3. Four of the eight filters hypothesize that the payload is oriented at a constant angle, in the frame of the payload. The remaining four filters hypothesize a sinusoidal input command, similar to a gimbaled sweeping optical payload. The varying degrees of complexity in the trigonometric hypotheses are designed to test the adaptive estimator's ability to distinguish between frequency, amplitude, and function order among the filters. The time derivatives of the input commands required for the MOI models are easily calculated from the analytical expressions in Table 3.3. Figure 3.6 provides a time history of the eight different models in the bank.

Table 3.3: Filter bank for Scenario 2: Payload Input Command Identification. Input commands are given in degrees. Here, $\omega_\theta = 2\pi/t_f$, where t_f is the final simulation time, to ensure one period is completed during the simulation, and $\theta_{\max} = 20°$.

Filter	Input Command	Filter	Input Command
1	$\theta_{PL,1}(t) = 45°$	5	$\theta_{PL,5}(t) = \frac{\theta_{\max}}{2}\left(1 + \sin^2\left(0.1 \cdot \omega_\theta t\right)\right)$
2	$\theta_{PL,2}(t) = 10°$	6	$\theta_{PL,6}(t) = \theta_{\max}\cos\left(0.4 \cdot \omega_\theta t\right)$
3	$\theta_{PL,3}(t) = -45°$	7	$\theta_{PL,7}(t) = \theta_{\max}\left(1 - \cos^2\left(\omega_\theta t\right)\right)$
4	$\theta_{PL,4}(t) = 5°$	8 (True Model)	$\theta_{PL,8}(t) = \frac{\theta_{\max}}{2}\cos\left(\omega_\theta t\right)$

The results from a realization using MMAE are shown in Figure 3.7. The estimation scheme is able to identify the correct model after 3.5 minutes. Immediately following the near-unity likelihood value for Model 8, the MOI estimation error

71
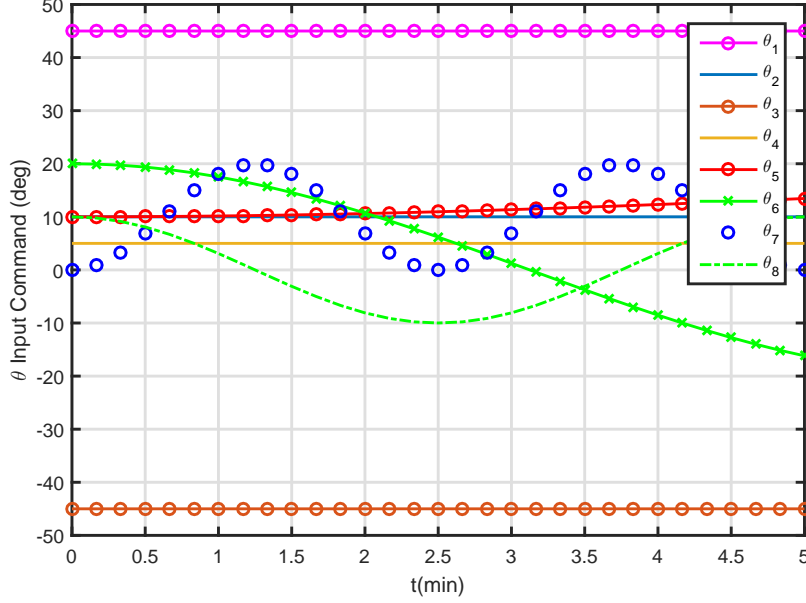
Figure 3.6: Depiction of the eight different input commands used as hypotheses in Scenario 2. For clarity, the input commands are plotted every five time steps.

approaches zero. The input angle parameter estimate also approaches the true value after identifying the correct model. The quaternion and angular velocity estimates have errors that are both $O(10^{-2})$. There is some conflict between Models 4 and 5, which differ by 5°, during the initial 3 minutes of the simulation, but the recursiveness of the MMAE routine allows for the correct selection of Model 8 after 3.5 minutes. Had a pruning or filter removal mechanism been employed in this realization, Model 8's likelihood would have been below realistic threshold values and would have been removed, rather than regaining its maximum likelihood.

The results from the same realization using the ALM algorithm are shown in Figure 3.8. The ALM method suffers a degraded performance when compared to the MMAE algorithm. The quaternion and angular velocity estimates are still $O(10^{-2})$ as the UKFs are still functioning filters, but the unknown system parameter is not well identified. The correct model is only the maximum likelihood for nearly a minute,

72
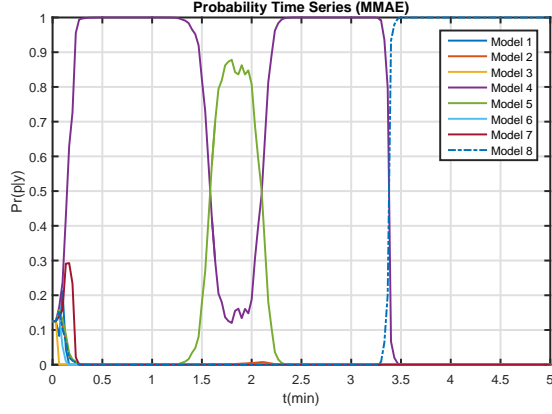
(a) Probability time series using MMAE
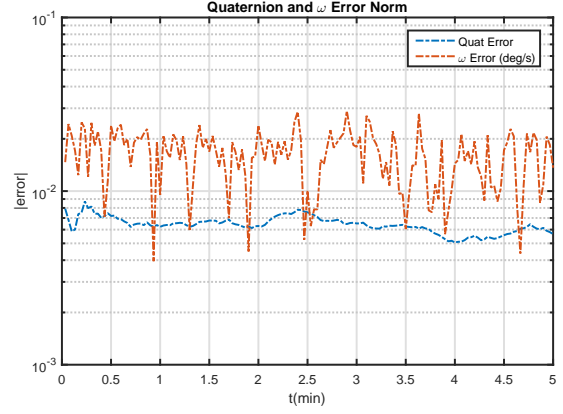
(b) Attitude and $\boldsymbol{\omega}$ Estimation Error
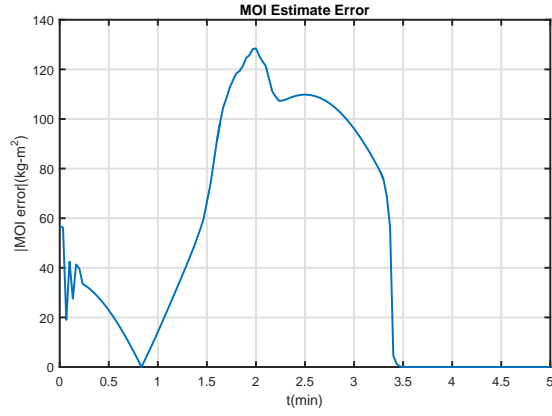
(c) MOI Estimation Error
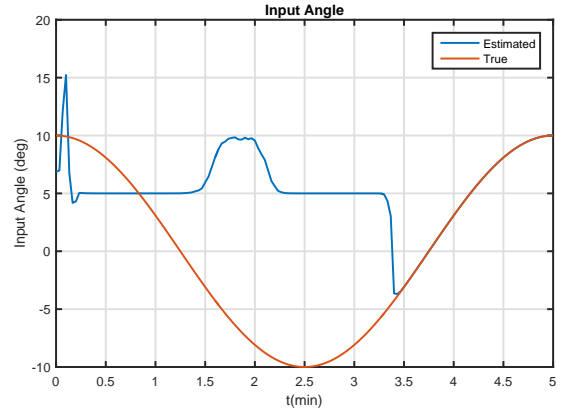
(d) Input Angle Estimation

Figure 3.7: Results from a realization of Scenario 2 using MMAE with $\boldsymbol{\omega}_0 = [3, 1.5, 1]^T$ deg/s. Model 8 contains the true dynamics.

and is outranked by competing models for the remainder of the simulation. This performance in identifying the correct model using ALM compares well with the results in [9]. The ALM method tends to equalize the likelihoods of all models over short propagation windows, but will tend to detect sudden changes over longer propagation windows. In the current example with propagations on the order of seconds, these appear to fall within the magnitude of propagation windows that lead to model equalization. This implies that ALM may not necessarily be the best general algorithm for attitude estimation, as the filtering fast rotational motions could lend to missing key dynamics.

For comparison, Scenario 2 is repeated exactly as previously described, but the initial angular velocity is modified to be $\boldsymbol{\omega}_0 = [3,3,3]^T$ deg/s. Figure 3.9 displays the results using the MMAE algorithm. The immediate result is Model 8's correct identification two minutes earlier than the slower initial conditions, which again leads to a near-zero estimation error of the input angle and MOI. The same simulation data is fed into an ALM algorithm, the results of which are plotted in Figure 3.10. The ALM results follow a similar trend from before in that models are equalized and the ALM method is definitely not optimal for the current situation. However, ALM and MMAE both identify Model 8 as the most likely model within nearly 1.5 minutes, but ALM's reinitialization equalizes the model probabilities after two minutes and the maximum likelihood model is no longer the true value. The faster initial conditions along the body 2- and 3-axes provide more variability in the information available to the adaptive estimator.

3.4.3 Results from Scenario 3: Payload Separation.

Scenario 3 examines the utility of various adaptive estimation schemes in identifying the correct structural configuration of a spacecraft given a series of three payload separations. Each payload is measured as a discontinuous loss of mass and
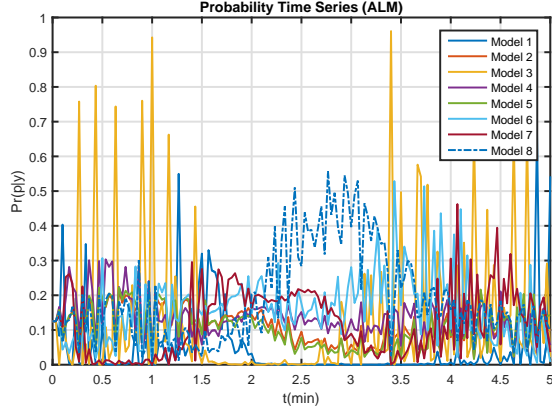
(a) Probability time series using ALM
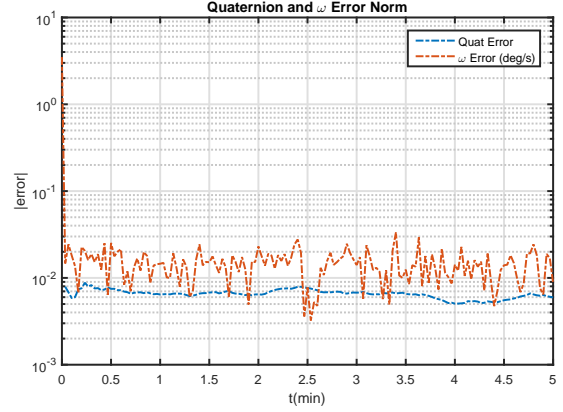
(b) Attitude and $\boldsymbol{\omega}$ Estimation Error
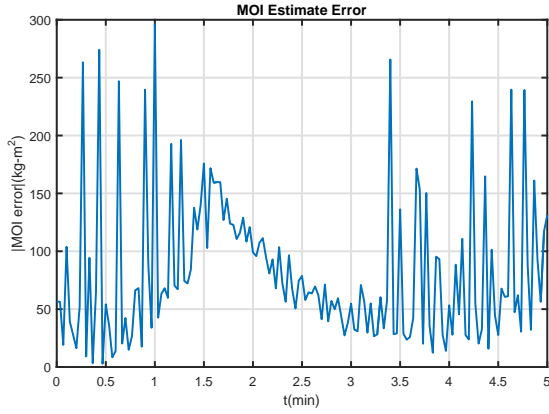
(c) MOI Estimation Error
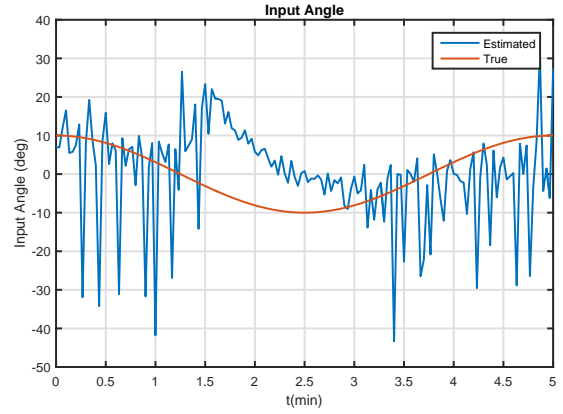
(d) Input Angle Estimation

Figure 3.8: Results from a realization of Scenario 2 using ALM with $\boldsymbol{\omega}_0 = [3, 1.5, 1]^T$ deg/s. Model 8 contains the true dynamics.
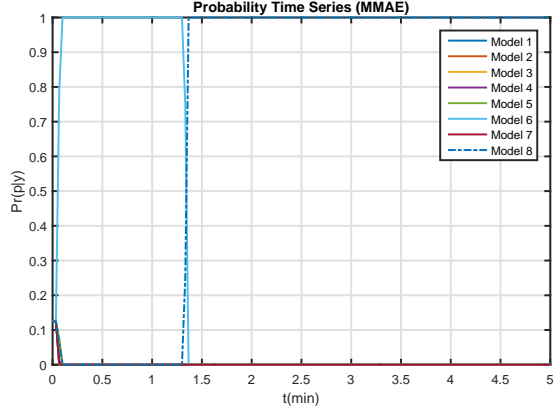
(a) Probability time series using ALM
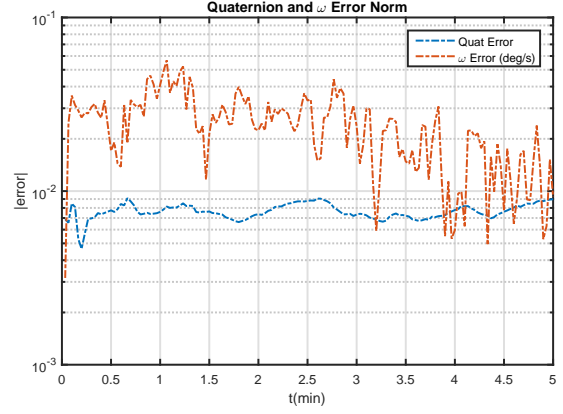
(b) Attitude and $\boldsymbol{\omega}$ Estimation Error
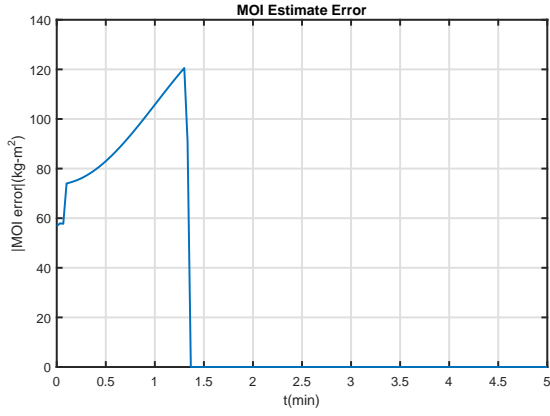
(c) MOI Estimation Error
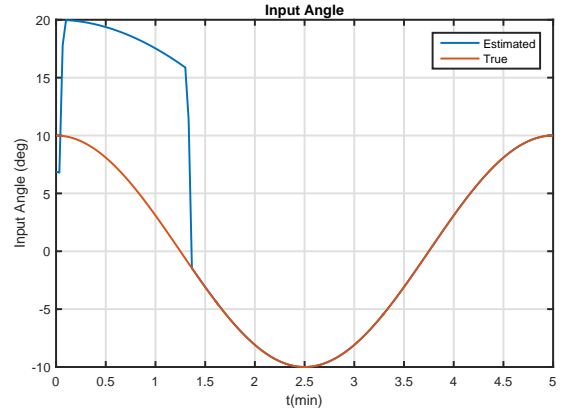
(d) Input Angle Estimation

Figure 3.9: Results from a realization of Scenario 2 with faster initial conditions using MMAE $\boldsymbol{\omega}_0 = [3, 3, 3]^T$ deg/s. Model 8 contains the true dynamics.
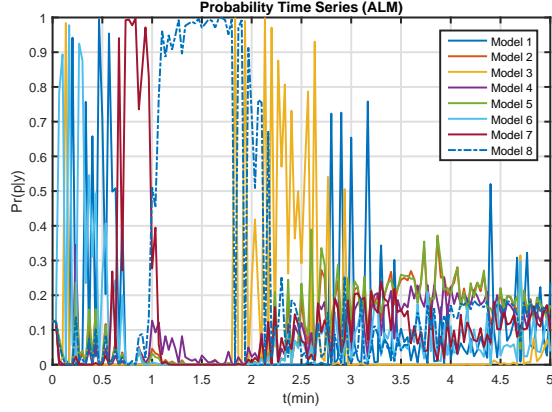
(a) Probability time series using ALM
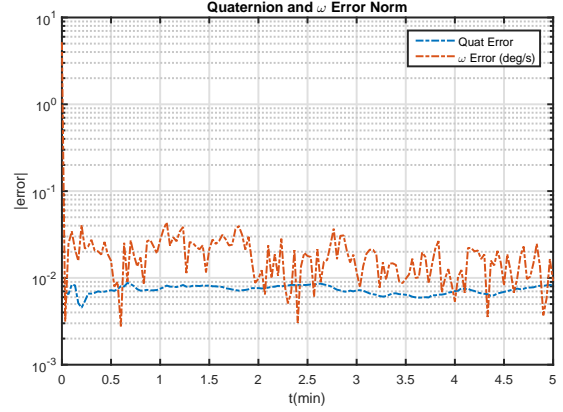
(b) Attitude and $\boldsymbol{\omega}$ Estimation Error
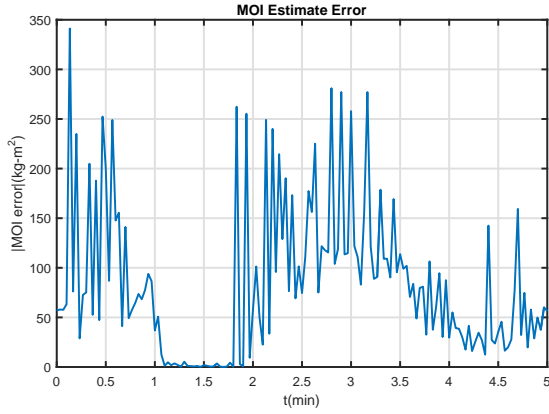
(c) MOI Estimation Error
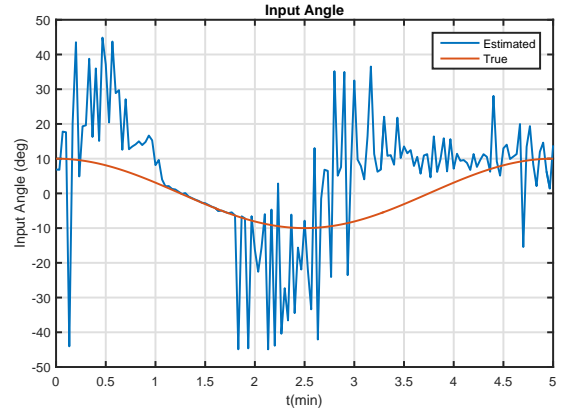
(d) Input Angle Estimation

Figure 3.10: Results from a realization of Scenario 2 with faster initial conditions using ALM $\boldsymbol{\omega}_0 = [3, 3, 3]^T$ deg/s. Model 8 contains the true dynamics.

change to MOI. The intent is to examine the different adaptive estimation schemes and identify which methods are more applicable to sudden changes in system dynamics and parameters. The filter bank will consist of four different models, all true at some point during the simulation time. Model 1 is true prior to the first payload separation, Model 2 is true between the first and second payload separations, Model 3 is true between the second and third payload separations, and Model 4 is true in the final configuration. The classical MMAE scheme, ALM, Soken's method, and the hybrid likelihood method will be evaluated in this scenario. A scenario time of 32 minutes is used with a constant time step Δt of one second. The initial spacecraft angular velocity and quaternion used in this scenario are

$$
\begin{aligned}
\boldsymbol{\omega}_0 &= \begin{bmatrix} 2 & 2 & 1 \end{bmatrix}^T \text{ deg/s} \\
\mathbf{q}_0 &= \begin{bmatrix} \sqrt{2}/2 & 0 & 0 & \sqrt{2}/2 \end{bmatrix}^{T}.
\end{aligned}
\tag{3.54}
$$

Initial estimation errors of 5% are added to both the angular velocity and quaternion for additional realism in initial estimates. Since the unscented filter is actually estimating the GRPs for the attitude states, and intermediate conversions are performed for the quaternions, the attitude covariance is actually describing the GRPs. The initial GRP covariance $\mathbf{P}_0^{pp}$ and initial angular velocity covariance $\mathbf{P}_0^{\omega\omega}$ are given as

$$
\begin{aligned}
\mathbf{P}_0^{pp} &= 0.0087 \cdot \mathbf{1}_{3\times 3} \\
\mathbf{P}_0^{\omega\omega} &= 0.0174 \cdot \mathbf{1}_{3\times 3} \text{ deg}^2/\text{s}^2
\end{aligned}
\tag{3.55}
$$

The filter bank assumes four different MOI configurations detailed in Table 3.4, and each model is are true at some point during the simulation. It is assumed that although the center of mass of the spacecraft will likely physically change following a separation, the MOI matrices are representative of the pre- and post-separation structures. The objective of this research was to examine sudden parameter change detection, and a more extensive effort for center of mass changes is required for

78

future research. Appendix B provides the finer details of the spacecraft model used to calculate the four different MOI configurations.

Table 3.4: Filter bank for Scenario 3: Payload Separation.

Filter	Spacecraft MOI (kg-m^2)		Relative MOI Ratio		Time Interval (sec)
1	$\mathbf{I}_1 = \begin{bmatrix} 770.5 & -100 & -200 \\ -100 & 834.5 & -40 \\ -200 & -40 & 589.5 \end{bmatrix}$		$\begin{bmatrix} 0.3944 \\ -0.6176 \\ 0.2951 \end{bmatrix}$		$[t_0, t_{\mathrm{sep},1}) = [0, 8)$
2	$\mathbf{I}_2 = \begin{bmatrix} 530.5 & -100 & 0 \\ -100 & 394.5 & -40 \\ 0 & -40 & 369.5 \end{bmatrix}$		$\begin{bmatrix} 0.1258 \\ -0.6831 \\ 0.6079 \end{bmatrix}$		$[t_{\mathrm{sep},1}, t_{\mathrm{sep},2}) = [8, 16)$
3	$\mathbf{I}_3 = \begin{bmatrix} 420 & 0 & 0 \\ 0 & 287 & -40 \\ 0 & -40 & 369.5 \end{bmatrix}$		$\begin{bmatrix} 0.3474 \\ -0.8930 \\ 0.7909 \end{bmatrix}$		$[t_{\mathrm{sep},2}, t_{\mathrm{sep},3}) = [16, 24)$
4	$\mathbf{I}_4 = \begin{bmatrix} 420 & 0 & 0 \\ 0 & 287 & -40 \\ 0 & -40 & 165 \end{bmatrix}$		$\begin{bmatrix} 0.3636 \\ -0.8750 \\ 0.7500 \end{bmatrix}$		$[t_{\mathrm{sep},3}, t_f) = [24, 32)$

A comparison of likelihood values from a realization of Scenario 3 are shown in Figure 3.11. The numbers (1,2,3,4) in each subfigure between sets of vertical lines indicate that model is true in that time interval. The individual data points indicate the likelihood of that model at a given time. In the MMAE and Soken charts (Figures 3.11a and 3.11c), the data points show as nearly horizontal lines as the estimators assign essentially a binary likelihood of 1 or 0 with intermediate transition values. The MMAE algorithm quickly identifies the correct model during Model 1's correct time interval, but is unable to adaptively switch modes until nearly 90% of the way through Model 2's correct time interval, after which the MMAE routine incorrectly

assigns Model 2 with unit probability when Models 3 and 4 are true. The ALM method does not detect the abrupt system changes, most likely due to the short propagation time in this scenario. The ALM method continues to essentially equalize models at each time step, but does assign the maximum likelihood to the correct model during brief periods. The Soken estimator quickly identifies the correct model, due to its inherent construction to adapt to sudden changes in the dynamics. The hybrid estimator performs similarly with quick adaption. There is competition for both the Soken and hybrid methods in differentiating between Models 3 and 4, which is attributed to the similarity of the assumed MOI matrices after the second and third payload separations, where the only change between Model 3 and 4 is a change in the I_{zz} component of the MOI.

The results from 30 realizations of five different iterations of Scenario 3 are tabulated in Tables 3.5 through 3.8. The scenario iteration examines the significance of the moving window length on model identification. It should be noted that the filter parameters were empirically tuned, as numerical instabilities do arise under numerous conditions. One common instability resulted from near singular covariance matrices for which a Cholesky decomposition often fails. The modifications to each filter parameter are described in the table captions. The evaluation metric is the percentage of time each adaptive estimation scheme correctly identifies the model, while the model is active, using the model with the maximum likelihood. The values for λ_1, λ_2 are held constant for a control with respect to the low-pass filter portion of the Soken and hybrid techniques. The values for $a, b,$ and β were empirically tuned for the current problem and prevent computational issues.

The first iteration of Scenario 3, with results found in Table 3.5, implemented a moving window length of 100 time steps. The ALM method recognizes the parameter change less than half the time, while the MMAE scheme typically recognizes the
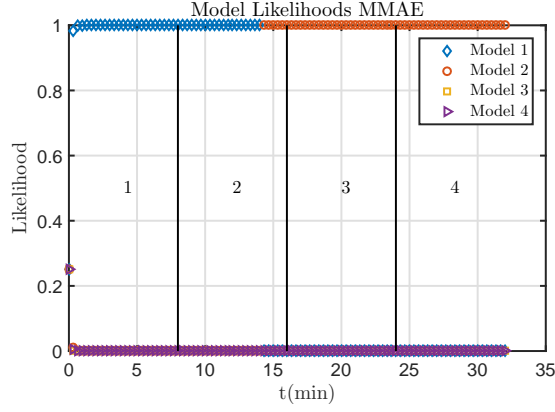
(a) MMAE likelihood values
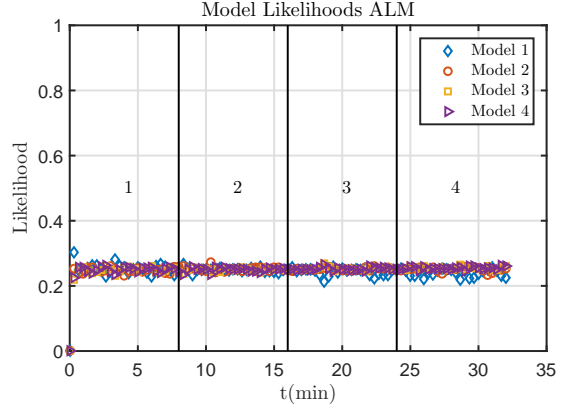
(b) ALM likelihood values
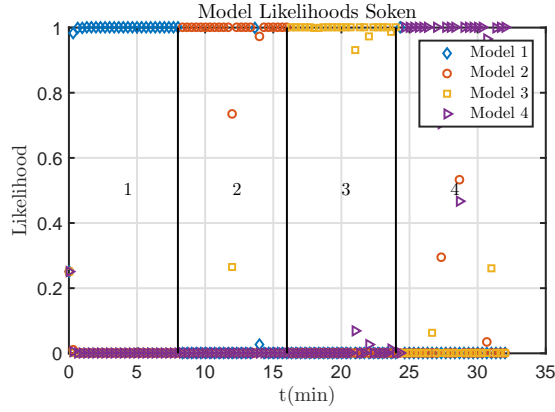
(c) Soken likelihood values
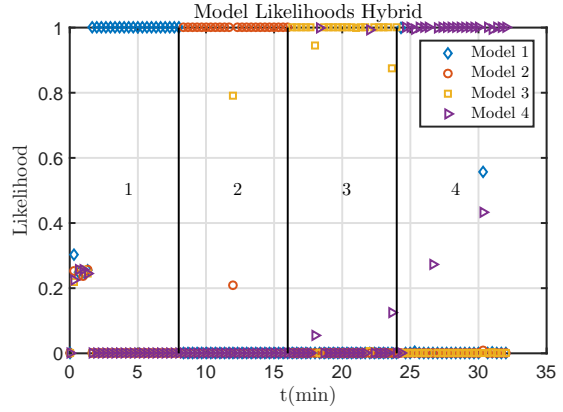
(d) Hybrid likelihood values

Figure 3.11: Comparison of model likelihoods for a realization of Scenario 3. The modified Soken and hybrid methods outperform MMAE and ALM for sudden change detection. $a = 1, b = 0, \lambda_1 = 0.997, \lambda_2 = 0.95, \beta = 0.05, \mu = 100$

correct model prior to the separations, but is unable to recover and the maximum MMAE likelihood is rarely the correct mode once payload separations begin. The Soken and hybrid schemes compare relatively equivalent, with Soken's outperforming the hybrid mode in three of the four configurations. Decreasing the moving window size by 80%, Table 3.6 tabulates the results for $\mu = 20$ time steps. Since μ only impacts the Soken and hybrid models, the results for the ALM and MMAE methods produce near similar results. The Soken and hybrid methods compare similarly, with the hybrid method identifying the correct model slightly (less than 2%) more often than the Soken scheme. A similar trend is noted for the remaining scenarios.

Table 3.5: Percent correct model identification using a maximum likelihood metric. Results are from 30 realizations of Scenario 3. $a = 1, b = 0, \lambda_1 = 0.997, \lambda_2 = 0.95, \beta = 0.05, \mu = 100$

Model	ALM	MMAE	Soken	Hybrid
1	37%	99%	98%	99%
2	37%	≈0%	93%	95%
3	41%	≈0%	90%	89%
4	50%	≈0%	91%	89%

The general trend among the various results points to the efficacy of the Soken and hybrid likelihood methods in terms of detecting sudden parameter changes. The MMAE scheme appears to often suffer from a lock-out, or inability to recover from models whose likelihoods have been reduced to essentially zero. The ALM method is able to eventually adopt to the sudden parameter changes, and on longer time scales the ALM is likely to increase in accuracy. The Soken and hybrid methods

Table 3.6: Percent correct model identification using a maximum likelihood metric. Results are from 30 realizations of Scenario 3. $a = 1, b = 0, \lambda_1 = 0.997, \lambda_2 = 0.95, \beta = 0.05, \mu = 20$

Model	ALM	MMAE	Soken	Hybrid
1	37%	99%	99%	98%
2	39%	1%	92%	94%
3	40%	$\approx$0%	92%	93%
4	50%	$\approx$0%	95%	91%

Table 3.7: Percent correct model identification using a maximum likelihood metric. Results are from 30 realizations of Scenario 3. $a = 1, b = 0, \lambda_1 = 0.997, \lambda_2 = 0.95, \beta = 0.05, \mu = 150$

Model	ALM	MMAE	Soken	Hybrid
1	39%	98%	98%	98%
2	37%	1%	91%	94%
3	44%	1%	86%	86%
4	49%	$\approx$0%	89%	86%

Table 3.8: Percent correct model identification using a maximum likelihood metric. Results are from 30 realizations of Scenario 3. $a = 1, b = 0, \lambda_1 = 0.997, \lambda_2 = 0.95, \beta = 0.05, \mu = 200$

Model	ALM	MMAE	Soken	Hybrid
1	34%	97%	99%	99%
2	32%	2%	95%	95%
3	33%	$\approx$0%	94%	92%
4	43%	$\approx$0%	95%	92%

compare, overall, very similarly, indicating that the weighted state and covariance filter reinitialization does not introduce significant improvement to the algorithm, but over long time scales, or in a different set of dynamics, could increase the detection accuracy.

3.5 Conclusions and Future Work

The purpose of the numerical experiment presented in this chapter was to analyze the new application of adaptive estimation techniques to the time-varying spacecraft MOI problem. Three different scenarios were analyzed. The first scenario sought the identification of a spacecraft's relative MOI ratios, the driving parameter for torque-free rigid body motion. The second scenario sought the identification of a continuous command input for a gimbaling and deployable payload. The third scenario examined a series of separating payloads, each producing a discontinuity in the spacecraft MOI. A hybrid between two adaptive estimation schemes was developed that, for this scenario, exhibits approximately the same performance as the Soken algorithm. This similar performance is likely a function of the propagation step, as the ALM hybrid component detects sudden dynamics changes over long propagation windows.

Some key findings from this work resulted in the need for rotational information about the three axes and the difficulty in estimating when unavailable, and also the need for variability and diversity in the filter bank. Another key finding was the change in dynamics must be greater than the noise floor, otherwise it is likely the estimator will account for the dynamical changes by compensating in noise rejection calculations. Specific future work pertaining to this numerical experiment will be detailed in Chapter 6. To the extent of the author's knowledge, this application of adaptive estimation to detect MOI changes has not been applied before and the research is a new contribution to the field. This research allowed for the use of streaming attitude data to estimate structural changes and has served as an initial

proof of concept, ultimately laying the foundation for future experimental work examining spacecraft MOI change detection via adaptive attitude estimation.

IV. Alternate Numerical Solutions to Wahba's Problem of Sequential Frame Attitude Estimation Using Heuristic Optimization and Fast Quartic Numerical Solvers

Grace Wahba posed the satellite attitude determination problem as a least-squares optimization problem in 1965 [20]. That is, given N sets of simultaneous vector measurements in two different reference frames, Wahba's problem seeks to approximate the rotation matrix between the two frames that minimizes a particular cost function. This rotation matrix defines the current attitude estimate. Classical numerical solutions to Wahba's problem include Davenport's q-method [21], TRIAD [22], QUEST [23], and several other techniques [24]. This research evaluates the application of Strobach's Fast Quartic Solver [18] to quickly solve a fourth-order eigenvalue problem required for the quaternion attitude estimate. Additionally, this work examines the application of heuristic based techniques, to include particle swarm optimization (PSO) and genetic algorithms (GA), to solve Wahba's minimization problem to estimate spacecraft attitude. As previously mentioned, the reader may notice some repetition between the presented motivation and background.

4.1 Introduction and Motivation

To define orientation in a three-dimensional space, one needs three independent parameters. A single vector measurement will provide two independent parameters, as a unit vector constraint removes a DOF, while two vector measurements will provide at least four quantities, making the problem overdetermined. As no general closed form solution exists, the attitude determination problem becomes an attitude estimation problem, especially in the presence of measurement and process noise. An attitude solution using single frame estimation techniques is not possible for an underdetermined single set of measurements. However, when two or

more observations are available, the attitude determination problem is numerically solvable, and Wahba's problem seeks to estimate the current attitude by minimizing a particular cost function to compute a rotation matrix.

The accuracy from coupling a spacecraft's attitude within an orbital state propagator is limited by the accuracy of the attitude estimate. The attitude dynamics of a rigid (or flexible) body are highly nonlinear, coupled, and sensitive to particular system parameters such as the spacecraft MOI [7]. Accurate attitude determination and the tight coupling between the MOI and the rotational motion of the spacecraft is of concern to SSA operators. Miscalculation of the spacecraft orientation, changes in MOI, or assumptions of rigidity could directly contributed to the observed effect of non-gravitational perturbations on an orbit and the consequential error and state covariance growth.

In the single frame attitude estimation problem made famous by Wahba in [20], knowledge of the spacecraft MOI is not necessarily required, as the rotation matrix between two reference frames is computed based upon unit vector measurements. Some recursive filters have produced hybrid estimation routines where the single frame problem becomes an intermediate step [101]. Numerous estimation routines exist to solve the single frame problem, and the solution method often relies on the parameterization of the rotation matrix, whether by quaternions, Euler angles, Rodriguez parameters, etc. Section 2.1.3 provides an overview of the various attitude parameters. Quaternion parameterizations often lead to a quartic eigendecomposition problem, the characteristic equation of which is solved in some instances analytically [44], or via numerical techniques like Newton-Raphson in QUEST [23].

Wahba's attitude estimation problem resembles a least-squares minimization problem, and has recently been shown to be a total least-squares problem [102], allowing for ways to more elegantly express covariance structures, which is not

investigated in this research. The least-squares minimization problem motivates the application of different optimization techniques to estimate the optimal attitude solution. One limitation common in many optimization routines is the need for a suitable initial guess, and when a 'close' initial guess is provided, may find themselves converging in a local optimal solution. Evolutionary or heuristic optimization algorithms have a key advantage in this regard in that an initial guess is often randomly generated and are more likely, but not guaranteed, to converge on locally, if not globally, optimal solutions [76; 79; 82].

This presented research is aimed at decreasing the computation time required to solve Wahba's problem by the application of Strobach's FQS algorithm. Additionally, this work seeks to demonstrate the application of heuristic techniques to solve the single frame attitude estimation problem. Section 4.2 provides a literature review of current attitude estimation techniques. From an application perspective, operational spacecraft are unlikely to employ the coding environment (Matlab) used to benchmark in this research; however, similar open-source platforms such as Python are possibilities. Specifics of the algorithms applied are also discussed in Section 4.2. Section 4.3 details the flow of numerical simulations and the evaluation metrics used. Section 4.4 details the results from various simulations. Finally, Section 4.5 summarizes the conclusions made in this research.

4.2   Background

The current research in Chapter 4 examines the fields of single-frame attitude determination and heuristic optimization. Chapter 2 provided an in-depth discussion of attitude determination in Section 2.3 that is recreated and expanded upon in this section. For background information regarding heuristic optimization, the reader is referred to Section 2.6. The discussion reveals a dichotomy in the attitude estimation problem: on one side are the recursive filtering methods used in Chapter 3, and on

the other side are the single frame estimation methods discussed in this chapter. The following section provides a discussion on Wahba's problem, which is the classical example of single frame estimation, and also discusses classical solution techniques. This section provides a discussion on the heuristic optimization schemes and quartic root solvers used in this research.

4.2.1 Wahba's Problem and Classical Numerical Solutions.

When two or more vector observations are available, the attitude determination problem is overdetermined [22]. This formulation lends to computing a rotation matrix (attitude) to minimize a loss function of these measurements. One loss function is often defined as Wahba's problem [20; 22; 24], and is given as

$$J\left(\mathbf{R}^{bi}\right) = \frac{1}{2} \sum_{k=1}^{N} w_k \left|\left|\mathbf{v}_{kb} - \mathbf{R}^{bi}\mathbf{v}_{ki}\right|\right|^2 \tag{4.1}$$

where J is the loss function, k is the index for the N observations, w_k is the observation weight, $\mathbf{v}_{kb}$ is k^{th} vector of body frame components, $\mathbf{v}_{ki}$ is the kth vector of components in the inertial frame, and $\mathbf{R}^{bi}$ is the rotation matrix to be found to minimize J. There are three commonly referenced solutions to this problem: (1) a numerical minimization approach using Lagrange multiplers; (2) an exact analytical solution in the eigenspace known as the q-method; and (3) an eigenspace approximation method known as QUEST.

In the numerical approximation to minimizing J, Wahba's problem generally involves the standard appendage of Lagrange multipliers with the unity norm quaternion constraint, a Jacobian, and a Newton-Raphson iteration [22]. Davenport's q-method [22] rewrites Wahba's minimization problem $(\min J(\mathbf{R}^{bi}))$ as a maximization of a gain function, where quaternions are the independent variables (i.e., $\max g(\mathbf{q})$). Appending the quaternion norm constraint leads to an eigenvalue problem, where the eigenvector corresponding to the eigenvalue maximizing the gain function is the optimal attitude estimate [22].

Shuster expanded Davenport's q-method with QUEST by providing an iterative numerical solution to find the maximum eigenvalue [23]. Rearranging the gain function derived from Wahba's problem, an initial guess for the optimal eigenvalue can be approximated as the sum of the weights w_k, and the corresponding eigenvector can be iteratively determined. Crassidis claims that often only a single iteration is required for the QUEST solution to converge [24], but when noise is present the number of iterations can be much greater [44]. While the QUEST algorithm is less robust than the q-method, QUEST has proven more reliable and computationally efficient than the q-method [24]. Psiaki modified Shuster's work with Extended QUEST [45] to allow for the estimation of other states (e.g., gyro bias) by modifying the cost function and implementing information filtering algorithms. Although these methods have minimized a loss function, there is no guarantee that the actual attitude error is minimized [22].

Wahba's problem is, at its core, an optimization problem where the control variable is the rotation matrix, and the cost function is essentially a least-squares formulation given in Eq. (4.1). Solving directly for the rotation matrix is a constrained nonlinear optimization problem, where the constraint is matrix orthonormality (i.e. $\mathbf{R}^{bi} \in \mathcal{SO}(3)$, the special orthogonal group in three dimensions). The rotation matrix requires solving for nine design variables that also satisfy the orthonormality constraint. The classical circumvention of this is to reduce the dimension of the problem by parameterizing the attitude rotation matrix with the quaternion. After some algebraic manipulation, the cost function J can be expressed as

$$J(\mathbf{R}^{bi}) = \lambda_0 - g(\mathbf{R}^{bi}) = \lambda_0 - \text{tr}\left[\mathbf{B}^T\mathbf{R}^{bi}\right] \tag{4.2}$$

where

$$\lambda_0 = \sum_{k=1}^{N} w_k$$
$$\mathbf{B} = \sum_{k=1}^{N} w_k \mathbf{v}_{kb} \mathbf{v}_{ki}^T$$
(4.3)

and the operator $\text{tr}\,[\cdot]$ is the trace operation, or the sum of diagonal elements of a matrix. The matrix $\mathbf{B}$ is often termed the attitude profile matrix as it contains the actual data measurements and sensor weights. In order to minimize J, the loss function $g(\mathbf{R}^{bi}) = \text{tr}\left[\mathbf{B}^T \mathbf{R}^{bi}\right]$ should be maximized. Davenport showed that the loss function could be written in quadratic form as [21; 103]

$$g(\mathbf{R}^{bi}) = g(\mathbf{q}) = \mathbf{q}^T \mathbf{K} \mathbf{q}$$
(4.4)

where the matrix $\mathbf{K}$ is given as

$$\mathbf{K} = \begin{bmatrix} \mathbf{S} - s\mathbf{I}_{3\times3} & \mathbf{Z} \\ \mathbf{Z}^T & s \end{bmatrix},$$
(4.5)

with the intermediate variables defined as

$$s = \text{tr}\,[\mathbf{B}]$$
$$\mathbf{S} = \mathbf{B} + \mathbf{B}^T$$
$$\mathbf{Z} = \begin{bmatrix} \mathbf{B}_{23} - \mathbf{B}_{32} & \mathbf{B}_{31} - \mathbf{B}_{13} & \mathbf{B}_{12} - \mathbf{B}_{21} \end{bmatrix}.$$
(4.6)

The optimization problem takes the form

$$\underset{\mathbf{q}}{\text{maximize}} \quad g(\mathbf{q}) = \mathbf{q}^T \mathbf{K} \mathbf{q}$$
$$\text{subject to} \quad \mathbf{q}^T \mathbf{q} = 1$$

Appending the quaternion unit norm constraint to the quadratic $\mathbf{q}^T \mathbf{K} \mathbf{q}$ equation results in

$$g(\mathbf{q}) = \mathbf{q}^T \mathbf{K} \mathbf{q} + \lambda \left(1 - \mathbf{q}^T \mathbf{q}\right).$$
(4.7)

91

A first-order optimization on the loss function g is found by taking the partial of $g(\mathbf{q})$ with respect to both the quaternion vector and the Lagrange multiplier. This differentiation is then found as

$$\frac{\partial \mathbf{q}^T \mathbf{K} \mathbf{q}}{\partial \mathbf{q}} = 2\mathbf{K}\mathbf{q}^T - 2\lambda \mathbf{q}^T = \mathbf{0}$$
$$\frac{\partial \mathbf{q}^T \mathbf{K} \mathbf{q}}{\partial \lambda} = (1 - \mathbf{q}^T \mathbf{q}) = 0$$

$$(4.8)$$

Solving the first of Eq. (4.8) results in

$$\mathbf{K}\mathbf{q} = \lambda \mathbf{q}, \tag{4.9}$$

which implies the optimal quaternion is the eigenvector associated with the largest eigenvalue of $\mathbf{K}$ matrix. Typically, this is solved by a Newton-Raphson technique and converges best when the initial guess is taken as the sum of the sensor weights. When the weights have been normalized such that the sum is one, the initial guess is unity. Solving the second equation of Eq. (4.8) retrieves the quaternion unit norm constraint.

The characteristic polynomial of the $\mathbf{K}$ matrix has previously been derived using Cayley-Hamilton in [44; 103] and is presented as

$$L(x) = x^4 + ax^3 + bx^2 + cx + d = 0 \tag{4.10}$$

where x is used to represent the eigenvalues rather than λ, and the coefficients are given as

$$a = 0$$
$$b = 2(\text{tr}[\mathbf{B}])^2 + \text{tr}[\text{adj}(\mathbf{S})]$$
$$c = -\text{tr}[\text{adj}(\mathbf{K})]$$
$$d = \det(\mathbf{K})$$

$$(4.11)$$

The a coefficient removes the cubic dependency from the characteristic equation, while the characteristic equation remains highly dependent on the attitude profile

92

matrix $\mathbf{B}$ as well as the $\mathbf{K}$ matrix. The optimal quaternion is then constructed using the Gibbs vector in an algorithm described in Shuster's work [23]. The Gibbs vector becomes infinite near $\pm\pi$ rotations and care must be taken to handle this singularity [23], such as the method of single frame rotations [23; 104]. The current research will focus on attitude estimates away from the singularities in these methods as a means of benchmarking performance, while it is noted that the proposed algorithms are easily modified to allow for singular scenarios.

4.2.2 Fast Quartic Solver.

The following section will detail the specifics of Strobach's FQS algorithm used in this research. Strobach introduced in [18] the Fast Quartic Solver (FQS), a numerical algorithm to tackle quartic equations efficiently and accurately. Although closed form quartic solution schemes exists such as Ferrari's [105], Strobach claims an unsuitability for stiff quartics with a large root spread [18] due to significant round off errors when implemented. The method employs the factorization of a quartic into the product of two quadratics with closed-form solutions. A fixed-point iteration is then used to fit the quartic-quadratic decomposition. The algorithm essentially iterates on the decomposed quadratic coefficients to fit the quartic function until a desired tolerance is reached, or the fitting error is minimized. Given a quartic polynomial of the form

$$
\begin{aligned}
f(x) &= x^4 + ax^3 + bx^2 + cx + d \\
&= \left(x^2 + \alpha x + \beta\right)\left(x^2 + \gamma x + \delta\right) \qquad , \\
&= (x - x_1)(x - x_2)(x - x_3)(x - x_4)
\end{aligned}
\tag{4.12}
$$

where (a, b, c, d) are coefficients of the quartic polynomial, $(\alpha, \beta, \gamma, \delta)$ are coefficients to the decomposed quadratic polynomials, and (x_1, x_2, x_3, x_4) are the roots to the fourth-order polynomial, a relation can be developed among the coefficients. Expanding the decomposed quadratics back to a quartic relation, the following equality results among

the polynomials in quartic form

$$f(x) = \left(x^2 + \alpha x + \beta\right)\left(x^2 + \gamma x + \delta\right)$$

$$= x^4 + (\alpha + \gamma)x^3 + (\beta + \alpha\gamma + \delta)x^2 + (\beta\gamma + \alpha\delta)x + (\beta\delta). \tag{4.13}$$

$$= x^4 + ax^3 + bx^2 + cx + d$$

Equality must hold among the coefficients in both polynomials, and the resulting relation can be constructed

$$\begin{bmatrix} 1 \\ a \\ b \\ c \\ d \end{bmatrix} = \begin{bmatrix} 1 & 0 & 0 \\ \alpha & 1 & 0 \\ \beta & \alpha & 1 \\ 0 & \beta & \alpha \\ 0 & 0 & \beta \end{bmatrix} \begin{bmatrix} 1 \\ \gamma \\ \delta \end{bmatrix} = \begin{bmatrix} 1 \\ \alpha + \gamma \\ \beta + \alpha\gamma + \delta \\ \beta\gamma + \alpha\delta \\ \beta\delta \end{bmatrix}. \tag{4.14}$$

If the quadratic coefficients do not produce an immediate fit, an error vector $\mathbf{e}$ of the following form results

$$\mathbf{e} = \begin{bmatrix} e_1 \\ e_2 \\ e_3 \\ e_4 \end{bmatrix} = \begin{bmatrix} a - (\alpha + \gamma) \\ b - (\beta + \alpha\gamma + \delta) \\ c - (\beta\gamma + \alpha\delta) \\ d - \beta\delta \end{bmatrix}. \tag{4.15}$$

The variables $(\alpha, \beta, \gamma, \delta)$ are the design variables to be iterated on. A Jacobian can now be found with respect to the design variables

$$\mathbf{J} = \begin{bmatrix} \frac{\partial e_1}{\partial \alpha} & \frac{\partial e_1}{\partial \beta} & \frac{\partial e_1}{\partial \gamma} & \frac{\partial e_1}{\partial \delta} \\ \frac{\partial e_2}{\partial \alpha} & \frac{\partial e_2}{\partial \beta} & \frac{\partial e_2}{\partial \gamma} & \frac{\partial e_2}{\partial \delta} \\ \frac{\partial e_3}{\partial \alpha} & \frac{\partial e_3}{\partial \beta} & \frac{\partial e_3}{\partial \gamma} & \frac{\partial e_3}{\partial \delta} \\ \frac{\partial e_4}{\partial \alpha} & \frac{\partial e_4}{\partial \beta} & \frac{\partial e_4}{\partial \gamma} & \frac{\partial e_4}{\partial \delta} \end{bmatrix} = \begin{bmatrix} 1 & 0 & 1 & 0 \\ \gamma & 1 & \alpha & 1 \\ \delta & \gamma & \beta & \alpha \\ 0 & \delta & 0 & \beta \end{bmatrix}. \tag{4.16}$$

A modified Newton-Raphson method is then constructed for a fixed point iteration on the design variables where the update equation is

$$\mathbf{p}^{j+1} = \mathbf{p}^j - \mathbf{J}^{-1}\mathbf{e}^j \tag{4.17}$$

94

where $\mathbf{p}$ is the vector of design variables $(\alpha, \beta, \gamma, \delta)$. The update term $\mathbf{J}^{-1}\mathbf{e}^j$ can be expressed as an update vector $\mathbf{y}$, and the update equation equivalently given as

$$\mathbf{p}^{j+1} = \mathbf{p}^j + \mathbf{y} \tag{4.18}$$

where $-\mathbf{J}\mathbf{y} = \mathbf{e}$. This presents a system of linear equations to solve for the update vector $\mathbf{y}$. The concatenated band structure of the Jacobian is then exploited to solve the system with LU-factorization of the Jacobian to produce rapid updates to the design variable vector. Complete details of the algorithm can be found in Strobach's work [18] to also include scenarios of repeated and complex roots. For the purposes of this research, Eq. (4.18) is utilized until the 2-norm of the error vector $\mathbf{e}$ is below a certain tolerance.

4.3 Methodology

The following section will detail the methodology employed in this research in order to perform attitude estimation on simulated data with the PSO, GA, and FQS algorithms.

4.3.1 Fast Quartic Solver Methodology.

A series of test cases constructed by Markley are readily available in the literature [17]. The cases are specifically designed to be representative of various sensor combinations, number of observations, and noise levels. A Newton-Raphson QUEST solution, a built-in Matlab eigenvalue calculation representing the q-method, and the new FQS method will be compared among the various test cases for 10000 simulations each in a Matlab environment. The full textual description of the test cases are in Markley's work [17]. This research will examine eight of the twelve test cases presented in [17] described in Table 4.1. The measured vectors will be of the form

$$\mathbf{v}_{b,k} = \mathbf{R}^{bi}\mathbf{v}_{i,k} + \mathbf{n}_k \tag{4.19}$$

where $\mathbf{n}_k$ is a zero-mean Gaussian vector used to simulate measurement noise whose covariance is described by the given σ values in Table 4.1. The methodological flow of numerical simulations used to evaluate the FQS compared to classical estimation methods initially consists of the construction of noisy vector measurements. Each set of measurements is then used to develop the $\mathbf{K}$ matrix previously described. Classical numerical attitude estimation methods are applied to the $\mathbf{K}$ matrix and compared to the results of the FQS algorithm using the metrics described in Section 4.3.3. The maximum root of the characteristic polynomial of $\mathbf{K}$ is then taken as the maximum eigenvalue. For comparison, the optimal quaternion is then determined for the FQS and QUEST method by using the Gibbs vector. The true rotation matrix for this numerical experiment is given as

$$\mathbf{R} = \begin{bmatrix} 0.352 & 0.864 & 0.360 \\ -0.864 & 0.152 & 0.480 \\ 0.360 & -0.480 & 0.800 \end{bmatrix} \tag{4.20}$$

which is associated the quaternion

$$\mathbf{q}^T = \begin{bmatrix} 0.3162 & 0 & 0.5692 & 0.7589 \end{bmatrix}. \tag{4.21}$$

Each measurement will be weighted relatively by its calibrated sensor noise, where the sensor weight w_i is given as

$$w_i = \frac{1}{N} \tag{4.22}$$

whereas the other case will weight the sensors by their known calibrated noise values as

$$w_i = \frac{1/\sigma_i}{\sum_{i=1}^{N} 1/\sigma_i}. \tag{4.23}$$

Table 4.1: Simulated sensor data used in the test cases.

Case	Measurements (i **Frame**)	Noise (rad)
1	$\mathbf{v}_1 = [1,0,0]^T, \mathbf{v}_2 = [0,1,0]^T, \mathbf{v}_3 = [0,0,1]^T$	$\sigma_1 = \sigma_2 = \sigma_3 = 10^{-6}$
2	$\mathbf{v}_1 = [1,0,0]^T, \mathbf{v}_2 = [0,1,0]^T$	$\sigma_1 = \sigma_2 = 10^{-6}$
3	$\mathbf{v}_1 = [1,0,0]^T, \mathbf{v}_2 = [0,1,0]^T, \mathbf{v}_3 = [0,0,1]^T$	$\sigma_1 = \sigma_2 = \sigma_3 = 10^{-2}$
4	$\mathbf{v}_1 = [1,0,0]^T, \mathbf{v}_2 = [0,1,0]^T$	$\sigma_1 = \sigma_2 = 10^{-2}$
5	$\mathbf{v}_1 = [0.6,0.8,0]^T, \mathbf{v}_2 = [0.8,-0.6,0]^T$	$\sigma_1 = 10^{-6}, \sigma_2 = 10^{-2}$
6	$\mathbf{v}_1 = [1,0,0]^T, \mathbf{v}_2 = [1,10^{-2},0]^T, \mathbf{v}_3 = [1,0,10^{-2}]^T$	$\sigma_1 = \sigma_2 = \sigma_3 = 10^{-6}$
7	$\mathbf{v}_1 = [1,0,0]^T, \mathbf{v}_2 = [1,10^{-2},0]^T$	$\sigma_1 = \sigma_2 = 10^{-6}$
8	$\mathbf{v}_1 = [1,0,0]^T, \mathbf{v}_2 = [0.96,0.28,0]^T, \mathbf{v}_3 = [0.96,0,0.28]^T$	$\sigma_1 = 10^{-6}, \sigma_2 = \sigma_3 = 10^{-2}$

4.3.2 Heuristic Optimization Methodology.

The methodology to assess the performance of the PSO and GA methods to minimize Wahba's problem differs slightly than that of Section 4.3.1. Rather than testing individual cases, a true attitude is given, and N random measurement vectors are created using Eq. (4.19) using various sensor noise levels. Each sensor producing any of the N observations will be assumed to have equivalent noise levels. Six noise levels will be investigated for N observations for the three algorithms with 1000 simulations each. This produces a total of $6 \cdot 3 \cdot (N-1) \cdot 1000$ simulations for the heuristic optimization experiments. The true attitude used in the heuristic optimization simulations is

$$\mathbf{q}^T = \begin{bmatrix} \frac{\sqrt{2}}{2} & 0 & 0 & \frac{\sqrt{2}}{2} \end{bmatrix}, \tag{4.24}$$

which corresponds to the rotation matrix

$$\mathbf{R} = \begin{bmatrix} 1 & 0 & 0 \\ 0 & 0 & 1 \\ 0 & -1 & 0 \end{bmatrix}. \tag{4.25}$$

The default social, cognitive, and inertial parameters in Matlab's PSO algorithm are used, as are the default values of the GA method. For this experiment, each sensor is weighted equally. Rather than constructing the $\mathbf{K}$ matrix, Wahba's least-squares cost function is then directly minimized using a quaternion parameterization of the rotation matrix. Only the first three components of the quaternion are used as design variables, as the fourth is immediately found by using the unit norm constraint. That is, (q_1, q_2, q_3) are iterated on in the heuristic optimization, and q_4 is found by

$$q_4 = \sqrt{1 - q_1^2 - q_2^2 - q_3^2} \tag{4.26}$$

assuming the positive root.

4.3.3 Comparison Metrics.

For comparison metrics, both the FQS and heuristic investigations use execution time and a principal error angle. Average computation time using Matlab's *tic-toc* command will be one performance metric. As a means of computing *tic-toc* resolution, 10^6 instances of the *tic-toc* command were executed, generating an average computation time of 3.3×10^{-7} seconds and a standard deviation of 1.4×10^{-6} seconds. Based on these values, results above a threshold of 10^{-6} seconds will be considered within the resolution of *tic-toc* for the purposes of this research. For reference, numerical simulations are carried out in Matlab 2015b on a 64-bit Intel Core i5 at 2.20 GHz with 8.00 GB RAM.

Another performance metric will be the difference in principal angle in the known attitude and the estimated attitude taken from Forbes [106], given as

$$\phi_e = \cos^{-1}\left(\frac{1}{2}\left(\text{tr}\left[\mathbf{R}_e\right] - 1\right)\right), \tag{4.27}$$

where the matrix $\mathbf{R}_e$ is an error matrix calculated as

$$\mathbf{R}_e = \hat{\mathbf{R}}\mathbf{R}^T, \tag{4.28}$$

where $\mathbf{R}$ is the true rotation matrix and $\hat{\mathbf{R}}$ is the estimated rotation matrix that is determined from the optimal quaternion estimate. The orthonormality property of the rotation matrix implies that as the estimated rotation matrix $\hat{\mathbf{R}}$ approaches the true value, the error rotation matrix will approach the identity matrix. Examining Eq. (4.28), if $\mathbf{R}_e = \mathbf{1}_{3 \times 3}$,

$$\begin{aligned} \phi_e &= \cos^{-1}\left(\frac{1}{2}\left(\text{tr}\left[\mathbf{1}_{3 \times 3}\right] - 1\right)\right) \\ \phi_e &= \cos^{-1}(1) \\ \phi_e &= 0 \end{aligned} \qquad (4.29)$$

As the estimated rotation matrix approaches the true value and the error matrix approaches identity, the principal angle error approaches zero and provides a scalar metric to quantify the current problem. The number of iterations and generations produced during the PSO and GA experiments will be recorded, as well as the final value of the cost function.

4.4 Results and Discussion

This section will provide results and discussion for the application of FQS and heuristic optimization to the single frame attitude estimation problem. Section 4.4.1 will detail the results of the FQS application, while Section 4.4.2 will detail the results of the heuristic optimization techniques.

4.4.1 Numerical Results Using FQS.

The three different estimation algorithms (FQS, QUEST, q-method) are applied to the eight single frame cases in Table 4.1 for 10,000 runs each. The eight cases are used to construct the 4×4 $\mathbf{K}$ matrix given in Eq. (4.5). The three different schemes are then used to solve the quartic eigen-decomposition problem. The optimal quaternion is then found as the eigenvector associated with the maximum eigenvalue, constructed via the Gibbs vector. Rather than examining the individual simulations

case by case, a more intuitive metric are the average values of solution time and error angle ϕ_e for each case. Assuming each sensor is weighted by noise level as in Eq. (4.23), Figure 4.1 provides a plot of the average computation time for each case, and Figure 4.2 displays the average ϕ_e error metric. The QUEST algorithm has an average computation time around 2×10^{-4} seconds among the eight cases, most likely due to the set tolerance and fixed iterative process. This consistent computation time is greater than both q-method and QUEST. The errors are similar among the three algorithms for each of the eight cases with the exception of Case 2. This is likely due to the iterative process of the FQS converging within the set tolerance. This is important to note as the FQS scheme is examining the norm of an error vector of matching coefficients, while QUEST is examining a residual norm between Newton-Raphson updates. Although greater than QUEST and q-method in Case 2, the FQS estimate is still below 10^{-2} degrees.
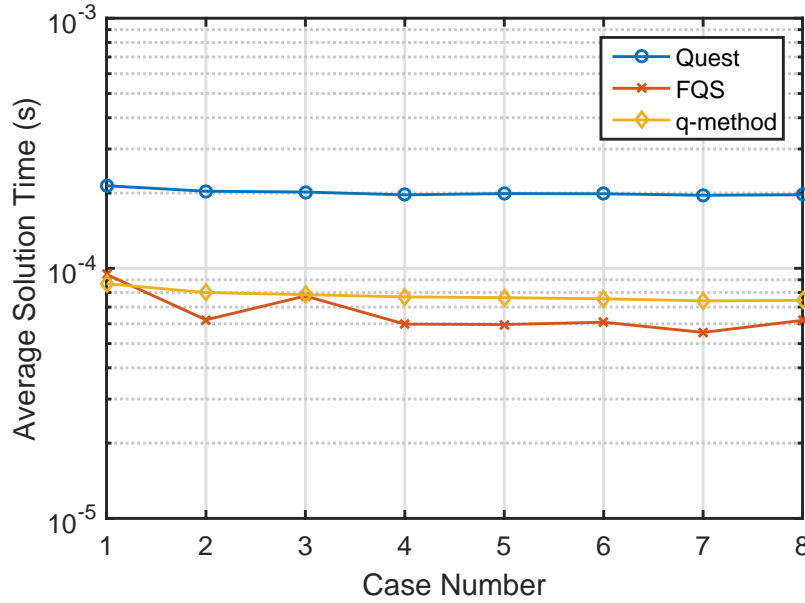
Figure 4.1: Attitude estimation results - average computation time over 10^5 realizations with sensor noise weighting.
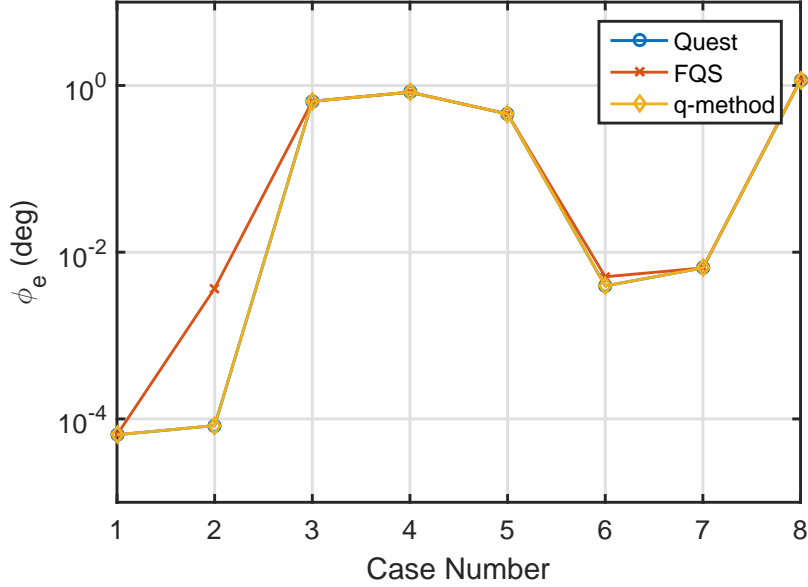
Figure 4.2: Attitude estimation results - principal angle error metric ϕ_e over 10^5 realizations with sensor noise weighting.

In Tables 4.2 and 4.3, the average solution time and estimation errors are tabulated for each case, respectively. The results indicate that for all eight test cases, the FQS algorithm performs between 56% and 72% (with an average of approximately 67%) faster than the QUEST method in terms of computational speed, and outperforms the q-method in all but Case 1. The vector measurements in Case 1 provide information about all three axes, are mutually orthogonal, and are associated with very low noise values. The performance of QUEST and the q-method in this case are not a surprise based on the well defined geometry of Case 1.

The FQS algorithm regains the computational advantage in the remaining seven cases, which are not as well geometrically defined and are associated with increased noise levels and representative off-axis and misaligned sensors. The average error metric for the eight cases is presented in Table 4.3. As a benchmark comparison, these error values are compared and found near identical to the results presented in [17; 44].

Within each case, the average error among the three different methods are nearly identical to one another. This error similarity is attributed to the same convergence tolerance used for comparison in each algorithm. This leads to the claim that for similar estimation error, the FQS method presents an average 67% improvement to QUEST computation time.

Table 4.2: Comparison of average computation time for the eight different single frame estimation cases. Percent differences are taken with respect to QUEST solution.

Case	Average Solution Time (s)		
	FQS	QUEST	q-method
1	9.455e-05 (-56%)	2.139e-04	8.673e-05 (-59%)
2	6.223e-05 (-69%)	2.034e-04	8.002e-05 (-61%)
3	7.751e-05 (-62%)	2.018e-04	7.847e-05 (-61%)
4	5.928e-05 (-70%)	1.967e-04	7.689e-05 (-61%)
5	5.959e-05 (-70%)	1.990e-04	7.629e-05 (-62%)
6	6.087e-05 (-69%)	1.986e-04	7.552e-05 (-62%)
7	5.542e-05 (-72%)	1.959e-04	7.410e-05 (-62%)
8	6.193e-05 (-69%)	1.969e-04	7.443e-05 (-62%)

Although Wahba's optimization problem led to the notion of constructing the **K** matrix and performing an eigendecomposition to minimize J, the value of the cost function is not evaluated in this section. This is a consequence of each method using the same **K** matrix to evaluate, and the similarities of the error angle ϕ_e values indicate the cost values will follow the same trends. The value of the cost function will be used as a metric when applying the PSO or GA method in Section 4.4.2.

Table 4.3: Comparison of average error ϕ_e for the eight different single frame estimation cases.

Case	Average Error ϕ_e (deg)		
	FQS	QUEST	q-method
1	6.458e-05	6.458e-05	6.458e-05
2	8.310e-05	3.683e-03	8.310e-05
3	6.464e-01	6.464e-01	6.464e-01
4	8.310e-01	8.310e-01	8.310e-01
5	4.551e-01	4.551e-01	4.551e-01
6	3.940e-03	5.074e-03	3.940e-03
7	6.475e-03	6.475e-03	6.475e-03
8	1.155e00	1.173e00	1.155e00

This section presented the new application of Strobach's FQS method to solving the single frame attitude estimation problem. By examining 8 cases of varying sensor refinement and noise levels, it was found the FQS is able to outperform the commonly used QUEST algorithm by nearly 67% in terms of computation speed while maintaining a similar order of accuracy. An additional benefit to using FQS is the simultaneous solution of all four roots to $\mathbf{K}$'s characteristic equation, and the usage of the $\max(\cdot)$ operation, rather than relying on an initial guess that converges to the maximum root in QUEST. The FQS method is elegant to code, and its simplicity and rapid solution time lends credence to real world space applications and attitude estimation.

4.4.2 Numerical Results Using PSO and GA.

The PSO and GA methods are applied to single frame vector observations in order to directly minimize Wahba's cost function in Eq. (4.1), restated as

$$J\left(\mathbf{R}^{bi}\right) = \frac{1}{2}\sum_{k=1}^{N} w_k \left|\left|\mathbf{v}_{kb} - \mathbf{R}^{bi}\mathbf{v}_{ki}\right|\right|^2. \tag{4.30}$$

The true attitude used in the heuristic optimization simulations is

$$\mathbf{q}^T = \begin{bmatrix} \frac{\sqrt{2}}{2} & 0 & 0 & \frac{\sqrt{2}}{2} \end{bmatrix}, \tag{4.31}$$

which corresponds to the rotation matrix

$$\mathbf{R} = \begin{bmatrix} 1 & 0 & 0 \\ 0 & 0 & 1 \\ 0 & -1 & 0 \end{bmatrix}. \tag{4.32}$$

For a given value of N, N inertial unit vectors are generated at random, and then rotated to the spacecraft body frame by the given rotation matrix with the addition of Gaussian noise at various noise levels. The PSO and GA algorithms are then applied to minimize Wahba's cost function directly and examined for efficacy.

The PSO results using a swarm of 10 particles are detailed in Figure 4.3. The average error angle trends approximately an order of magnitude greater than the calibrated sensor noise, and for noise values below $\sigma = 10^{-2}$, are less than 0.1 degrees. The average cost value is nearly independent of the number of observations, reaching similar costs that are below the specified tolerance. The average computation time has a surprisingly near-linear relation with observations. A linear fit to each of the six noise levels produces an average slope of approximately 0.16 seconds per observation, and an average y-intercept of 0.47 seconds. This implies an inherent half-second computation time, and for each additional observation, there is an additional 0.16 seconds for processing. Combined with average iteration values between 48 and 52,

the PSO algorithm itself likely represents the majority of the computation time, and the additional time per observation is attributed to the actual observation processing and cost function evaluation.

The GA results using a population of 10 members are detailed in Figure 4.4. For larger noise values, the average error is an order of magnitude greater than the same noise level result using PSO. The average value of the cost function is also greater, but well within acceptable orders of magnitude. This fact does point out that for the same data, GA and PSO are minimizing the same cost function with the same tolerance, and the random noise likely changes the location of the global optima. With 10 members of the population, the GA does take less time than PSO, but, the computation time is not as predictable as the previous PSO result.

For a comparison, the number of particles in the swarm were increased from 10 to 100. The results are shown in Figure 4.5. The trends are nearly identical, empirically, to the previous PSO results. The greater number of particles in the swarm allows the PSO to capture a slightly more accurate attitude estimate and lower cost, but the complexity and memory requirements of propagating 100 particles versus 10 do not necessarily merit the slight increase in accuracy. For an additional comparison, the population size of the GA was increased from 10 individuals to 100. The results are shown in Figure 4.6. The inclusion of more members in the population allows for greater diversity in the intermediate mutation and crossover portions of the heuristic algorithm. This allows the population to examine a greater search space, and allows for less sporadic error values and costs. However, the computation time has essentially doubled, but with an overall decrease in the number of generations or iterations. The increase in computation time is a direct result of the additional population members, and the diversity of the population allows for fewer generations to meet the convergence tolerance.
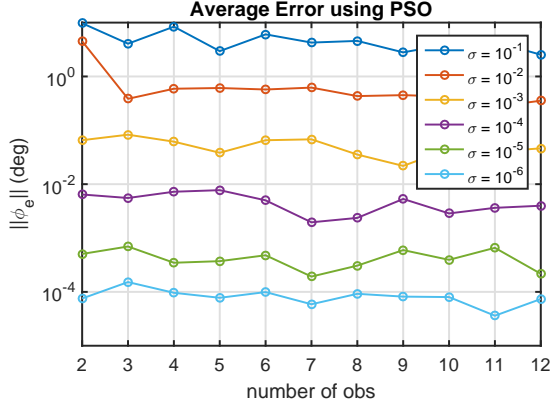
(a) Average PSO error ϕ_e
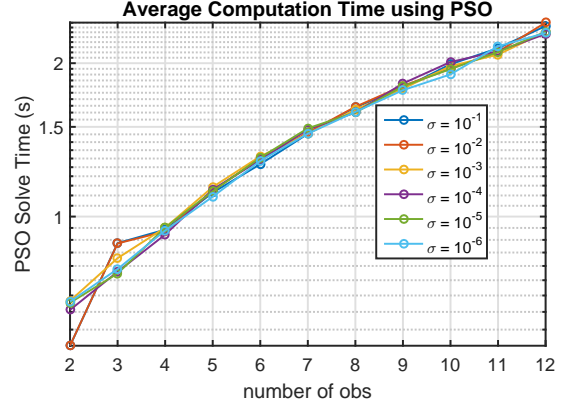
(b) Average PSO computation time
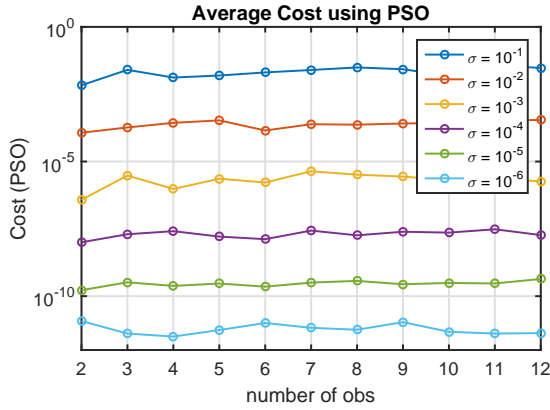
(c) Average Wahba cost function value
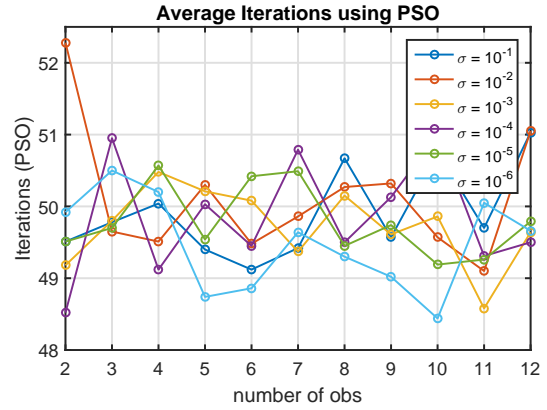
(d) Average number of iterations

Figure 4.3: Results from a direct minimization of Wahba's cost function using PSO (10 particles in swarm).

The computation time for both the PSO and GA methods benefits from the method by which the quaternion is calculated. The search space is limited to (q_1, q_2, q_3) and the fourth component is found by maintaining a unit norm constraint. Simulations were performed searching the entire (q_1, q_2, q_3, q_4) space where a penalty factor was introduced to the cost function for unit-norm violations. The computation time increased by at least an order of magnitude and the unit-norm constraint was
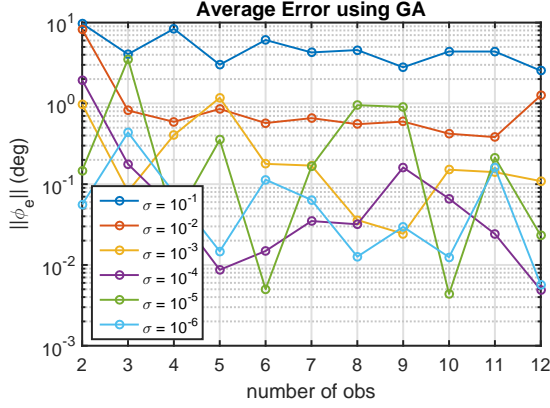
(a) Average GA error ϕ_e
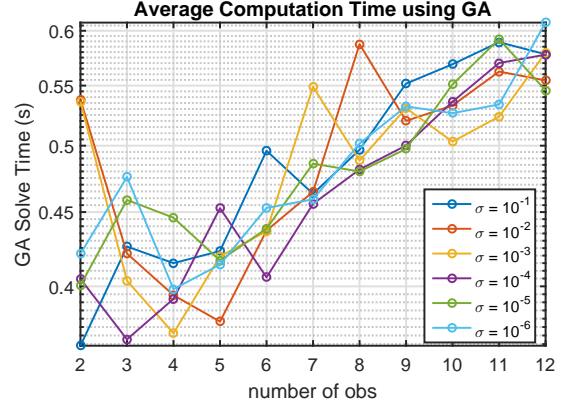
(b) Average GA computation time
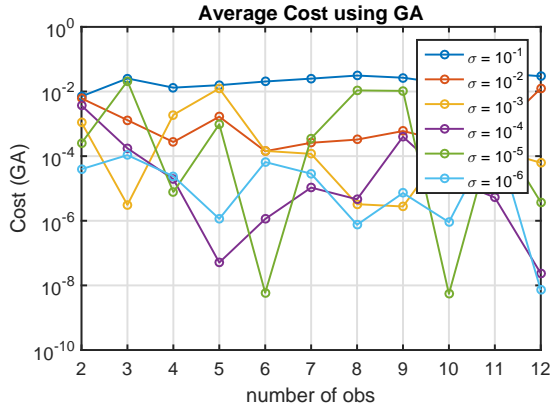
(c) Average Wahba cost function value
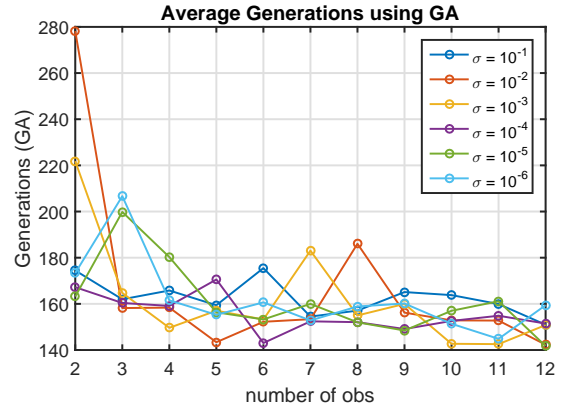
(d) Average number of iterations

Figure 4.4: Results from a direct minimization of Wahba's cost function using GA (10 population members).

often violated. Additionally, directly minimizing the cost function by iterating on the quaternion itself avoids the singularity at $\pm\pi$ encountered in classical methods that solve the eigenvalue problem and then calculate the quaternion through the Gibbs vector.
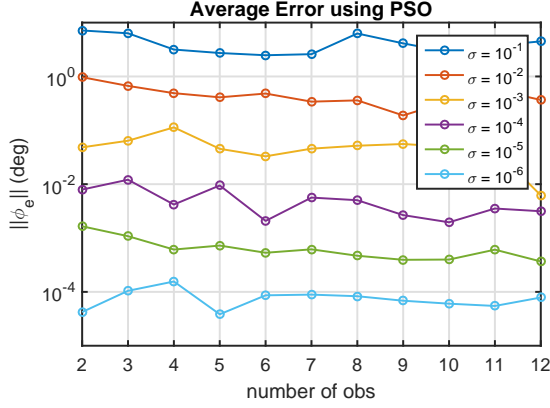
(a) Average PSO error ϕ_e
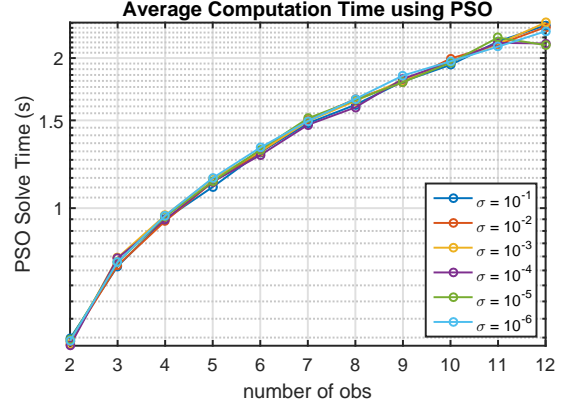
(b) Average PSO computation time
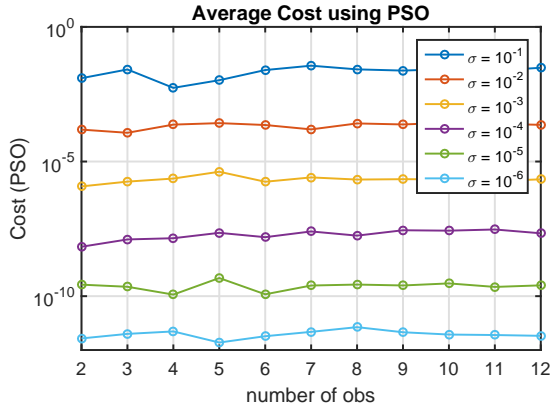
(c) Average Wahba cost function value
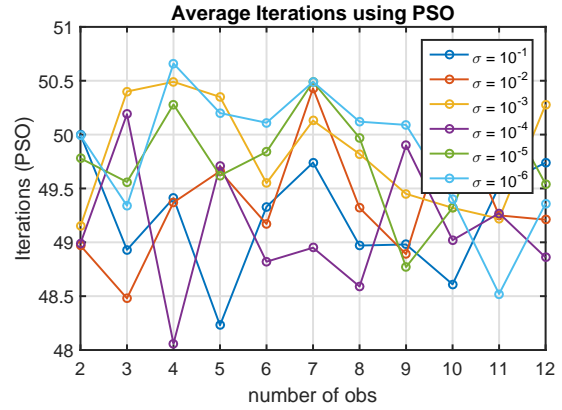
(d) Average number of iterations

Figure 4.5: Results from a direct minimization of Wahba's cost function using PSO (50 particles in swarm).

4.5   Conclusions and Future Work

This research proposed the application of Strobach's Fast Quartic Solver [18] to quickly solve the quartic eigenvalue problem required for the quaternion attitude estimate. The FQS algorithm decomposes the quartic characteristic equation of the **K** matrix into the product of two quadratics, and takes advantage of a well-defined Jacobian to equate polynomial coefficients via LU decomposition. This method

(a) Average GA error ϕ_e
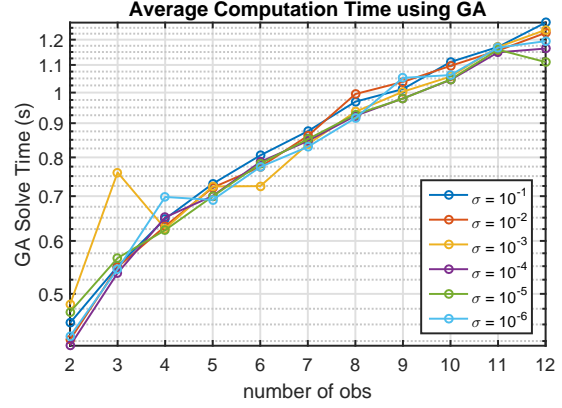
(b) Average GA computation time
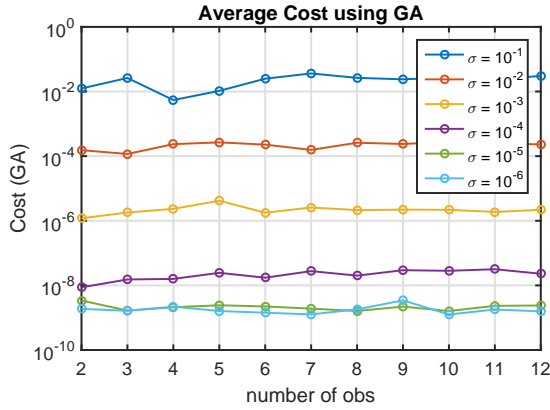
(c) Average Wahba cost function value
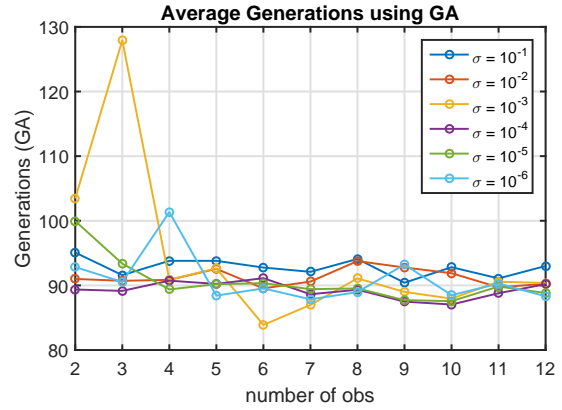
(d) Average number of iterations

Figure 4.6: Results from a direct minimization of Wahba's cost function using GA (100 population members).

produces an average of 67% improvement to the QUEST computation time, while using the same convergence criteria produces similar estimation error values. The decrease in computation time has the potential to reduce time lag between attitude estimate and control calculation. By solving simultaneously for all four eigenvalues, the method also avoids the possibility of converging on the *non* maximum eigenvalue. The FQS application is prone to the same singularities as QUEST and the *q*-method,

but these can be handled similarly by single frame rotations or other singularity avoidance or removal methods.

Additionally, this work examined the application of heuristic based techniques, to include particle swarm optimization (PSO) and genetic algorithms (GA), to solve Wahba's minimization problem to estimate spacecraft attitude. Both heuristic methods are capable of minimizing Wahba's cost function directly, but come with a significant increase in computation time compared to QUEST, q-method, and FQS. The algorithms also come with a computation complexity that may not be posed well for on-board implementation. One of the main benefits to estimating the quaternion via a heuristic method is a 'close enough' initial guess is not required, as heuristic techniques implement randomly chosen initial candidate solutions. Although these methods are not well posed for on-board processing, the heuristic algorithms are applicable to off-line post-processing of vector observation time history. Direct minimization of the cost function by searching the (q_1, q_2, q_3) maintains the unit norm constraint and avoids Gibbs vector singularities.

This research has focused on deterministic or geometric attitude determination based on various numerical solution schemes to the single frame estimation problem. A key contribution from this work resulted in the application of a rapid quartic root solver applied to the characteristic equation from Wahba's problem for a savings in computational cost. This research also allowed for the contribution of a new application of heuristic optimization to a total least-squares problem for attitude determination. Specific future work pertaining to this research will be detailed in Chapter 6.

V. Spacecraft Moment of Inertia Estimation Posed as an Ordinary Differential Equation Parameter Estimation Problem

The equations expressing the attitude dynamics of a rigid or flexible body are highly nonlinear, coupled, and sensitive to particular system parameters. This brief introductory section provides an abstract regarding the estimation of these system parameters. For a given set of initial conditions, the moment of inertia (MOI) for a spacecraft essentially determines the rotational trajectory. Accurate attitude determination is of concern to space situational awareness (SSA) operators, as miscalculation of the spacecraft's orientation directly influences the impact of modeled perturbations and can lead to poor translational state estimates. Moreover, current efforts into orbital debris removal necessitates the estimation of mass properties, which, through the methods developed in this research can be estimated by observing the body's angular velocity via some type of optical sensor. The classical rigid body motion problem is defined by determining the rotational trajectory and attitude of a body given its MOI and initial conditions. This research investigates the inverse problem of MOI estimation given mseasurements of the rotational trajectory and initial conditions which is solved in two manners. The first approach formulates the problem as a parameter estimation in a nonlinear ordinary differential equation under the presence of stochastic measurement noise. Relative MOI ratios are estimated with single-shooting methods employing Levenberg-Marquardt iteration schemes are employed. The second approach, in a new fashion, employs a cost function exploiting the classical polhodes of analytical mechanics and known constants of the motion, within a two-step optimization process utilizing heuristic optimization techniques as warm starts to SQP optimizers. Intermediate normalizations and use of Smelt

parameters are used to minimize the cost function to estimate actual principal MOI values rather than relative MOI ratios.

5.1 Introduction and Motivation

Accurate attitude determination is of concern to space situational awareness (SSA) operators. Miscalculations in the spacecraft's orientation can directly influence the impact of modeled perturbations that are functions of spacecraft attitude, such as atmospheric drag or solar radiation pressure. The accuracy of a position and velocity state estimate can become a function of how well the attitude of the spacecraft is estimated, which is directly a function of the MOI of the spacecraft. Further, efforts to remove tumbling debris require knowledge of the mass properties of the body for an effective capture.

The classical rigid body motion problem is determining the rotational trajectory of a body given a configuration (the MOI) and initial conditions. The classical rotational equations of motion are herein refered to as Euler's equations of rigid body motion, or simply Euler's equations. Euler's equations are nonlinear ordinary differential equations (ODEs) that are highly coupled among the states, and only have closed-form solutions for very particular scenarios, such as an isoinertial or axisymmetric body. Estimation of the MOI is a sensitive process, and on-orbit estimation techniques have been shown previously in [46; 66–68; 107; 108].

The intent of this research is to estimate a body's MOI by the measurement of angular rate data, whether by on-board gyro sensors, or by stand-off estimation of another body, as in the case of a tumbling satellite. More specifically, for torque-free motion, this research shows that the relative MOI ratios along each axis can be estimated. For torque-free motion with given initial conditions, these relative MOI ratios are shown to be the sole determinant of the rotational trajectory. However, an ambiguity exists when the absolute MOI about a specific axis is sought from a

solution solving the linear system formed by the relative MOI ratios as a consequence of being within the null space of a particular matrix.

One inherent problem in measuring the angular rates of a spacecraft or rigid body is measurement noise. To start, an initial assumption is made that the sensor has been calibrated and the measurement noise statistics are known. Further, we assume the measured angular rates are of the spacecraft body with respect to an inertial reference frame, allowing the employment of Euler's equations as classically derived.

Given the previous discussion, this research question then essentially seeks solution to the inverse problem of the classic Euler's equations. That is, given measurements of the rotational trajectory and initial conditions, *can one determine the moment of inertia*? The current problem is posed as one of parameter estimation in a nonlinear ordinary differential equation under the presence of stochastic measurement noise. Single-shooting methods employing Levenberg-Marquardt iteration schemes are employed along with maximum likelihood estimates (MLE) techniques. An additional intent of this research is to use heuristic optimization schemes as a warm start initial guess to an SQP optimization method. The heuristic PSO algorithm is also used to minimize a novel cost function constraining the rotational trajectory along the intersection of angular momentum and kinetic energy ellipsoids. Various structural configurations and rotational trajectories are investigated to assess the performance of the established estimation algorithms.

5.2 Background

The current research on MOI estimation examines the fields of spacecraft attitude dynamics, Smelt parameters, polhodes, parameter estimation, shooting techniques, MOI estimation, and heuristic optimization. For background information, the reader is referred to Section 2.1 regarding attitude dynamics, Section 2.5 for MOI estimation,

and Section 2.6 for heuristic optimization. The following sections provide background on Smelt parameters, polhodes, parameter estimation, and shooting techniques.

5.2.1 Relative MOI Ratios or Smelt Parameters.

Euler's rotation equations of motion in the principal frame are

$$\dot{\omega}_1 = \left(\frac{B-C}{A}\right)\omega_2\omega_3$$

$$\dot{\omega}_2 = \left(\frac{C-A}{B}\right)\omega_3\omega_1. \tag{5.1}$$

$$\dot{\omega}_3 = \left(\frac{A-B}{C}\right)\omega_1\omega_2$$

The coefficients in Eq. (5.1), along with initial conditions on angular velocity, determine the rotational trajectory of a rigid body. For example, an unperturbed axisymmetric body will rotate about one axis at a constant angular velocity, and rotate about the other two axes with a constant frequency. These coefficients will remain constant for a rigid body, such that the coefficients can be labeled as the following

$$\mathbf{k} = \begin{bmatrix} k_1 & k_2 & k_3 \end{bmatrix}^T = \begin{bmatrix} \frac{I_2-I_3}{I_1} & \frac{I_3-I_1}{I_2} & \frac{I_1-I_2}{I_3} \end{bmatrix}^T \tag{5.2}$$

and Euler's equations in principal form can be expressed as

$$\dot{\omega}_1 = k_1\omega_2\omega_3$$

$$\dot{\omega}_2 = k_2\omega_3\omega_1. \tag{5.3}$$

$$\dot{\omega}_3 = k_3\omega_1\omega_2$$

The values (k_1, k_2, k_3) are relative MOI ratios among the three axes, and are also refered to as Smelt parameters [22]. The values for (k_1, k_2, k_3) are constrained within $[-1, 1]$, and indicate the level of symmetry. Values near 0 or close in magnitude to 1 indicate symmetry between two axes, while intermediate values indicate levels of asymmetry. The Smelt parameters are not necessarily independent of one another; rather, they are constrained by the relation [109]

$$k_1 + k_2 + k_3 + k_1k_2k_3 = 0, \tag{5.4}$$

114

and given two of the three parameters, the other is immediately known. For example, given k_1 and k_3, k_2 can be found as

$$k_2 = -\frac{k_1 + k_3}{1 + k_1 k_3}. \tag{5.5}$$

The constraint in Eq. (5.4) follows a petal-shape in the (k_1, k_2, k_3) space [109], seen in Figure 5.1. By observing Eqs.(5.2) and (5.3), given a spacecraft whose MOI $\mathbf{I}_1$ is
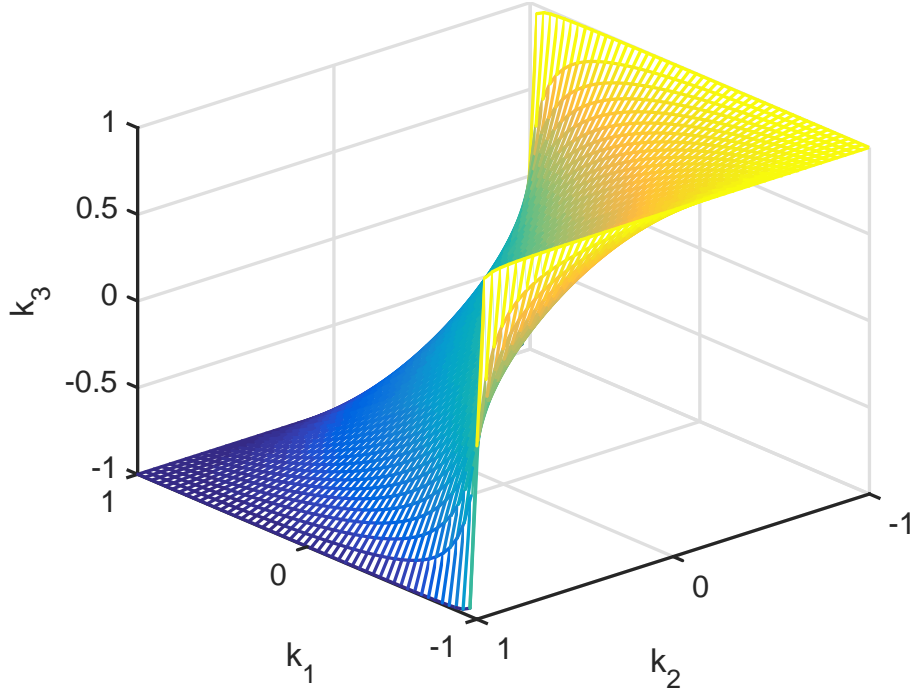
Figure 5.1: Petal shape formed by the Smelt parameter (k_1, k_2, k_3) plane.

$$\mathbf{I}_1 = \begin{bmatrix} I_1 & 0 & 0 \\ 0 & I_2 & 0 \\ 0 & 0 & I_3 \end{bmatrix}, \tag{5.6}$$

and another spacecraft whose MOI is $\mathbf{I}_2$ is

$$\mathbf{I}_2 = \beta \mathbf{I}_1 \tag{5.7}$$

where β is some constant, the relative MOI ratios will be identical and the rotational trajectory will be equal for the same initial conditions in a torque-free environment. This can be observed by calculating the Smelt parameters for each MOI as

$$\mathbf{k}_1 = \begin{bmatrix} \frac{I_2-I_3}{I_1} & \frac{I_3-I_1}{I_2} & \frac{I_1-I_2}{I_3} \end{bmatrix}^T$$

$$\mathbf{k}_2 = \begin{bmatrix} \frac{\beta}{\beta}\frac{I_2-I_3}{I_1} & \frac{\beta}{\beta}\frac{I_3-I_1}{I_2} & \frac{\beta}{\beta}\frac{I_1-I_2}{I_3} \end{bmatrix}^T = \mathbf{k}_1$$

(5.8)

Given a set of relative MOI ratios or Smelt parameters, a linear system of equations can be formed to solve for the absolute MOI values, shown by rearranging Eq. (5.2) as

$$I_1 k_1 - I_2 + I_3 = 0$$

$$I_2 k_2 - I_3 + I_1 = 0\cdot$$

(5.9)

$$I_3 k_3 - I_1 + I_2 = 0$$

Equation (5.9) can now be placed into the form $\mathbf{Rx} = \mathbf{0}$ as

$$\begin{bmatrix} k_1 & -1 & 1 \\ 1 & k_2 & -1 \\ -1 & 1 & k_3 \end{bmatrix} \begin{bmatrix} I_1 \\ I_2 \\ I_3 \end{bmatrix} = \begin{bmatrix} 0 \\ 0 \\ 0 \end{bmatrix}.$$

(5.10)

Since the matrix in the system of Eq. (5.10) linearly transforms the principal MOI to the zero vector, the principal MOI essentially lies along the basis of the null space of the relative MOI matrix, $\mathcal{N}(\mathbf{R})$. The null space of the matrix in Eq. (5.10) is found as

$$\mathbf{p} = \begin{bmatrix} I_1 \\ I_2 \\ I_3 \end{bmatrix} = \beta \begin{bmatrix} \frac{1+k_3}{1-k_1} \\ \frac{1+k_1 k_3}{1-k_1} \\ 1 \end{bmatrix},$$

(5.11)

where k_2 has been expressed as a function of k_1 and k_3 and β is a scaling constant. By observation, this β parameter is essentially the minor MOI. Multiplication of the principal MOI by the constant β will also remain in $\mathcal{N}(\mathbf{R})$. The implication of this null

116

space finding to the current estimation problem is that once a **k** has been determined, there will be an ambiguity where the absolute MOI lies along the null space basis. A possible mechanism to avoid this problem is then to incorporate torques in the system model (such that $\mathbf{M} \neq \mathbf{0}$) and exploit the coupling; however, the MOI ratios and the angular velocity initial conditions are no longer the sole determination of the rotational trajectory. This research demonstrates the constant β can be determined by exploiting the angular momentum and kinetic energy ellipsoids, which are discussed in the next section.

5.2.2 Poinsot's Ellipsoids for Torque Free Rigid Body Motion.

For torque-free rigid body motion, angular momentum in the inertial frame is a conserved quantity. Component-wise, this does not hold true in the body frame. However, as there is a simple rotation between the inertial and body frame, the magnitude of the angular momentum vector will be equal in both frames. The angular momentum **H** is expressed as the product of the MOI and the angular velocity as

$$\mathbf{H} = \mathbf{I}\boldsymbol{\omega}. \tag{5.12}$$

Assuming the body frame is aligned with the principal axes such that the MOI matrix is diagonalizable, the above expression in matrix-vector form is

$$\begin{bmatrix} H_1 \\ H_2 \\ H_3 \end{bmatrix} = \begin{bmatrix} I_1 & 0 & 0 \\ 0 & I_2 & 0 \\ 0 & 0 & I_3 \end{bmatrix} \begin{bmatrix} \omega_1 \\ \omega_2 \\ \omega_3 \end{bmatrix}. \tag{5.13}$$

Component wise, the angular momentum is then expressed as

$$\begin{bmatrix} H_1 \\ H_2 \\ H_3 \end{bmatrix} = \begin{bmatrix} I_1\omega_1 \\ I_2\omega_2 \\ I_3\omega_3 \end{bmatrix}. \tag{5.14}$$

117

Taking the norm of the above equation, the magnitude of the angular momentum vector is given as

$$||\mathbf{H}||^2 = H^2 = I_1^2\omega_1^2 + I_2^2\omega_2^2 + I_3^2\omega_3^2. \tag{5.15}$$

Normalizing the above equation by H^2, a general form of an ellipsoid appears as

$$1 = \frac{\omega_1^2}{H^2/I_1^2} + \frac{\omega_2^2}{H^2/I_2^2} + \frac{\omega_3^2}{H^2/I_3^2}. \tag{5.16}$$

An analogous development occurs for the kinetic energy ellipsoid. In the absence of energy dissipation external torques, the rotational kinetic energy T will remain constant. The kinetic energy is determined as the dot product of the angular momentum and angular velocity, expressed as

$$2T = \mathbf{I}\boldsymbol{\omega} \cdot \boldsymbol{\omega}. \tag{5.17}$$

Expanding the kinetic energy component wise,

$$2T = I_1\omega_1^2 + I_2\omega_2^2 + I_3\omega_3^2, \tag{5.18}$$

and dividing through by $2T$, the kinetic energy ellipsoid takes the form

$$1 = \frac{\omega_1^2}{2T/I_1} + \frac{\omega_2^2}{2T/I_2} + \frac{\omega_3^2}{2T/I_3}. \tag{5.19}$$

The angular velocity must lie on the surface of both of the ellipsoids, and the intersection of the angular momentum and kinetic energy ellipsoid is then the rotational trajectory of the rigid body assuming torque-free motion. Classical results and relations regarding this can be found in Hughes [7]. This intersection is often termed a polhode. Figure 5.2 provides an example of the intersection of the two ellipsoids and the path traced by the angular velocity. Section 5.3.2 will recast these polhodes in terms of the Smelt parameters as a means to estimate the MOI.
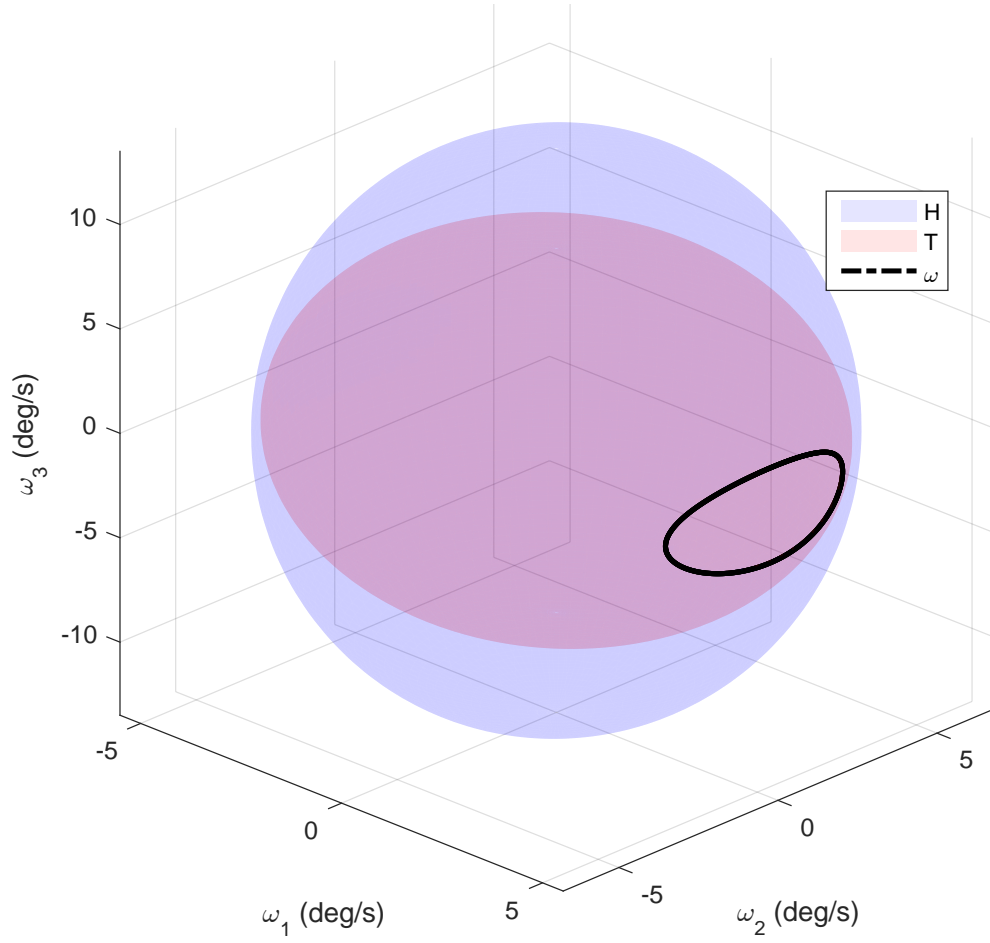
Figure 5.2: Polhode example - Intersection of angular momentum ellipsoid ($H = 4.712 \text{ N} \cdot \text{m} \cdot \text{s}$) and kinetic energy ellipsoid ($T = 0.2315 \text{ N} \cdot \text{m}$) for rigid body with principal MOI given as $I_1 = 50 \text{ kg-m}^2, I_2 = 40 \text{ kg-m}^2, I_3 = 20 \text{ kg-m}^2$.

5.2.3 *Parameter Estimation in Ordinary Differential Equations.*

Ordinary differential equations can be used to model and predict the evolution of a system based on a given set of initial or boundary conditions. System dynamics are typically functions of key system parameters, such as the current problem of MOI coupling in rotational motion. Often these parameters are physically measurable or observable as an additional state, but may require a more complex estimation process. This section will briefly detail some of the open literature regarding parameter estimation in ODEs.

Dogruer discretized the dynamics of a robot odometer in [110] and implemented a MMAE composed of EKFs to estimate physical robot parameters. Parameter estimation can also be performed using recursive filtering. In [39], Vandyke et al. implemented a dual UKF in order to solve for a spacecraft's MOI. Vandyke estimated the full MOI matrix to include the products of inertia, producing an additional six states to estimate.

West and Swiler approximate various physical systems by fitting the data with multiple Gaussian processess, and use a maximum likelihood estimator to fit parameters in the Gaussian processes [111]. David and Bastin also implement a maximum likelihood parameter estimator to determine flow correction properties for a two-tank water system [112]. Donnet and Samson proposed a parameter estimation algorithm using expectation-maximization to describe biological processes [113].

Hamilton implements single- and multiple-shooting methods to estimate system parameters in nonlinear ODEs [114]. Hamilton also compares Gauss-Newton and Levenberg-Marquardt numerical iterations within the single-shooting, and finds Levenberg-Marquardt tends to converge more often in nonlinear chaotic systems [114]. Shawash also used the Levengerg-Marquardt method for real-time parameter estimation on field programmable gate arrays [115]. Ramsay et al. modified data

smoothing methods to estimate parameters within chemical processes and auto immune disease modeling [116].

5.2.4 Numerical Shooting and Iterative Techniques.

Numerical shooting techniques emanate from the idea of selecting a design variable node and propagating, or shooting, the trajectory forward, and minimizing the residuals between a given and generated trajectory. Figure 5.3 provides a visualization of the single shooting process.
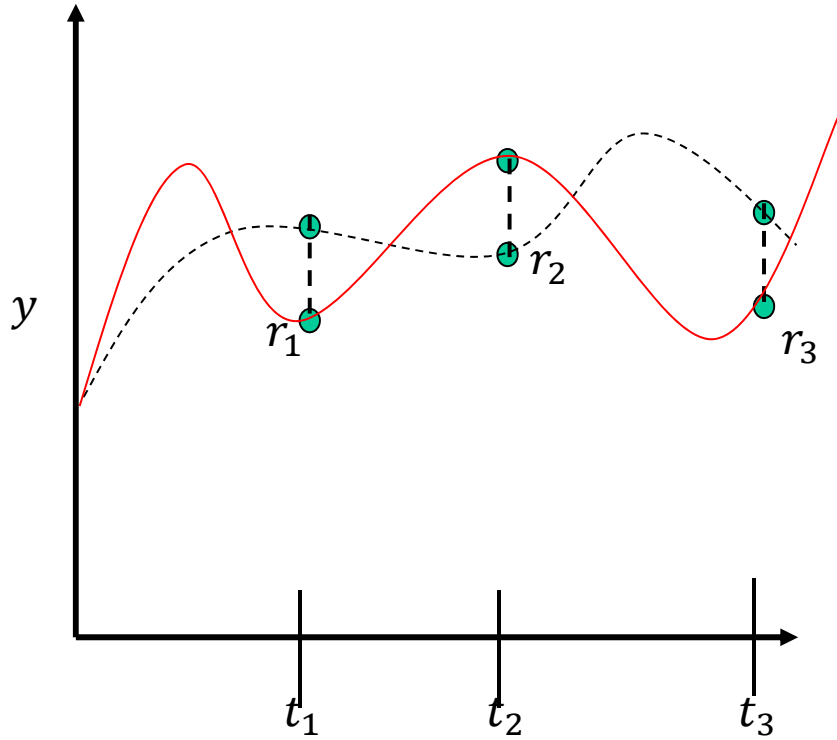
Figure 5.3: Example of a single-shooting algorithm where some design variable is iterated on to minimize the residuals r_i at time t_i between the trajectory y and the generated trajectory (dashed-line).

At a top level, the method requires a trajectory, a governing system, either known or unknown initial conditions, and the selection of design variables. Based on the given conditions, the change in the system dynamics with respect to the design variables must then be developed, typically through a Jacobian. A convergence tolerance, a type of residual metric, and further, a type of iteration scheme must be chosen. A standard Gauss-Newton scheme is typically represented as

$$\mathbf{p}_{j+1} = \mathbf{p}_j - \mathbf{A}^{-1}\mathbf{r}, \tag{5.20}$$

where $\mathbf{p}$ is a design vector, $\mathbf{A}$ is a Jacobian, and $\mathbf{r}$ is a residual. The standard Gauss-Newton in Eq. (5.20) assumes the Jacobian is square. For non-square examples, a pseudo-inverse is typically given in the form

$$\mathbf{p}_{j+1} = \mathbf{p}_j - \left(\mathbf{A}^T\mathbf{A}\right)^{-1}\mathbf{A}^T\mathbf{r}. \tag{5.21}$$

Equation (5.21) simplifies to Eq. (5.20) when a square assumption is made. However, for systems that are ill-conditioned, nonlinear, or very large $\mathbf{A}$ matrices, the pseudo-inverse calculations perform poorly. One potential method to circumvent the ill-conditioning is to use the Lavenberg-Marquardt method [114], given as

$$\mathbf{p}_{j+1} = \mathbf{p}_j - \left(\mathbf{A}^T\mathbf{A} + \lambda \cdot \operatorname{diag}\left(\mathbf{A}^T\mathbf{A}\right)\right)^{-1}\mathbf{A}^T\mathbf{r} \tag{5.22}$$

where λ is an adaptable damping parameter, and the diag($\cdot$) operator indicates the formation of a diagonal matrix of the diagonals of the matrix product $\mathbf{A}^T\mathbf{A}$.

5.3 Methodology

This section will provide an overview of the methodology and algorithms used to estimate the relative MOI ratios or the actual principal MOI values from measured angular velocity data. Section 5.3.1 will describe the numerical shooting methodology, while Section 5.3.2 will overview the heuristic polhode optimization method.

5.3.1 Numerical Single Shooting Solutions.

A time-series of angular velocity data will be generated using Euler's equations. Next, zero-mean Gaussian white noise at a given σ noise level will be added to the angular velocity data to simulate measurements. Having measured data, a numerical single shooting will be employed using the relative MOI ratio as a design variable. This experiment will then specifically focus on estimating the principal MOI values. A Jacobian must be constructed mapping changes in system dynamics to the relative MOI ratios. The Jacobian for the torque-free rigid body system, $\mathbf{J_{M=0}}$, is given as

$$
\mathbf{J_{M=0}} = \frac{\partial \mathbf{f}}{\partial \mathbf{p}} = \begin{bmatrix} \frac{\partial f_1}{p_1} & \frac{\partial f_1}{p_2} & \frac{\partial f_1}{p_3} \\ \frac{\partial f_2}{p_1} & \frac{\partial f_2}{p_2} & \frac{\partial f_2}{p_3} \\ \frac{\partial f_3}{p_1} & \frac{\partial f_3}{p_2} & \frac{\partial f_3}{p_3} \end{bmatrix}
$$
$$
= \begin{bmatrix} \frac{\partial \dot{\omega}_1}{p_1} & \frac{\partial \dot{\omega}_1}{p_2} & \frac{\partial \dot{\omega}_1}{p_3} \\ \frac{\partial \dot{\omega}_2}{p_1} & \frac{\partial \dot{\omega}_2}{p_2} & \frac{\partial \dot{\omega}_2}{p_3} \\ \frac{\partial \dot{\omega}_3}{p_1} & \frac{\partial \dot{\omega}_3}{p_2} & \frac{\partial \dot{\omega}_3}{p_3} \end{bmatrix}. \tag{5.23}
$$

Reexamining Euler's equations, if the parameter vector of interest is the relative MOI ratio, the Jacobian for torque-free rigid body motion is then

$$
\mathbf{J_{M=0}} = \begin{bmatrix} \frac{\partial \dot{\omega}_1}{k_1} & \frac{\partial \dot{\omega}_1}{k_2} & \frac{\partial \dot{\omega}_1}{k_3} \\ \frac{\partial \dot{\omega}_2}{k_1} & \frac{\partial \dot{\omega}_2}{k_2} & \frac{\partial \dot{\omega}_2}{k_3} \\ \frac{\partial \dot{\omega}_3}{k_1} & \frac{\partial \dot{\omega}_3}{k_2} & \frac{\partial \dot{\omega}_3}{k_3} \end{bmatrix} = \begin{bmatrix} \omega_2\omega_3 & 0 & 0 \\ 0 & \omega_1\omega_3 & 0 \\ 0 & 0 & \omega_1\omega_2 \end{bmatrix}, \tag{5.24}
$$

which is a much simpler, elegant form with a computationally less expensive inverse.

The $\mathbf{A}$ matrix will now be formed from the Jacobian evaluated at each time step. Let the time interval be divided into N time-steps ranging from t_0 to t_n. The

A matrix used in the shooting scheme is then constructed by

$$\mathbf{A} = \begin{bmatrix} \mathbf{J_{M=0}}(t_0) \\ \mathbf{J_{M=0}}(t_1) \\ \vdots \\ \mathbf{J_{M=0}}(t_N) \end{bmatrix}, \tag{5.25}$$

and forms a $(3N \times 3)$ matrix. The non-square nature of the **A** matrix merits the use of the Lavenberg-Marquardt method to numerically iterate on the **p** design vector.

An initial guess will be randomly generated for the **p** vector on the interval $[-1, 1]^3$. The trajectory will be propagated to form the time series $\boldsymbol{\omega_p}$, and the Jacobian evaluated at each time step and the **A** matrix formed. The residual vector will then be calculated as

$$\mathbf{r} = \begin{bmatrix} \tilde{\boldsymbol{\omega}}(t_0) - \boldsymbol{\omega_p}(t_0) \\ \tilde{\boldsymbol{\omega}}(t_1) - \boldsymbol{\omega_p}(t_1) \\ \vdots \\ \tilde{\boldsymbol{\omega}}(t_N) - \boldsymbol{\omega_p}(t_N) \end{bmatrix}, \tag{5.26}$$

where $\tilde{\boldsymbol{\omega}}$ is the measured angular velocity, given by

$$\tilde{\boldsymbol{\omega}} = \boldsymbol{\omega} + \boldsymbol{\eta}_\omega, \tag{5.27}$$

where $\boldsymbol{\eta}_\omega$ is a 3×1 vector of zero-mean Gaussian noise with variance σ^2. If the 2-norm of the residual vector is below a set tolerance, the design vector becomes the relative MOI estimate. If the residual is greater than the tolerance, the design vector is updated using the LM relation

$$\mathbf{p}_{j+1} = \mathbf{p}_j - \left(\mathbf{A}^T \mathbf{A} + \lambda \cdot \text{diag} \left(\mathbf{A}^T \mathbf{A} \right) \right)^{-1} \mathbf{A}^T \mathbf{r}. \tag{5.28}$$

For each experiment, 100 simulations will be conducted and an average error reported for various noise levels. The error metric will be taken as

$$e_{\mathbf{p}} = ||\tilde{\mathbf{p}} - \mathbf{p}||. \tag{5.29}$$

124

In an attempt to estimate the actual principal MOI values, the inclusion of external moments is examined. The same procedure as previously described is implemented, with three exceptions. The first is the dynamics are propagated assuming $\mathbf{M} \neq \mathbf{0}$ in Euler's rotational EOMs. The second exception is the Jacobian for the rigid body system $\mathbf{J_M}$ must be recalculated. Restating the EOMs for rigid body motion as

$$
\begin{aligned}
\dot{\omega}_1 &= \frac{M_1}{I_1} + \frac{I_2 - I_3}{I_1}\omega_2\omega_3 \\
\dot{\omega}_2 &= \frac{M_2}{I_2} + \frac{I_3 - I_1}{I_2}\omega_3\omega_1. \\
\dot{\omega}_3 &= \frac{M_3}{I_3} + \frac{I_1 - I_2}{I_3}\omega_1\omega_2
\end{aligned}
\tag{5.30}
$$

The Jacobian is then taken as the partial with respect to the principal MOI values.

$$
\begin{aligned}
\mathbf{J_M} = \frac{\partial \mathbf{f}}{\partial \mathbf{p}} &=
\begin{bmatrix}
\frac{\partial f_1}{I_1} & \frac{\partial f_1}{I_2} & \frac{\partial f_1}{I_3} \\
\frac{\partial f_2}{I_1} & \frac{\partial f_2}{I_2} & \frac{\partial f_2}{I_3} \\
\frac{\partial f_3}{I_1} & \frac{\partial f_3}{I_2} & \frac{\partial f_3}{I_3}
\end{bmatrix} \\
&=
\begin{bmatrix}
\frac{\partial \dot{\omega}_1}{I_1} & \frac{\partial \dot{\omega}_1}{I_2} & \frac{\partial \dot{\omega}_1}{I_3} \\
\frac{\partial \dot{\omega}_2}{I_1} & \frac{\partial \dot{\omega}_2}{I_2} & \frac{\partial \dot{\omega}_2}{I_3} \\
\frac{\partial \dot{\omega}_3}{I_1} & \frac{\partial \dot{\omega}_3}{I_2} & \frac{\partial \dot{\omega}_3}{I_3}
\end{bmatrix}.
\end{aligned}
\tag{5.31}
$$

Taking the partials in Eq. (5.32) for the included torque system, the Jacobian is explicitly found as

$$
\mathbf{J_M} =
\begin{bmatrix}
\frac{I_3 - I_2}{I_1^2}\omega_2\omega_3 - \frac{M_1}{I_1^2} & \frac{1}{I_1}\omega_2\omega_3 & -\frac{1}{I_1}\omega_2\omega_3 \\
-\frac{1}{I_2}\omega_1\omega_3 & \frac{I_1 - I_3}{I_2^2}\omega_1\omega_3 - \frac{M_2}{I_2^2} & \frac{1}{I_2}\omega_1\omega_3 \\
\frac{1}{I_3}\omega_1\omega_2 & -\frac{1}{I_3}\omega_1\omega_2 & \frac{I_2 - I_1}{I_3^2}\omega_2\omega_1 - \frac{M_3}{I_3^2}
\end{bmatrix}.
\tag{5.32}
$$

The third exception is the initial guess must be closer to the basin of attraction of the solver. This is a limiting factor as the search space will significantly increase to account for a range of MOI, but the second-order dependency on the principal MOI in the moment terms introduces additional coupling and sensitivity. The methodology

125

for estimating relative MOI ratios by single shooting is summarized in Algorithm 3.

Algorithm 3: Relative MOI Estimation by Single Shooting and LM Iteration

     Given a time history of measured angular rate data $\boldsymbol{\omega}(t)$ and convergence tolerance ϵ

1 Define a LM factor λ and adaption rate τ

2 Randomly generate an initial guess $\mathbf{p}_0$ in the cube $[-1, 1]^3$

3 While $||\mathbf{r}|| > \epsilon$

     Increase iteration step

     Assign guess variable as previous update $\mathbf{p}_j = \mathbf{p}_{j-1}$

     Numerically propagate equations of motion $\dot{\boldsymbol{\omega}}$ using $\mathbf{p}_j$

     Construct residual vector $\mathbf{r}_j$ using Eq. (5.26)

     If $\mathbf{r}_j < \mathbf{r}_{j-1}$, then $\lambda = \lambda/\tau$; elseif $\mathbf{r}_j > \mathbf{r}_{j-1}$, then $\lambda = \lambda \cdot \tau$

     Construct the $3 \cdot N \times 3$ matrix $\mathbf{A}$ from Eq. (5.25), update $\mathbf{p}_j$ using Eq. (5.28)

4 Define the relative MOI estimate $\tilde{\mathbf{p}}$ as the updated guess value $\mathbf{p}_j$

5.3.2 *Polhode Exploitation.*

This method seeks to exploit classical constants of the motion of Euler's equations and to take advantage of the shape of the polhode discussed in Section 5.2.2, while also using the Smelt parameters to limit an optimization search space. First, for torque-free rigid body motion, it is known that angular momentum and rotational kinetic energy are constants of the motion. The two constants are functions of the angular velocity and the body's MOI. Second, it has been established that a body's principal MOI can be expressed in terms of the Smelt parameters, but there will be an arbitrary constant as the principal MOI lies along the basis of a null space. The angular momentum can be recast in terms of the Smelt parameters as

$$H^2 = I_1^2\omega_1^2 + I_2^2\omega_2^2 + I_3^2\omega_3^2 = \left(\beta\frac{1+k_3}{1-k_1}\right)^2\omega_1^2 + \left(\beta\frac{1+k_3k_1}{1-k_1}\right)^2\omega_2^2 + \beta^2\omega_3^2. \quad (5.33)$$

Remembering that the constant β scales the null space of the relative MOI matrix, certain manipulations can be made to essentially normalize the design variables. Dividing Eq. (5.33) through by β^2, and defining the quantity η as

$$\eta \equiv \frac{H^2}{\beta^2}, \tag{5.34}$$

the angular momentum relation can be recast as the following

$$\eta = c_1^2 \omega_1^2 + c_2^2 \omega_2^2 + c_3^2 \omega_3^2, \tag{5.35}$$

where the coefficients are defined as

$$c_1 \equiv \frac{1 + k_3}{1 - k_1}$$
$$c_2 \equiv \frac{1 + k_3 k_1}{1 - k_1} \tag{5.36}$$
$$c_3 \equiv 1.$$

A similar manipulation can be performed on the rotational kinetic energy relationship. Defining τ as

$$\tau \equiv \frac{2T}{\beta}, \tag{5.37}$$

the new expression for rotational kinetic energy is given as

$$\tau = c_1 \omega_1^2 + c_2 \omega_2^2 + c_3 \omega_3^2. \tag{5.38}$$

Since angular momentum and kinetic energy are constants of the motion, their time derivatives must be zero. As the left hand side of Eqs. (5.35) and (5.38) have only been manipulated by constants, their time derivatives must be zero as well. This produces the following two constraints

$$0 = c_1^2 \omega_1 \dot{\omega}_1 + c_2^2 \omega_2 \dot{\omega}_2 + c_3^2 \omega_3 \dot{\omega}_3$$
$$0 = c_1 \omega_1 \dot{\omega}_1 + c_2 \omega_2 \dot{\omega}_2 + c_3 \omega_3 \dot{\omega}_3 \tag{5.39}$$

where the expressions for $\dot{\omega}_1, \dot{\omega}_2$, and $\dot{\omega}_3$ are given by Eq. (5.1) or Eq. (5.3).

Having recast the angular momentum and kinetic energy ellipsoids in terms of the Smelt parameters and a scaling constant β, these expressions can now be exploited in a two-step optimization scheme. The first optimization problem is to minimize a cost function forcing the fit of the $\tilde{\boldsymbol{\omega}}$ data to an angular momentum ellipsoid, a kinetic energy ellipsoid, while also minimizing the time derivatives of angular momentum and kinetic energy. The ellipsoids will be used in Smelt parameter form to shrink the design variable search space. Mathematically, the first optimization problem is expressed as

$$\underset{\mathbf{u_1}}{\text{minimize}} \quad J_1 = \sum_{i=1}^{N} \left(J_H^2(t_i) + J_T^2(t_i) + J_{\dot{H}}^2(t_i) + J_{\dot{T}}^2(t_i) \right) \quad ,$$

where the individual costs are given by

$$
\begin{aligned}
J_H(t_i) &= \left|\left| \eta - \left[c_1^2 \omega_1^2(t_i) + c_2^2 \omega_2^2(t_i) + c_3^2 \omega_3^2(t_i) \right] \right|\right| \\
J_T(t_i) &= \left|\left| \tau - \left[c_1 \omega_1^2(t_i) + c_2 \omega_2^2(t_i) + c_3 \omega_3^2(t_i) \right] \right|\right| \\
J_{\dot{H}}(t_i) &= c_1^2 \omega_1(t_i)\dot{\omega}_1(t_i) + c_2^2 \omega_2(t_i)\dot{\omega}_2(t_i) + c_3^2 \omega_3(t_i)\dot{\omega}_3(t_i) \\
J_{\dot{T}}(t_i) &= c_1 \omega_1(t_i)\dot{\omega}_1(t_i) + c_2 \omega_2(t_i)\dot{\omega}_2(t_i) + c_3 \omega_3(t_i)\dot{\omega}_3(t_i).
\end{aligned}
\tag{5.40}
$$

The control vector $\mathbf{u}_1$ is given by

$$\mathbf{u}_1 = \begin{bmatrix} k_1 & k_3 & \eta & \tau \end{bmatrix}^T. \tag{5.41}$$

The Smelt parameters k_1 and k_3 are limited between $[-1, 1]$, and the third parameter k_2 is derived from the other two values. As given in Eq.(5.34) and Eq.(5.37), respectively, the normalized angular momentum η and kinetic energy τ are positive values, whose lower and upper bound magnitudes can be approximated by the measured angular velocity data. The coefficients (c_1, c_2, c_3) have previously been defined, but represent a point along the basis of the null space of the relative MOI

matrix, given as

$$c_1 = \frac{1 + k_3}{1 - k_1}$$

$$c_2 = \frac{1 + k_3 k_1}{1 - k_1}.$$

(5.42)

$$c_3 = 1$$

Assuming the first optimization is successful, the second optimization problem is to minimize a cost function again forcing the fit of the kinetic energy and angular momentum ellipsoids, but this time as functions of the principal MOI, expressed in terms of the optimal Smelt parameters. The second optimization problem also seeks to size the two ellipsoids by solving for the angular momentum H and kinetic energy T from the normalized values η and τ. Mathematically, the second optimization problem is expressed as

$$\underset{\mathbf{u_2}}{\text{minimize}} \quad J_2 = \sum_{i=1}^{N} \left(J_{H_2}^2(t_i) + J_{T_2}^2(t_i) + J_{\eta}^2(t_i) + J_{\tau}^2(t_i) \right) \quad ,$$

where the individual costs are given by

$$J_{H_2}(t_i) = \left\| 1 - \frac{1}{H^2} \left(\beta^2 c_1^2 \omega_1^2(t_i) + \beta^2 c_2^2 \omega_2^2(t_i) + \beta^2 c_3^2 \omega_3^2(t_i) \right) \right\|$$

$$J_{T_2}(t_i) = \left\| 1 - \frac{1}{2T} \left(\beta c_1 \omega_1^2(t_i) + \beta c_2 \omega_2^2(t_i) + \beta c_3 \omega_3^2(t_i) \right) \right\|$$

$$J_{\eta}(t_i) = \left\| \eta - \frac{H^2}{\beta^2} \right\|$$

$$J_{\tau}(t_i) = \left\| \tau - \frac{2T}{\beta} \right\|$$

(5.43)

and the control vector $\mathbf{u}_2$ is given as

$$\mathbf{u}_2 = \begin{bmatrix} H & T & \beta \end{bmatrix}^T.$$

(5.44)

The first optimization problem is initially solved by a heuristic particle swarm optimizer. The, possibly local or global, optima from the PSO is then used as an initial guess to an SQP optimization via Matlab's *fmincon*. The result of the SQP

is assumed as the optimal value for k_1^*, k_3^*, η^*, and τ^*. These values are then fed to to second optimization problem along with the angular velocity measurements. The process is repeated to develop a local minima via PSO as a warm start to SQP for optimal values of H^*, T^*, and β^*. These optimal values are then used to construct the principal MOI values by the Smelt parameter relations. These relations, described earlier, are given as

$$
\begin{aligned}
I_1^* &= \beta \left(\frac{1 + k_3^*}{1 - k_1^*} \right) \\
I_2^* &= \beta \left(\frac{1 + k_3^* k_1^*}{1 - k_1^*} \right). \\
I_3^* &= \beta
\end{aligned}
\tag{5.45}
$$

A graphical depiction of the two-step optimization is shown in Figure 5.4, and is also discussed in Algorithm 4.
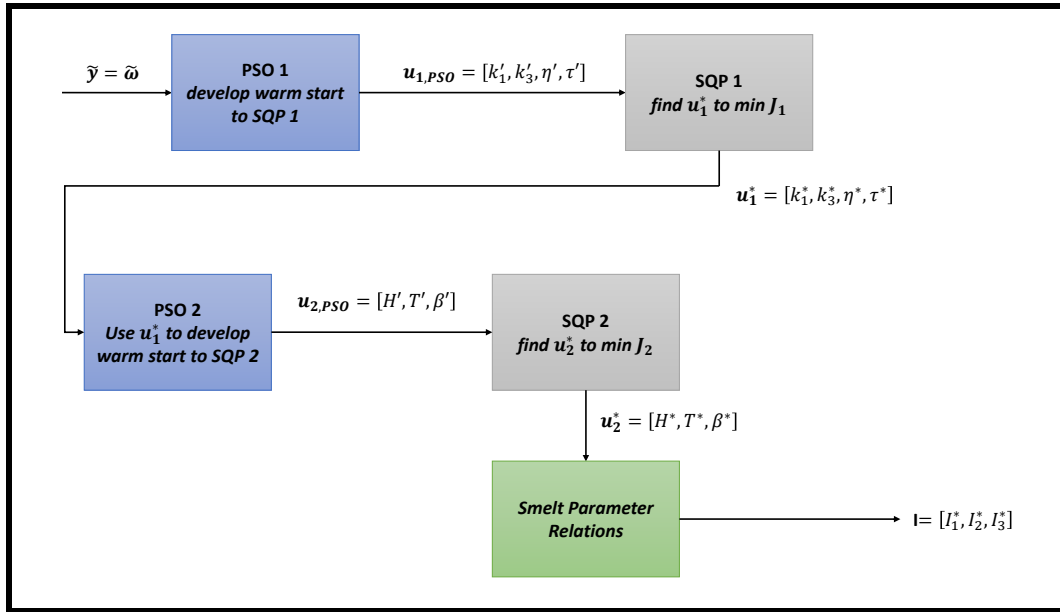
Figure 5.4: A graphical depiction of the two-step optimization process using PSO and SQP to estimate the principal MOI of a spacecraft given angular velocity data.

Algorithm 4: Heuristic Polhode Exploitation for MOI Estimation
---
    Given a time history of measured angular rate data $\boldsymbol{\omega}(t)$

1 Establish lower and upper bounds for design variables in $\mathbf{u}_1$

2 Minimize J_1 via a PSO for a local optimal $\mathbf{u}_1'$

3 Use $\mathbf{u}_1'$ as a warm start to a SQP to minimize J_1 for $u_1^* = [k_1^*, k_3^*, \eta^*, \tau^*]$

4 Establish lower and upper bounds for design variables in $\mathbf{u}_2$

5 With the optimal $\mathbf{u}_1^*$ as inputs, minimize J_2 with a heuristic PSO for a local optimal $\mathbf{u}_2'$

6 Use $\mathbf{u}_2'$ as a warm start to a SQP to minimize J_2 for $u_2^* = [H^*, T^*, \beta^*]$

7 With β^*, solve for optimal principal MOI estimate by Smelt parameter relations
---

The first optimization has a four-variable search space with values that are either constrained, or magnitudes that can be approximated by measured data. The second optimization has a three-variable search space whose values may take on more variability, but the PSO method typically finds a local minima that serves as an efficient first guess for the SQP solver. An initial one-step optimization method was attempted, but attempts consistently used circular logic to define values. This two-step process breaks up the process by exploiting the Smelt parameters and polhode in the first step, and uses those optimal estimates to solve the larger problem of estimating the principal MOI.

5.4 Results and Discussion

5.4.1 Numerical Results and Discussion for Relative MOI Ratio Estimation Using Single-Shooting.

This section will provide results and discussion on the employment of single-shooting algorithms to estimate the relative spacecraft MOI, the driving system parameter is Euler's rotational equations. Three cases are presented at two different noise levels. Case 1 is an axisymmetric body at a slower initial conditions. Case 2 is an axisymmetric body at fast angular velocity. Case 3 is an asymmetric tumbling

body at a slower angular velocity. Each scenario assumes an observation time of 30 seconds with one second time steps. The angular velocity about each axis is assumed as an available measurement. A damping coefficient of $\lambda = 10000$ is initially used with an adaption rate of $\tau = 2$. The initial conditions, MOI ratios, and nominal representative principal MOIs are given in Table 5.1.

Table 5.1: Relative MOI Ratio Single Shooting Test Cases

Scenario	$\boldsymbol{\omega}_0$ (deg/s)	MOI Ratios	Nominal MOI (kg-m^2)
Case 1	$\boldsymbol{\omega}_0 = [1, 1, 0.5]^T$	$\mathbf{p} = [0.5, -0.5, 0]^T$	$I_1 = 50, I_2 = 50, I_3 = 25$
Case 2	$\boldsymbol{\omega}_0 = [4, 2, 1]^T$	$\mathbf{p} = [0.5, -0.5, 0]^T$	$I_1 = 50, I_2 = 50, I_3 = 25$
Case 3	$\boldsymbol{\omega}_0 = [1, 1, 0.5]^T$	$\mathbf{p} = [0.2, -0.7143, 0.6]^T$	$I_1 = 50, I_2 = 35, I_3 = 25$

A summary of the average iterations and error for each simulation is provided in Table 5.2. A convergence tolerance of $\epsilon = N \cdot \sigma$ is used to ensure a tolerance level is in the vicinity of the noise floor, where N is the number of measurements. For

Table 5.2: Average results from single shooting simulations. 100 simulations with a convergence tolerance $\epsilon = N \cdot \sigma$.

Scenario	Estimate	Iterations	Error
Case 1, $\sigma = 10^{-6}$ deg/s	$\tilde{\mathbf{p}} = [0.5001, -0.5001, 0.0000]^T$	46.7	2.7968e-05
Case 1, $\sigma = 10^{-4}$ deg/s	$\tilde{\mathbf{p}} = [0.4996, -0.5001, -0.0001]^T$	27.8	2.7040e-03
Case 2, $\sigma = 10^{-6}$ deg/s	$\tilde{\mathbf{p}} = [0.4999, -0.5000, -0.0000]^T$	45.3	5.2707e-06
Case 2, $\sigma = 10^{-4}$ deg/s	$\tilde{\mathbf{p}} = [0.5002, -0.4999, -0.0000]^T$	31.5	5.0927e-04
Case 3, $\sigma = 10^{-6}$ deg/s	$\tilde{\mathbf{p}} = [0.2000, -0.7143, 0.6000]^T$	50.3	1.8669e-05
Case 3, $\sigma = 10^{-4}$ deg/s	$\tilde{\mathbf{p}} = [0.2001, -0.7132, 0.6007]^T$	27.6	1.9153e-03

all three cases, the 10^{-6} noise level requires between 45 and 50 iterations to reach the convergence tolerance. Although these measurements are the least corrupted by noise, the tolerance $\epsilon = N\sigma$ requires more adaptation on the λ damping parameter to meet the required level. The 10^{-4} noise level measurements require between 27 and 30 iterations to converge, but the noise floor has been raised in this scenario and requires less λ damping adaption to converge. The difference between the fast and slow rotations in Cases 1 and 2 are not as significant as expected. Both cases require the same order of iterations to converge and achieve accuracy on the same relative order. The more rapid spin in Case 2 does yield relative MOI error estimates on $O(10^{-6})$ and $O(10^{-4})$ compared to Case 1's error of $O(10^{-5})$ and $O(10^{-3})$. The fast spin produces more variability in the Jacobian, and allows for more information to update the design vector.

From Case 3, an example of the behavior of the λ damping coefficient is found in Figure 5.5. Similarly, an example of the value of the residual is found in Figure 5.6. For the first 10 iterations, updates to the design vector $\mathbf{p}$ are gradually decreasing the residual norm. As the residual is decreasing, the value of λ is also decreasing at a rate dictated by τ. An overshoot begins after the 10th iteration, and a series of λ adjustments are made. The adaption resembles chatter in the λ values, but the residual is gradually decreasing with under- and over-shooting until reaching the tolerance level.

Figure 5.7 provides an example of the resulting iterations of single-shooting applied to the relative MOI ratio design vector in Case 2. The iterated trajectory varies wildly after five iterations. Initial guesses project incorrect linear responses or incorrect concavity. After 10 iterations, the design vector has converged on a trajectory that is similar, but the residuals among the three directions are still above the tolerance. After 15 iterations, the design vector is within the basin of attraction of

133
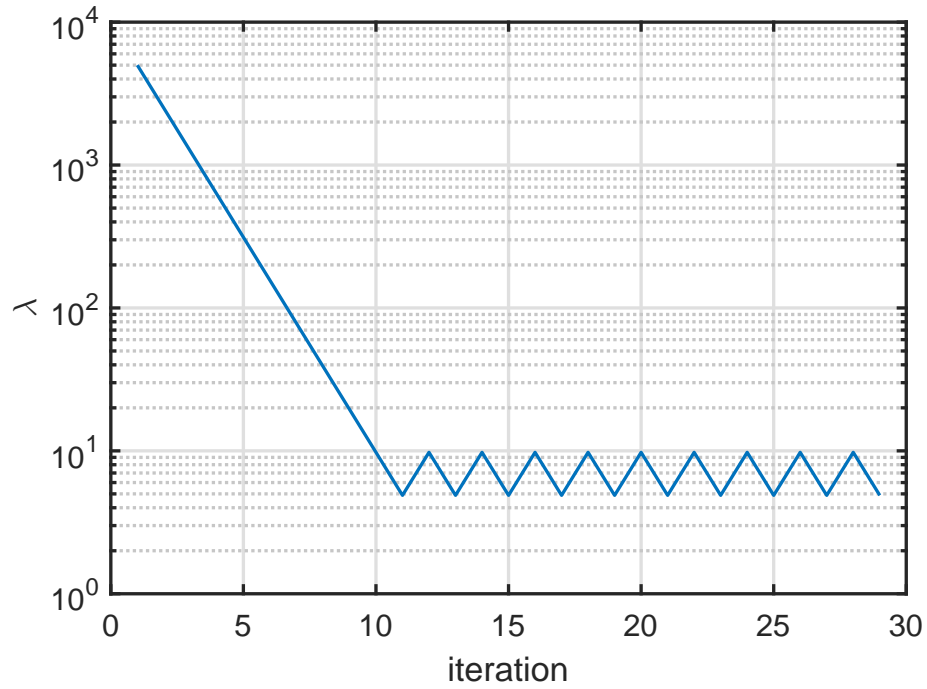
Figure 5.5: Example of the behavior of damping coefficient λ, taken from Case 3.
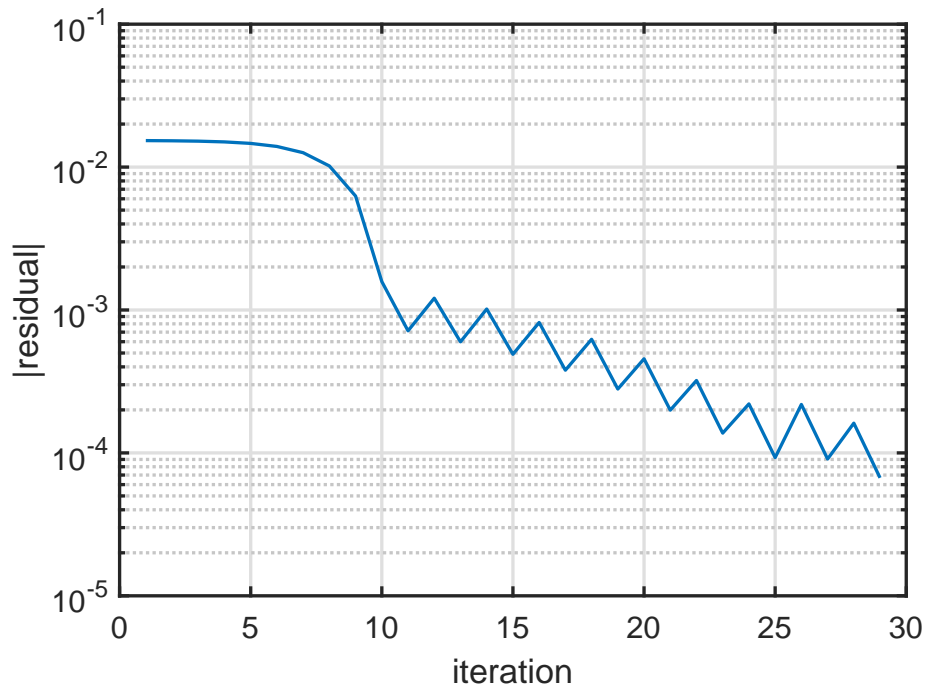
Figure 5.6: Example of the behavior of the residual norm, taken from Case 3.

134

the numerical scheme, and the remaining sets of 20, 25, and 30 iterations are resulting from the λ adaption in an attempt to minimize the residual norm below $\epsilon = N\sigma$.

This research has demonstrated success is estimating the relative MOI ratio by posing the problem as an ODE parameter estimation problem and implementing a single-shooting numerical iteration scheme. The estimated MOI ratio can be used to characterize the rotational motion, but in this development, the actual value of the principal MOI can not be determined without additional knowledge. The next section will provide a discussion on MOI estimation where the external torques are known and applied to the system.

5.4.2   Numerical Results and Discussion for Spacecraft MOI Estimation with Known Constant Torques.

This section will provide results and discussion on the employment of single-shooting algorithms to estimate the principal MOI of a spacecraft using measured angular velocity, posing the problem as an ODE parameter estimation problem in Euler's equations, but accounting for known external torques. This section will use Algorithm 3, replacing the EOMs with Euler's equations with external torques, and using the Jacobian developed in Eq. (5.31). Two MOI configurations will be examined using four cases of known external torques. A nominal noise level of $\sigma = 10^{-4}$ deg/s will be used for measurement simulation. An initial condition of $\boldsymbol{\omega}_0 = [2, 2, 0.5]^T$ deg/s will be used for each case as well. The error metric will be taken as

$$e_{\mathbf{p}} = ||\tilde{\mathbf{p}} - \mathbf{p}||, \tag{5.46}$$

where $\tilde{\mathbf{p}}$ is the 3×1 vector of estimated principal MOI, and $\mathbf{p}$ is the 3×1 vector of the true principal MOI. A description of the eight test cases is given in Table 5.3, and the individual MOI and moment profiles are given in Table 5.4.
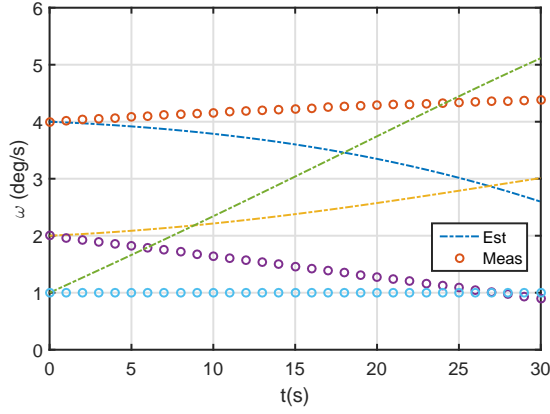
(a) Trajectory comparison - 5 iterations
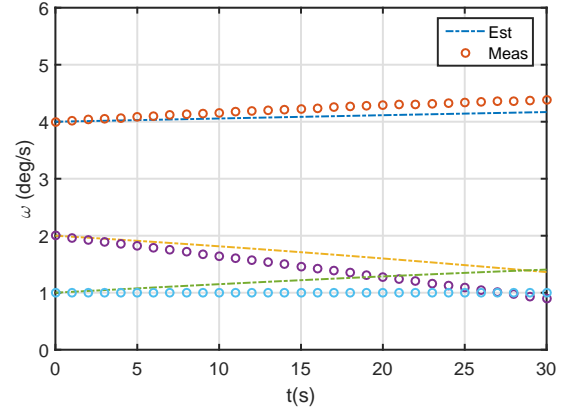
(b) Trajectory comparison - 10 iterations
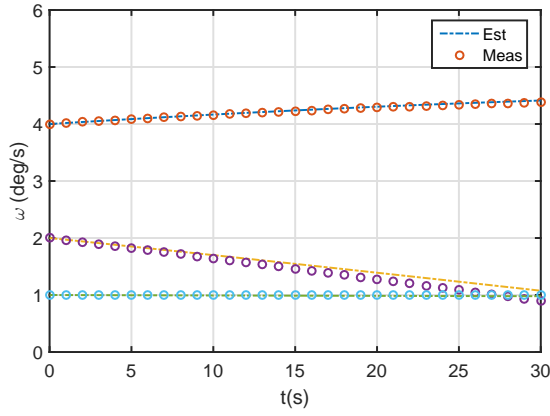
(c) Trajectory comparison - 15 iterations
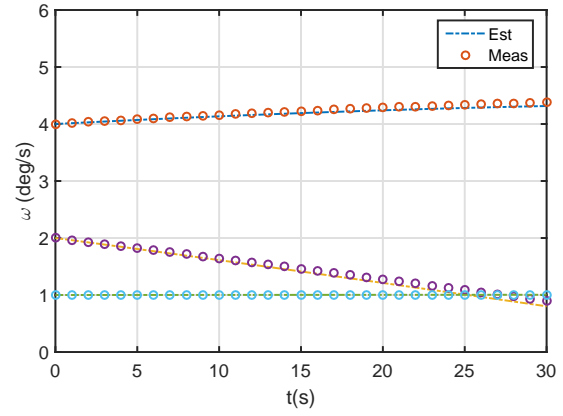
(d) Trajectory comparison - 20 iterations
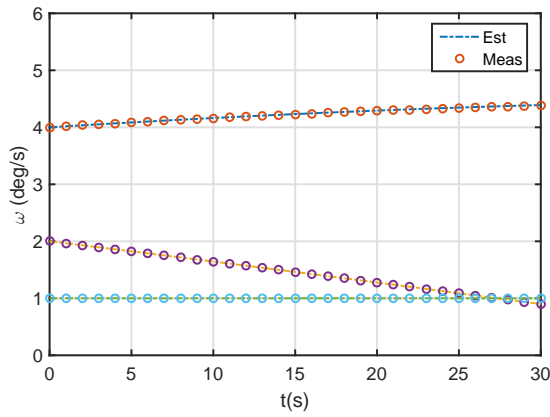
(e) Trajectory comparison - 25 iterations
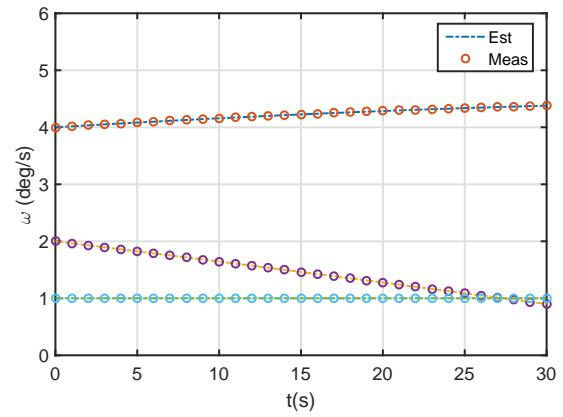
(f) Trajectory comparison - 30 iterations

Figure 5.7: Example of single-shooting applied to the relative MOI ratio in Case 2.

Table 5.3: Principal MOI Single Shooting Test Cases

Scenario	Nominal MOI (kg-m^2)	Moment Profile ($N \cdot m$)
Case 1	MOI 1	Moment 1
Case 2	MOI 2	Moment 1
Case 3	MOI 1	Moment 2
Case 4	MOI 2	Moment 2
Case 5	MOI 1	Moment 3
Case 6	MOI 2	Moment 3
Case 7	MOI 1	Moment 4
Case 8	MOI 2	Moment 4

Table 5.4: MOI and Moment Profile

Profile Name	Value
MOI 1	$I_1 = 50, I_2 = 50, I_3 = 25$ kg-m^2
MOI 2	$I_1 = 50, I_2 = 40, I_3 = 25$ kg-m^2
Moment 1	$M_1 = 0.001, M_2 = 0, M_3 = 0.001$ N-m
Moment 2	$M_1 = 0.001, M_2 = 0.001, M_3 = 0$ N-m
Moment 3	$M_1 = 0, M_2 = 0.001, M_3 = 0.001$ N-m
Moment 4	$M_1 = 0.001, M_2 = 0.001, M_3 = 0.001$ N-m

For each test case, a series of 1000 simulations are carried out. Table 5.5 provides a summary of the numerical experiment results, where the initial guess for each simulation is a random normally distributed 3×1 vector centered around the principal

MOI values with a σ of 5 kg-m^2. A convergence tolerance of $\epsilon = 10^{-3} \approx 0.06$ deg/s, or approximately 0.002 deg/s per time step is used.

Table 5.5: Average results from single shooting simulations estimating principal MOI. 1000 simulations with a convergence tolerance $\epsilon = 10^{-2} \approx 0.6$ deg/s, or approximately 0.02 deg/s per time step. Maximum number of iterations is 1000. Averages are taken from converged values. Initial guess randomly distributed around true value with $\sigma = 5$ kg-m^2.

Scenario	Convergence	Estimate	Iterations	Error (kg-m^2)
1	100	$\tilde{I}_1 = 50.07, \tilde{I}_2 = 49.97, \tilde{I}_3 = 26.07$	7.70	5.17
2	99.7	$\tilde{I}_1 = 49.97, \tilde{I}_2 = 39.94, \tilde{I}_3 = 24.86$	7.82	5.14
3	100	$\tilde{I}_1 = 50.31, \tilde{I}_2 = 50.14, \tilde{I}_3 = 26.23$	7.57	5.10
4	100	$\tilde{I}_1 = 50.36, \tilde{I}_2 = 40.35, \tilde{I}_3 = 24.95$	8.02	5.21
5	100	$\tilde{I}_1 = 50.12, \tilde{I}_2 = 50.04, \tilde{I}_3 = 26.07$	7.43	5.31
6	99.6	$\tilde{I}_1 = 50.10, \tilde{I}_2 = 40.09, \tilde{I}_3 = 24.82$	8.07	5.21
7	100	$\tilde{I}_1 = 50.06, \tilde{I}_2 = 49.95, \tilde{I}_3 = 25.86$	7.55	5.22
8	99.7	$\tilde{I}_1 = 50.17, \tilde{I}_2 = 40.07, \tilde{I}_3 = 25.05$	8.01	5.17

The axisymmetric configuration converges 100% of the time in each of the four moment profiles, averaging seven and eight iterations with an average error around 5.2 kg-m^2. The asymmetric configuration converges 100% of the time only in Case 6, where the applied moment is constant about the body 2- and 3-axes. In each of the 10 cases, the single-shooting method is able to converge on values near the principal MOI when accounting for applied, constant external moments.

The overall accurate performance of this method can be attributed to the initial guess used to initiate the iterative process. Under the same simulation conditions, the

experiment is repeated but the initial guess is generated from a random guess centered around the true value, but with a σ value of 15 kg-m ^{2}. The rates of convergence are gathered in Table 5.6.

Table 5.6: Convergence rates from single shooting simulations estimating principal MOI. 1000 simulations with a convergence tolerance $\epsilon = 10^{-2} \approx 0.6$ deg/s, or approximately 0.02 deg/s per time step. Maximum number of iterations is 1000. Averages are taken from converged values. Initial guess randomly distributed around true value with $\sigma = 15$ kg-m^2.

Scenario	Convergence Rate
1	21%
2	11%
3	20%
4	12%
5	22%
6	10%
7	21%
8	12%

The axisymmetric configuration has a convergence rate of approximately 20%, while the asymmetric spacecraft converges nearly 11% of the time. This poor performance is a direct consequence of the initial guess supplied to the LM iteration scheme. This result leads to the classical fact that a 'good' initial guess is required for nearly any numerical algorithm, whether a single-shooting iteration problem or an optimization problem. When the initial guess is *close enough*, the iterative process converges based on the given tolerance level. However, when the initial guess is not

within a basin of attraction for the solver, one can expect diverging results and poor estimates.

The benefit to estimating relative MOI ratios in Section 5.4.1 is the search space is limited to $[-1, 1]$ for all three parameters. Another benefit is only two of the parameters actually need to be iterated on, and the third will come from the Smelt parameter petal relation. This research presented here allows for the estimation of the actual principal MOI via a single-shooting method by exploiting the coupling between moments and MOI in Euler's equations, and the sensitivity introduced to the Jacobian. Constant external moments were assumed for this research, whereas the next step is to introduce time-varying moments, or moments that are functions of the MOI. This single-shooting method relies on an initial guess that is near the true value. For large, non-cooperative tumbling spacecraft, a close initial guess may not always be available and this creates a vast search space. Section 5.4.3 presents a method to estimate the actual principal MOI of a rigid body assuming torque-free motion by using constants of the motion and heuristic optimization techniques.

5.4.3 Numerical Results and Discussion for Relative MOI Ratio Estimation Using Heuristic Optimization and Polhode Exploitation.

This section will describe the results of implementing a two-step optimization process on simulated angular velocity data to estimate actual values of principal MOI by exploiting the polhodes of analytical rigid body mechanics and the Smelt parameters. Table 5.7 details the four different MOI configurations and the initial conditions for each scenario. Following the methodology proposed in Section 5.3.2, 100 simulations are carried out on the four different structural and angular velocity configurations, simulated at four different noise levels for a total of 1,600 numerical

simulations. Each simulation assumes 60 seconds of measurements available at a constant time step of one second unless otherwise specified.

Table 5.7: Principal MOI configurations used for the two-step optimization of polhodes using measured angular velocity.

MOI Configuration	Principal MOI (kg-m^2)	Initial Angular Velocity (deg/s)
1	$\mathbf{I}_1 = [50, 45, 30]$	$\boldsymbol{\omega}_0 = [4, 3, 1]^T$
2	$\mathbf{I}_2 = [500, 450, 300]$	$\boldsymbol{\omega}_0 = [4, 3, 1]^T$
3	$\mathbf{I}_3 = [100, 100, 50]$	$\boldsymbol{\omega}_0 = [2, 1, 1]^T$
4	$\mathbf{I}_5 = [200, 180, 120]$	$\boldsymbol{\omega}_0 = [5, 3, 2]^T$

Examining a simulation of Case 1 where an asymmetric spacecraft is tumbling with an initial angular velocity of $\boldsymbol{\omega}_0 = [4, 3, 1]^T$ deg/s, the first PSO run yields a final J_1 cost function evaluation of 5.743×10^{-6} but takes nearly 600 iterations and has parameter estimate errors around 5%. Using the output $\mathbf{u}_{1,\text{PSO}}$ to prime the first SQP to minimize J_1, the final cost for J_1 is $4.998e \times 10^{-7}$ in 19 iterations, an order of magnitude less than the PSO, and parameter estimate errors are less than 1%. The process is repeated using the optimal $\mathbf{u}_1^*$ values, and after the second PSO to SQP run, the final cost of J_2 is approximately 3.915×10^{-5} with estimate errors on the order of 0.3%.

The results from 100 simulations of Case 1 are presented in Table 5.8. The optimization scheme estimates the angular momentum and kinetic energy with the same relative accuracy for each noise value. For the two noise levels where H and T are off by approximately 1.5%, the intermediate MOI is off by nearly 4.5%, the minor MOI by 3.5%, and the major by 1.5%. From Figure 5.8, the optimal polhode underestimates the trace of the angular velocity trajectory along the ω_2 direction.

The accuracy of this estimate could likely be improved by increasing the sampling time to capture more of the curvature of the $\boldsymbol{\omega}$ data to fit the polhode. A similar trend occurs in Case 2, shown in Table 5.9 and Figure 5.9; however, the magnitude of the actual MOI values has been increased tenfold, amplifying the effcect of not capturing the curvature of the $\boldsymbol{\omega}$ path.

Case 3 presents the case of an axisymmetric body at a slow angular velocity. Theoretically, the angular velocity about the minor axis should remain constant for all time, and the polhode should only vary in the (ω_1, ω_2) plane. The optimized polhode created by the intersection of the two ellipsoids has a time variant ω_3 history. This, in effect, introduces a significant error to the minor MOI approximation, reaching up to 15%. The observed data does not produce enough variability for the algorithm to recognize the constant ω_3 history. When the time-history is increased from 60 seconds to 15 minutes, the average MOI estimate error after 100 simulations is found to be between 1% and 3% for the four noise levels. An example of the extended time history is found in Figure 5.11.

Table 5.8: Results from 100 simulations of Case 1 at four different noise levels. Variables with a tilde are final estimates. Numbers in parentheses indicate percent errors. Noise values are given in deg/s. Initial angular velocity is $\boldsymbol{\omega}_0 = [4, 3, 1]^T$ deg/s.

Case 1	$\tilde{H}$ (N·m·s)	$\tilde{T}$ (N·m·)	$\tilde{I}_1$ (kg-m^2)	$\tilde{I}_2$ (kg-m^2)	$\tilde{I}_3$ (kg-m^2)
True	**4.24**	**0.18**	**50**	**45**	**30**
$\sigma = 10^{-4}$	4.17 (-1.7%)	0.18 (1.8%)	49.2 (-1.6%)	42.9 (-4.5%)	28.9 (-3.7%)
$\sigma = 10^{-3}$	4.21 (-0.6%)	0.19 (0.7%)	49.8 (-0.5%)	43.4 (-3.6%)	29.2 (-2.8%)
$\sigma = 10^{-2}$	4.22 (-0.6%)	0.19 (0.7%)	49.8 (-0.5%)	43.4 (-3.6%)	29.2 (-2.5%)
$\sigma = 10^{-1}$	4.18 (-1.5%)	0.19 (1.6%)	49.3 (-1.4%)	43 (-4.4%)	29.0 (-3.3%)
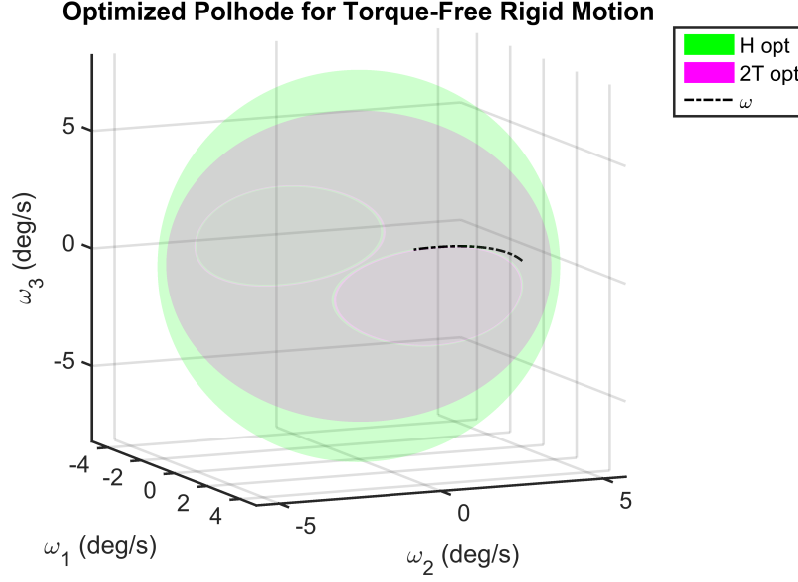
Figure 5.8: Example of an optimal polhode fit for Case 1 with $\sigma = 10^{-4}$ deg/s. Fitting resulted in a 0.5% estimate error in I_1, a 3.6% estimate error in I_2, and a 1.2% estimate error in I_3.

Table 5.9: Results from 100 simulations of Case 2 at four different noise levels. Variables with a tilde are final estimates. Numbers in parentheses indicate percent errors. Noise values are given in deg/s. Initial angular velocity is $\boldsymbol{\omega}_0 = [4, 3, 1]^T$

Case 2	$\tilde{H}$ (N·m·s)	$\tilde{T}$ (N·m·)	$\tilde{I}_1$ (kg-m^2)	$\tilde{I}_2$ (kg-m^2)	$\tilde{I}_3$ (kg-m^2)
True	**42.4**	**1.9**	**500**	**450**	**300**
$\sigma = 10^{-4}$	40.8 (-3.8%)	1.8 (-3.8%)	481.8 (-3.6%)	420.9 (-6.5%)	283.5 (-5.5%)
$\sigma = 10^{-3}$	42.1 (-0.8%)	1.9 (-0.8%)	497.0 (-0.6%)	434.4 (-3.5%)	292.0 (-2.7%)
$\sigma = 10^{-2}$	42.6 (-0.3%)	1.9 (-0.2%)	502.0 (0.4%)	438.9 (-2.5%)	294.8 (1-.8%)
$\sigma = 10^{-1}$	40.2 (-5.3%)	1.8 (-5.3%)	473.8 (-5.3%)	414.8 (-7.8%)	277.8 (-7.4%)

143
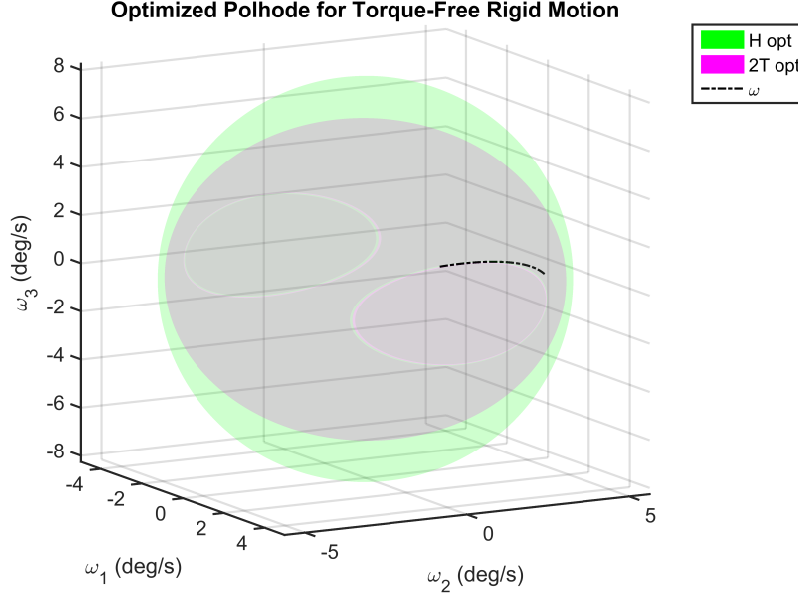
Figure 5.9: Example of an optimal polhode fit for Case 2 with $\sigma = 10^{-4}$ deg/s. Fitting resulted in a 0.3% estimate error in I_1, a 3.9% estimate error in I_2, and a 1.7% estimate error in I_3.

Table 5.10: Results from 100 simulations of Case 3 at four different noise levels. Variables with a tilde are final estimates. Numbers in parentheses indicate percent errors. Noise values are given in deg/s. Initial angular velocity is $\boldsymbol{\omega}_0 = [2, 1, 1]^T$

| Case 3	$\tilde{H}$ (N·m·s)	$\tilde{T}$ (N·m·)	$\tilde{I}_1$ (kg-m^2)	$\tilde{I}_2$ (kg-m^2)	$\tilde{I}_3$ (kg-m^2)
True	**3.99**	**0.084**	**100**	**100**	**50**
$\sigma = 10^{-4}$	4.03 (0.7%)	0.085 (0.8%)	100.53 (0.5%)	98.09 (-1.91%)	52.13 (4.2%)
$\sigma = 10^{-3}$	4.41 (10.3%)	0.093 (10.5%)	110.14 (10.1%)	107.08 (7.08%)	57.66 (15.3%)
$\sigma = 10^{-2}$	4.15 (3.8%)	0.087 (3.9%)	103.62 (3.6%)	100.94 (0.94%)	54.02 (8.1%)
$\sigma = 10^{-1}$	4.16 (4.1%)	0.087 (4.3%)	103.99 (3.9%)	101.10 (1.10%)	54.16 (8.3%)

144
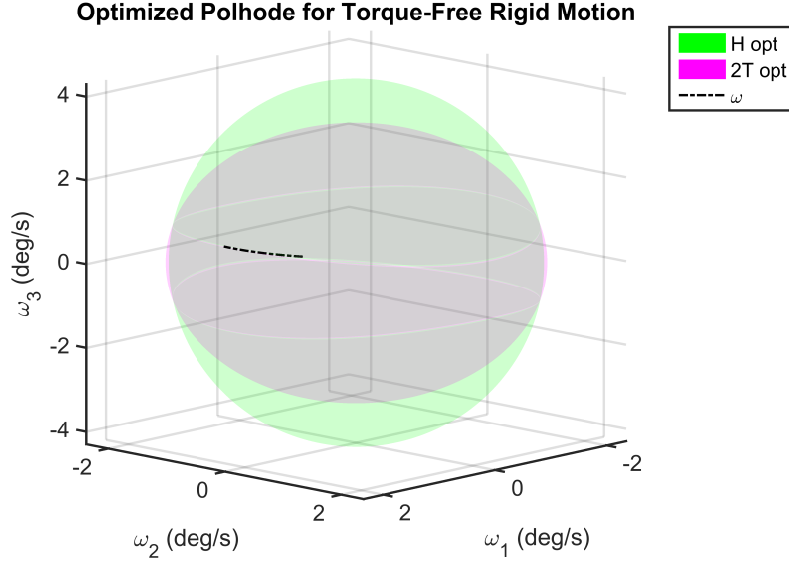
Figure 5.10: Example of an optimal polhode fit for Case 3 with $\sigma = 10^{-4}$ deg/s. Fitting resulted in a 1.4% estimate error in I_1, a 3.5% estimate error in I_2, and a 2.1% estimate error in I_3.

Figure 5.11: Example of an optimal polhode fit for Case 3 with $\sigma = 10^{-4}$ deg/s with an increased observation time of 15 minutes.

Case 4 represents an asymmetric body tumbling that is being observed for 60 seconds with a greater spin about the primary axis. The results for Case 4 are shown in Table 5.11 and Figure 5.12. The shape of the polhode is captured by the optimization process by fitting the two ellipsoids such that the error in both the rotational kinetic energy and angular momentum is approximately 1% for each noise level. Error estimates for the MOI is between 1% and 3% for all axes, with the exception of the 4% errors for the intermediate MOI for two noise levels. This is likely due to underestimating both H and T in these scenarios, shrinking the ellipsoids and altering the polhode path based on lack of observability. Increasing the measurement time to 15 minutes, Figure 5.13 displays an optimized polhode fit that matches the $\boldsymbol{\omega}$ data where MOI errors are between 0.2% and 1.1%. Extending the observation time allows the two-step optimization process to better form the intersection between the ellipsoids and determine the optimal MOI estimate.

Table 5.11: Results from 100 simulations of Case 4 at four different noise levels. Variables with a tilde are final estimates. Numbers in parentheses indicate percent errors. Noise values are given in deg/s. Initial angular velocity is $\boldsymbol{\omega}_0 = [5, 3, 2]^T$.

| Case 4	$\tilde{H}$ (N·m·s)	$\tilde{T}$ (N·m·)	$\tilde{I}_1$ (kg-m^2)	$\tilde{I}_2$ (kg-m^2)	$\tilde{I}_3$ (kg-m^2)
True	**20.3**	**1.1**	**200**	**180**	**120**
$\sigma = 10^{-4}$	20.5 (1.30%)	1.09 (-1.14%)	202.7 (1.33%)	176.7 (-1.79%)	117.9 (-1.71%)
$\sigma = 10^{-3}$	20.0 (1.25%)	1.07 (-1.36%)	197.9 (-1.04%)	176.4 (-4.09%)	114.9 (-3.74%)
$\sigma = 10^{-2}$	19.9 (-1.43%)	1.06 (-1.56%)	197.6 (-1.20%)	176.8 (-4.07%)	115.5 (-4.25%)
$\sigma = 10^{-1}$	20.5 (0.95%)	1.09 (-0.83%)	202.4 (1.18%)	179.9 (-1.67%)	117.9 (-1.72%)
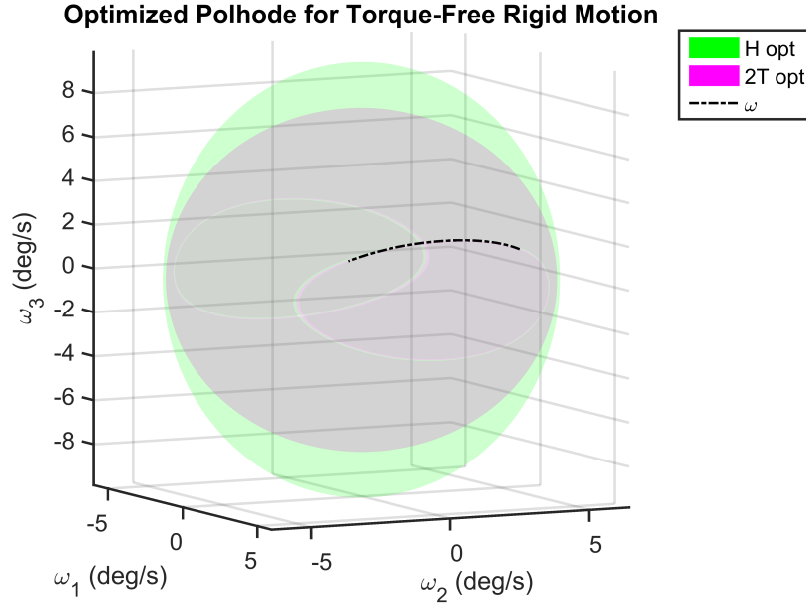
Figure 5.12: Example of an optimal polhode fit for Case 4 with $\sigma = 10^{-4}$ deg/s. Fitting resulted in a 0.9% estimate error in I_1, a 0.6% estimate error in I_2, and a 1.3% estimate error in I_3.
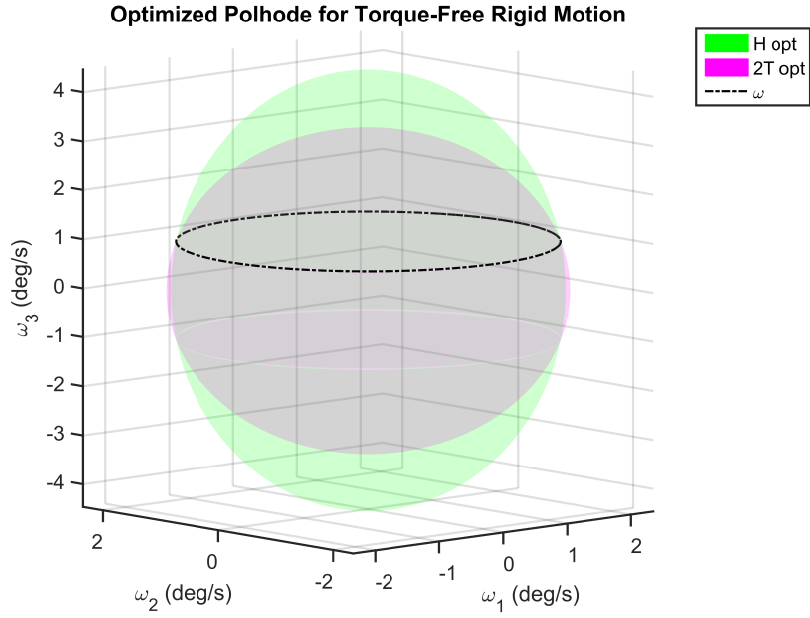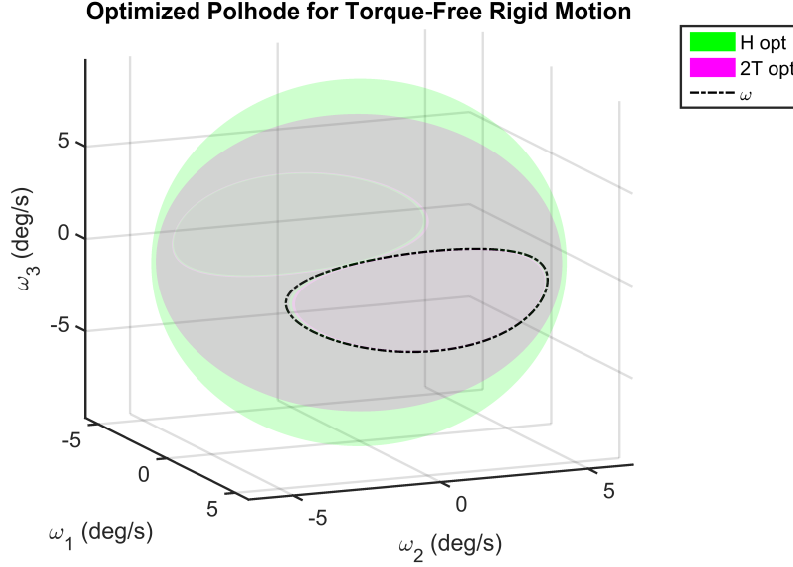
Figure 5.13: Example of an optimal polhode fit for Case 4 with $\sigma = 10^{-4}$ deg/s with an increased observation time of 15 minutes.

As a means to validate the two-step optimization in terms of cost values, and to justify the use of a warm start to the SQP algorithm, Figure 5.14 displays the average final cost function using the results of 100 simulations of each of the four test cases and the four noise levels. In each of the four noise cases, all of the test cases are able to locally minimize either J_1 or J_2 via the heuristic PSO. By inspection, the SQP is then able to use the local minima from the PSO as a primer to further minimize the cost function, in most cases by at least an order of magnitude.

5.5 Conclusions and Future Work

This research examined the inverse problem of the classic Euler's equations. That is, given measurements of the rotational trajectory and initial conditions, *can one determine the moment of inertia?* The proposed problem is now posed as one of parameter estimation in a nonlinear ordinary differential equation under the presence of stochastic measurement noise. Single-shooting methods employing Gauss-Newton
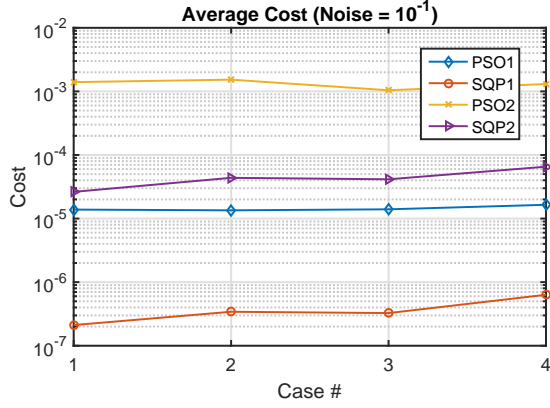
(a) Average cost value $\sigma = 10^{-1}$ deg/s
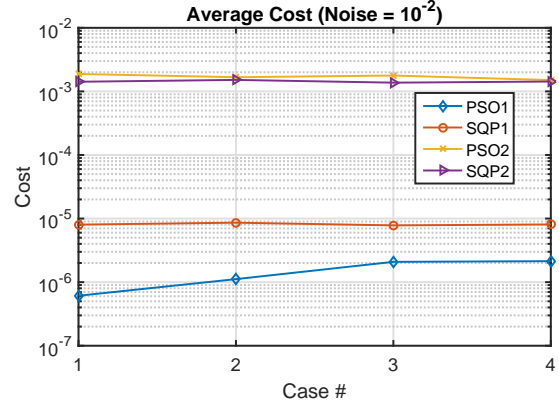
(b) Average cost value $\sigma = 10^{-2}$ deg/s
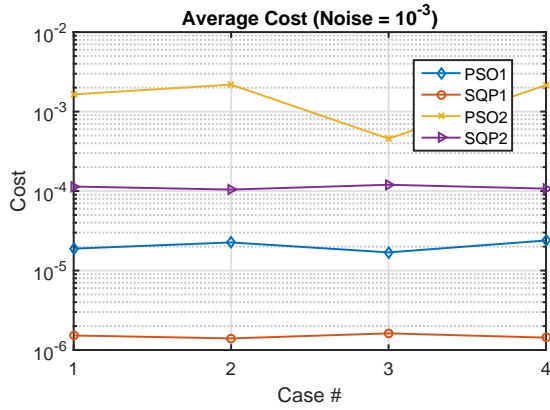
(c) Average cost value $\sigma = 10^{-3}$ deg/s
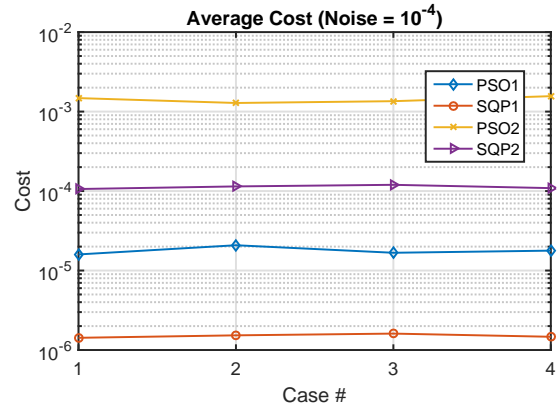
(d) Average cost value $\sigma = 10^{-4}$ deg/s

Figure 5.14: Average final cost values for 100 runs of the four test cases at four noise levels.

and Levenberg-Marquardt iteration schemes were employed. When using measured angular velocity data, relative MOI ratios were found by a single shooting numerical scheme. However, estimation of the principal MOI was found to be unsuccessful, unless coupling with known external moments is utilized. Internal moments and momentum exchange principles could also likely be applied as a solution to this problem.

In order to estimate the principal MOI, a heuristic optimization algorithm is used in conjunction with a SQP optimizer to minimize two novel cost functions constraining the rotational trajectory along the intersection of angular momentum and kinetic energy ellipsoids in a two-step optimization process. This in effect shapes two different ellipsoids representing constants of the motion such that their intersection is, within some tolerance, the three-dimensional path traced by the angular velocity. This shape is the well known polhode. The search space is bound by employing intermediate conversions of the Smelt parameters, and by normalized angular momentum and rotational kinetic energy in the first step of the minimization. The second step then searches for the actual values of H, T, and the MOI. Various structural configurations and rotational trajectories are investigated to assess the performance of the established estimation algorithms. Estimates are found, on average, to be within 1 to 5% of the true MOI values with some exceptions, with variations attributed to observation time and angular accelerations about particular axes. Referencing the research in Chapter 3, the MOI estimation routine developed in this chapter could be used to develop hypotheses for filter banks in the MMAE construct. Specific future work pertaining to this research will be detailed in Chapter 6.

VI. Conclusions

The initial goal of this research was strictly focused on the new application of adaptive estimation to spacecraft attitude with time varying MOI. During the course of the literature review and project development, a number of side research projects were discovered. The first problem was assessing whether new computational methods are beneficial to single-frame attitude determination. Further research then evolved to focus on techniques to estimate principal MOI and relative MOI ratios by numerical shooting and optimization techniques. The specific contributions of the research will first be discussed, followed by the conclusions of the three research projects and areas for future work.

6.1 Contributions

The main contributions of this dissertation are now detailed. A concise statement of the contribution will be given, and then a brief paragraph is provided for discussion.

New application of adaptive estimation to spacecraft with time-varying MOI: Motivated and discussed in Chapter 3, streaming attitude data was used to probabilistically classify and estimate the structural configuration of a spacecraft when the MOI is time-varying. This research was initially described in Hess [19] as a means to estimate sensor noise and sensor boom extension parameters, and was expanded in this research to a more complex spacecraft MOI model, provided by Leve [100], with deployable and separable payloads.

Modification and development of hybrid adaptive estimation schemes for sudden dynamics changes: Discussed in Chapter 3, Soken's [60] algorithm for sudden change detection via adaptive estimation was modified from assessing the state vector to assessing the parameter estimate using the parallel bank of filters. Soken's method was also modified in order to transition from an EKF to a UKF formulation.

A hybrid algorithm was developed that combined Soken's sudden change detection with the ALM method. The hybrid adaptive estimation scheme developed found that, for this scenario, the algorithm correctly identifies separating payloads between 90% and 99% of the time.

Rapid quartic eigendecomposition as applied to QUEST for single-frame attitude determination: A key contribution from the work in Chapter 4 resulted in the application of a rapid quartic root solver applied to the characteristic equation from Wahba's problem for a savings in computational cost. This method produces an average of 67% improvement to the QUEST computation time, using the same convergence tolerance for comparison. The decrease in computation time has the potential to reduce the time lag between attitude estimate and control calculation, facilitating near real-time optimal control. By solving simultaneously for all four eigenvalues, the method also avoids the possibility of converging on the *non* maximum eigenvalue to produce an incorrect attitude estimate.

Investigation of heuristic optimization techniques for attitude determination via Wahba's problem: The work in Chapter 4 examined the application of heuristic based techniques, to include particle swarm optimization (PSO) and genetic algorithms (GA), to solve Wahba's minimization problem to estimate spacecraft attitude. Both heuristic methods are capable of minimizing Wahba's cost function directly, but come with a significant increase in computation time compared to QUEST, q-method, and FQS. Although these methods are not well posed for on-board processing, the heuristic algorithms are applicable to off-line post-processing of vector observation time history. Direct minimization of the cost function by searching the (q_1, q_2, q_3) maintains the unit norm constraint and avoids Gibbs vector singularities.

Development of single-shooting parameter estimation technique as applied to Euler's rotational EOMs: The research in Chapter 5 developed an

algorithm that, given a series of simulated noisy angular velocity measurements, can converge on the relative MOI ratios using single-shooting and Levenberg-Marquardt iteration. An assumed external moment profile was analyzed and it was shown principal MOI can be estimated in this manner, but requires a close initial guess for convergence.

Exploitation of polhodes for estimation of principal MOI via a two-step optimization process: The work in Chapter 5 developed a method that combines a heuristic optimization in conjunction with an SQP optimizer to minimize two novel cost functions constraining the rotational trajectory along the intersection of angular momentum and kinetic energy ellipsoids in a two-step optimization process. This in effect shapes two different ellipsoids representing constants of the motion such that their intersection is, within some tolerance, the three-dimensional path traced by the angular velocity. Estimates are found, on average, to be within 1 to 5% of the true MOI values with some exceptions. These exceptions are attributed to observed measurements that do not fully capture the shape of the polhode intersection.

Demonstration of alternate method of ballistic coefficient estimation for a reentering spacecraft using MMAE: This brief work in Appendix C presents a method to estimate the ballistic coefficient of a reentering satellite using noisy radar data. A reentry is simulated to generate truth data and measurements of range, range rate, azimuth, and elevation. These measurements were corrupted and implemented in a MMAE bank of filters, each hypothesizing a different ballistic coefficient. Convergence on the correct model was shown as an example of MMAE as applied to a nonlinear system, but upon a further literature review, has not, to the knowledge of this author, been documented.

6.2 Research Conclusions and Future Work

6.2.1 Adaptive Estimation.

The purpose of the numerical experiment presented in Chapter 3 is to analyze the new application of adaptive estimation techniques to the time-varying spacecraft MOI problem. Three different scenarios were analyzed. The first scenario sought the identification of a spacecraft's relative MOI ratios, the driving parameter in torque-free rigid body motion. The second scenario sought the identification of a continuous command input for a gimbaled payload. The third scenario examined a series of separating payloads, each producing a discontinuity in the spacecraft MOI. A hybrid adaptive estimation scheme was developed that, for this scenario, performs on the same order of accuracy magnitude as the state-of-the-art.

Some key findings from this work exposed the need for rotational information about the three axes and the difficulty in estimating MOI ratios when unavailable, and also the need for variability and diversity in model hypotheses in an adaptive estimation filter bank construction. Another key finding was that the observable change in dynamics due to the MOI varying must be greater than the noise floor, otherwise it is likely the estimator will account for the dynamical changes by compensating in noise rejection calculations. This research allowed for the use of streaming attitude data to estimate structural changes and has served as an initial proof of concept, ultimately laying the foundation for future experimental work examining spacecraft MOI change detection via adaptive attitude estimation.

There are multiple paths and directions for future work regarding adaptive estimation. One of the first recommendations is a reformulation of the problem such that updated multiple model techniques may be applied. Reformulating the problem in the form of a Markov process will lend well to the use of an Interacting Multiple Model (IMM) that allows more mixing between models.

Following the translational maneuver detection proposed by Goff in [13], a rotational analog can be developed to detect changes in MOI. Rather than allowing the MOI to be a parameter or model in the filter bank, the problem could be reposed using an EKF and allow for a variable state dimension filter that adapts in size to include the MOI in the state vector. A metric such as the Mahalanobis distance would then be monitored, and above reaching a certain threshold, modifying the size of the state vector and inflating the covariance would allow convergence on a new MOI estimate, reducing the size again once the Mahalanobis distance reaches the threshold. The use of the Mahalanobis distance would allow for a decrease in models in the filter bank and for more variability in possible MOI modes, rather than assuming only M models in the bank are possibilities. The use of an IMM or other multiple model method using Markov chains also allows for more recent and advanced techniques such as pruning and mixing among models in the bank.

Chee and Forbes recently constructed the norm-constrained UKF and applied the filter to tracking high area-to-mass ratio (HAMR) space debris [117]. This norm-constrained UKF circumvents the intermediate attitude parameterization conversions used in the USQUE, which was the filter applied in this research. Chee follows a classical derivation of a norm-constrained EKF, but adapts the process for the UKF directly for the purpose of maintaining a unit quaternion norm. The use of this norm-constrained UKF would likely reduce the computational loading within the filter bank, and also allow for a smoothly propagated covariance, rather than matching covariances between parameterizations. Moreover, the use of this filter would also lend well to a full 6-DOF simulation rather than the complications faced with the USQUE method.

The use of different sensor sources is also of value to the academic and defense communities. This research examined the use of on-board gyros and magnetometers

to recursively estimate the attitude; however, this is easily adaptable by a simple change in the measurement-state relation $\tilde{\mathbf{y}} = \mathbf{h}(\mathbf{x})$. Other sensor sources include photometric light curve data, optical sensors, on-board star sensors, and so forth. Simulating the adaptive estimation problem with a variety of sensors is a key step in transitioning this research to technology.

Another area of future work is developing and modeling combined rotational and translational dynamics in the coupled attitude and orbit determination problem. Adaptive estimation of the two problems has been examined individually in the literature, but, other than the work by Linares [9; 62], the two sets of dynamics have not been combined. Examining combinations of time varying MOI and spacecraft translational maneuvers would be of great benefit to the community. Creating the combined translational/rotational problem could also lend well to incorporating thruster firings and higher-order perturbations to estimate non-conservative forces.

In order to generalize results, a means to non-dimensionalize the time scale of the adaptive estimation problem should be examined. Possible modes for research include normalizing by an orbit specific metric such as orbital period, or by a value associated with the rotational motion (such as a rotational period).

A final recommendation for future work in validating adaptive estimation research is the implementation of this numerical experiment in hardware. A simple experiment would involve suddenly adding mass to a ground-based satellite simulator with a known MOI configuration before a mass addition, and a known MOI configuration after an addition. Having certainty in the MOI of the spacecraft prior to a change event, along with certainty in the MOI after, these models would be included in a filter bank and, following the methodology in Chapter 3, perform an adaptive estimation with the streaming attitude data to demonstrate the capability

of this method. A hardware demonstration would give significant confidence in the efficacy shown by this method in the numerous simulations in this research.

6.2.2   Single-Frame Attitude Estimation.

This research proposed the application of Strobach's Fast Quartic Solver [18] to quickly solve the quartic eigenvalue problem required for the quaternion attitude estimate. The FQS algorithm decomposes the quartic characteristic equation of the **K** matrix into the product of two quadratics, and takes advantage of a well-defined Jacobian to equate polynomial coefficients via LU decomposition. This method produces an average of 67% improvement to the QUEST computation time, while using the same convergence criteria produces similar estimation error values. The decrease in computation time has the potential to reduce the time lag between attitude estimate and control calculation. By solving simultaneously for all four eigenvalues, the method also avoids the possibility of converging on the *non* maximum eigenvalue. The FQS application is prone to the same singularities as QUEST and the q-method, but these can be handled similarly by sequential rotations or other singularity avoidance or removal methods.

Additionally, this work examined the application of heuristic based techniques, to include particle swarm optimization (PSO) and genetic algorithms (GA), to solve Wahba's minimization problem to estimate spacecraft attitude. Both heuristic methods are capable of minimizing Wahba's cost (loss) function directly, but come with a significant increase in computation time compared to QUEST, q-method, and FQS. The algorithms also come with a computation complexity that may not be suitable for on board implementation. One of the main benefits to estimating the quaternion via a heuristic method is a 'close enough' initial guess is not required, as heuristic techniques implement randomly chosen initial candidate solutions. Although these methods are not well posed for on-board processing, the heuristic algorithms

157

are applicable to off-line post-processing of vector observation time history. Direct minimization of the cost function by searching the (q_1, q_2, q_3) consequently maintains the unit norm constraint and avoids Gibbs vector singularities.

Suggested future work involves the development of an analytical solution to the characteristic equation of the **K** matrix. Yang [44] met some success in developing an analytical solution, but some limitations were encountered. Future work could also re-parameterize the problem in terms of the Rodriguez parameters or some other form of attitude parameter of a dimension less than 4, and develop a closed-form solution to the minimization of Wahba's cost function. Moreover, re-parameterizing Wahba's cost function with an attitude parameter of dimension less than 4 would also decrease the computation time required in the heuristic optimization techniques.

6.2.3 *Moment of Inertia Estimation.*

Chapter 5 examined the inverse problem of the classic Euler's equations. That is, given measurements of the rotational trajectory and initial conditions, *can one determine the moment of inertia*? The current problem is now posed as one of parameter estimation in a nonlinear ordinary differential equation under the presence of stochastic measurement noise. Single-shooting methods employing Levenberg-Marquardt iteration schemes were employed. When using simulated measured angular velocity data, relative MOI ratios were found by a single shooting numerical scheme. However, estimation of the principal MOI was found to be less than successful, unless coupling with external moments is utilized.

In order to estimate the principal MOI, a heuristic optimization algorithm is used in conjunction with an SQP optimizer to minimize two novel cost functions constraining the rotational trajectory along the intersection of angular momentum and kinetic energy ellipsoids in a two-step optimization process. This in effect shapes two different ellipsoids representing constants of the motion such that their

intersection is, within some error tolerance, the three-dimensional path traced by the angular velocity. This shape is well known in analytical rigid body motion as a polhode. The search space is bound by employing intermediate conversions of the Smelt parameters, and by normalized angular momentum and rotational kinetic energy in the first step of the minimization. The second step then searches for the actual values of H, T, and parameter σ. Various structural configurations and rotational trajectories are investigated to assess the performance of the established estimation algorithms. Estimates are found, on average, to be within $< 1\%$ to 5% of the true MOI values with some exceptions. These exceptions are attributed to observed measurements that do not fully capture the shape of the polhode intersection.

The suggested future work in this research could involve estimation of the full MOI matrix and determining the products of inertia (the off-diagonal components). This would involve a reformulation of the kinetic energy and angular momentum constraints, and would also limit the use of Smelt parameters as an intermediate step. An additional step is then to take streaming quaternion data, and using the coupled relation between $\dot{\mathbf{q}}$ and $\dot{\boldsymbol{\omega}}$, determine if the MOI, in theory, can be estimated from streaming quaternions.

6.3   Summary

This research began focusing on applying adaptive estimation techniques to spacecraft attitude dynamics with time varying MOI. A number of research projects were also discovered that were distinct, but related, to the attitude estimation problem. Adaptive estimation techniques were applied and shown to be capable of detecting MOI variations, whether continuous or discontinuous. New techniques were either modified or developed that can detect discontinuities in MOI up to 98% of the time. A classical problem of attitude estimation was tackled with new computation

159

methods, decreasing the computation time by an average of nearly 67%. Numerical methods were also used to estimate the relative MOI ratios given noisy measured angular velocity, which are the key driving system parameters for rotational motion. Finally, the classical polhodes of analytical mechanics were exploited in a two-step optimization process to estimate the principal MOI of a rigid body, with results, on average, to be within $< 1\%$ to 5% of the true MOI values with some minor exceptions. Overall, this research has contributed to the field by providing new techniques to solve attitude determination problems accurately, quickly, and using techniques that are adaptable. The results in this research positively demonstrate with attitude dynamics the NRC's recommendation of the efficacy of multiple models when sudden changes in dynamics are expected, laying a foundation for future experimental hardware work validating these positive results, while simultaneously strengthening and bolstering the community's SSA techniques and capabilities.

Appendix A: Spacecraft Parameters used in Chapter 3, Scenario 2

This appendix will detail the assumed mass characteristics of the spacecraft investigated in Section 3.4.2. Section 3.3.4 details the development of the full spacecraft MOI model. All values are assumed to be nominal and for simulation purposes only and are not intended for use as design guidance or operational inputs, although care is taken to ensure the MOI values are mathematically valid. The static main bus MOI is assumed as

$$\mathbf{I}_B = \operatorname{diag}\left([240, 160, 100]\right) \text{kg-m}^2. \tag{A.1}$$

Table A.1 details the mass of and position vectors to the separable masses. Table A.2 details the parameters used for the solar panel and the other deployable payload.

Table A.1: Separable payload parameters used in Scenario 2 of Chapter 3

Payload	Mass (kg)	Position Vector $\hat{\mathbf{r}}_{S,i}$ (m)	Separable MOI $\mathbf{I}_{S,i}$ kg-m^2
1	50	$[1, 0, 0]^T$	$\operatorname{diag}\left([12, 12, 4]\right)$
2	25	$[0, 1, 0]^T$	$\operatorname{diag}\left([4.8, 4.8, 2.4]\right)$
3	20	$[0, 0, 1]^T$	$\operatorname{diag}\left([20, 20, 12]\right)$

Table A.2: Solar panel and payload parameters used in Scenario 2 of Chapter 3

Payload	Mass (kg)	MOI (kg-m^2)	Bus Arm $\bar{\mathbf{r}}$ (m)	Payload Arm $\tilde{\mathbf{r}}$ (m)
Solar Panel	35	$\operatorname{diag}\left([40, 40, 16]\right)$	$[0, 1.5, 0]^T$	$[0, 1, 0]^T$
Deployable	80	$\operatorname{diag}\left([50, 30, 30]\right)$	$[2, 0, 0]^T$	$[0, 2, 0.5]^T$

Appendix B: Spacecraft Parameters used in Chapter 3, Scenario 3

This appendix will detail the assumed mass characteristics of the spacecraft investigated in Section 3.4.3. Section 3.3.4 details the development of the full spacecraft MOI model. All values are assumed to be nominal and for simulation purposes only and are not intended for use as design guidance or operational inputs, although care is taken to ensure the MOI values are mathematically valid. The static main bus MOI is assumed as

$$\mathbf{I}_B = \mathrm{diag}\left([330, 240, 120]\right) \mathrm{kg\text{-}m}^2. \tag{B.1}$$

The static main bus MOI is assumed to account for the solar panels as well as the deployable payloads, which are non-rotating in this scenario. Table B.1 details the mass of and position vectors to the separable masses.

Table B.1: Separable payload parameters used in Scenario 3 of Chapter 3

Payload	Mass (kg)	Position Vector $\hat{\mathbf{r}}_{S,i}$ (m)	Separable MOI $\mathbf{I}_{S,i}$ kg-m^2
1	200	$[1, 0, 1]^T$	$\mathrm{diag}\left([40, 40, 20]\right)$
2	100	$[1, 1, 0]^T$	$\mathrm{diag}\left([10.5, 7.5, 4.5]\right)$
3	40	$[0, 1, 1]^T$	$\mathrm{diag}\left([10, 7, 5]\right)$

Appendix C: Ballistic Coefficient Estimation for a Re-entering Satellite using Ground Based Radar via Adaptive Estimation

This section presents a nominal example of parameter estimation via MMAE in a nonlinear system. The scenario is a satellite on a re-entry trajectory being tracked by a ground radar. The objective is to use MMAE to estimate the ballistic coefficient of the particular satellite. A UKF is implemented for the reentry estimation problem in order to demonstrate the efficacy of a parallel bank of UKFs in the MMAE architecture.

C.1 System Model

An uncontrolled satellite reentering the atmosphere can be modeled with a flat, non-rotating earth assumption, along with the assumption of constant gravity. The EOMs used in this example of parameter estimation in a coupled, nonlinear system are taken from [118], which differ slightly from Hicks [119], but will effectively serve for the current example. The system has six states, three position and three velocity. The system state vector $\mathbf{x}$ is defined as

$$\mathbf{x} = \begin{bmatrix} x & y & z & \dot{x} & \dot{y} & \dot{z} \end{bmatrix}^T, \tag{C.1}$$

where (x, y, z) is the three-dimensional location of the satellite with respect to a given ground radar, and the dotted variables indicate velocities. The system model $\dot{\mathbf{x}}$ is given as

$$\dot{\mathbf{x}} = \begin{bmatrix} \dot{x} & \dot{y} & \dot{z} & \ddot{x} & \ddot{y} & \ddot{z} \end{bmatrix}^T. \tag{C.2}$$

163

where double-dots indicate accelerations. The acceleration models are modified from [118] and given as

$$\ddot{x} = -\frac{\rho v^2 B^*}{2} g \cos \gamma_1 \cos \gamma_2$$
$$\ddot{y} = \frac{\rho v^2 B^*}{2} g \sin \gamma_1 - g \qquad , \qquad (\text{C.3})$$
$$\ddot{z} = -\frac{\rho v^2 B^*}{2} g \cos \gamma_1 \sin \gamma_2$$

where v is the 2-norm of the three velocity components at a given time, g is the gravitational acceleration, ρ is the density which will follow a simple exponential model given in [118], the flight path angles γ_1 and γ_2 are defined as

$$\gamma_1 = \tan^{-1}\left(-\frac{\dot{y}}{\sqrt{\dot{x}^2 + \dot{z}^2}}\right)$$
$$\gamma_2 = \tan^{-1}\left(-\frac{\dot{z}}{\dot{x}}\right) \qquad , \qquad (\text{C.4})$$

and the ballistic coefficient B^* is the ratio of the product of the satellite's drag coefficient C_D and area A to the satellite's mass m, given as

$$B^* = \frac{C_D A}{m}. \qquad (\text{C.5})$$

The accelerations are direct functions of ballistic coefficient, and are coupled by both the velocity term and the flight path angles, which are functions of velocity. Figure C.1 depicts the geometry of the current system.

C.2   Measurement Model

The work presented in [118] assumes all six states are available for measurements. This research introduces additional complexity to [118] by removing 33% of the available measurements. The measurement model used in this experiment will assume a ground radar is available that provides range ρ_r, range rate $\dot{\rho}_r$, azimuth α, and elevation ϵ. For compactness, let the vector $\boldsymbol{\rho}$ contain the position components $x, y,$ and z, and let the vector $\dot{\boldsymbol{\rho}}$ contain the position components $\dot{x}, \dot{y},$ and $\dot{z}$. The
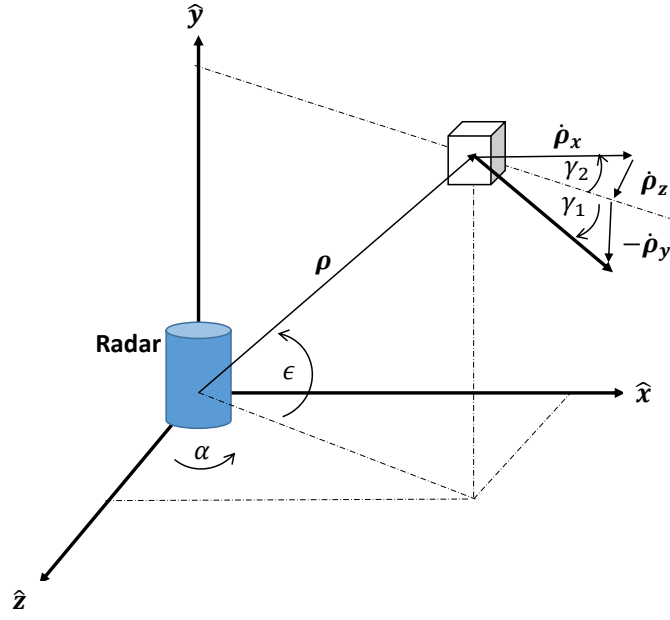
Figure C.1: Geometry for the ballistic reentry problem adapted from [118]

measurement model is then given as

$$
\begin{aligned}
\rho_r &= ||\boldsymbol{\rho}|| \\
\dot{\rho}_r &= \frac{\boldsymbol{\rho} \cdot \dot{\boldsymbol{\rho}}}{||\boldsymbol{\rho}||} \\
\alpha &= \tan^{-1}\left(\frac{x}{y}\right) \\
\epsilon &= \sin^{-1}\left(\frac{y}{\rho_r}\right)
\end{aligned}
\tag{C.6}
$$

The measurement vector $\tilde{\mathbf{y}}$ is then the collection of the four measurements, defined as

$$
\tilde{\mathbf{y}} = \mathbf{h}\left(\mathbf{x}\right) = \begin{bmatrix} \rho_r & \dot{\rho}_r & \alpha & \epsilon \end{bmatrix}^T.
\tag{C.7}
$$

The nominal ground radar is assumed to be calibrated with constant known noise levels that are Gaussian distributed given by the matrix $\mathbf{R}$ given as

$$\mathbf{R} = \begin{bmatrix} \sigma_\rho^2 & 0 & 0 & 0 \\ 0 & \sigma_{\dot{\rho}}^2 & 0 & 0 \\ 0 & 0 & \sigma_\alpha^2 & 0 \\ 0 & 0 & 0 & \sigma_\epsilon^2 \end{bmatrix} \tag{C.8}$$

C.3   Methodology

Truth data will be generated from a set of initial conditions and true dynamics model through numerical integration. Having simulated the true state and parameter values, range, range rate, azimuth, and elevation measurements will be calculated using the measurement relation $\mathbf{h}(\mathbf{x})$. The true measurements will then be corrupted by the given amount of measurement noise $\mathbf{R}_k$ that is zero-mean Gaussian distributed. The process noise $\mathbf{Q}_k$ is assumed constant as the zero matrix $\mathbf{0}_{6\times6}$. These measurements now serve as input to a parallel bank of filters, each assuming a different ballistic coefficient. The general form of each filter will follow the UKF described in this research in 2.2. The sigma points in each UKF are numerically propagated according to the specific filter's assumed dynamics, and the filter parameters are set such that $\kappa = 0, \alpha = 0.001, \beta = 2$ as described in [118]. The residuals and innovation covariance from each filter will then be input to the MMAE scheme, described in Section 2.4.

C.4 Results and Discussion

A ballistic reentry is modeled assuming the initial state used in [118]

$$
\mathbf{x}_0 = \begin{bmatrix} 13.55 \text{ km} \\ 30.48 \text{ km} \\ 0.30 \text{ km} \\ 0.43 \text{ km/s} \\ -0.08 \text{ km/s} \\ 0.10 \text{ km/s} \end{bmatrix}.
\tag{C.9}
$$

The initial covariance is assumed to be

$$
\mathbf{P}_0 = \begin{bmatrix} 1.524 \cdot \mathbf{1}_{3\times3} & \mathbf{0}_{3\times3} \\ \mathbf{0}_{3\times3} & 0.305 \cdot \mathbf{1}_{3\times3} \end{bmatrix}.
\tag{C.10}
$$

It is also assumed that target tracking has occurred prior to the beginning of the adaptive estimation algorithm, allowing for confidence in initial state and covariance estimates. A constant process noise $\mathbf{Q}_k$ is taken as

$$
\mathbf{Q}_k = \begin{bmatrix} 3.048 \cdot \mathbf{1}_{3\times3} & \mathbf{0}_{3\times3} \\ \mathbf{0}_{3\times3} & 6.096 \cdot \mathbf{1}_{3\times3} \end{bmatrix}.
\tag{C.11}
$$

A gravity constant of 9.81m/s^2 is assumed. The simulation time uses an initial time of $t_0 = 0$ and final time of $t_f = 3$ min with a constant time step of $\Delta t = 1$ sec. The true value for the ballistic coefficient is $B^* = 0.002 \text{ m}^2/\text{kg}$. A bank of 10 filters is constructed of potential ballistic coefficient values that are detailed in Table C.1. Figure C.2 shows the model likelihood time series along with the probabilistically weighted parameter estimate. Within eight seconds, the true model has already achieved the maximum likelihood among the models in the bank. Beginning around 25 seconds, Model 4 (whose B^*) is 0.04, compared to Model 5's true value of 0.05) begins to increase in likelihood and compete with Model 5, but the true value regains is

maxima around 65 seconds. After two minutes of tracking the re-entering spacecraft, the true model has a likelihood near unity and maintains that value for the remainder of the simulation. After reaching a probability of near one, the parameter estimate coincides with the true value. Figure C.3 displays the six estimated position and velocity states compared with the adaptive estimate and their respective 1σ bounds. A similar event occurs after approximately two minutes of processing, where the 1σ covariance bounds on the position estimates tighten around the true values following the likely identification of the true parameter.

Table C.1: Filter bank for the ballistic reentry ballistic coefficient estimation problem.

Model Number	B^* Value	Model Number	B^* Value
1	0.01	6	0.06
2	0.02	7	0.07
3	0.03	8	0.08
4	0.04	9	0.09
5 (True)	0.05	0.10	0.01
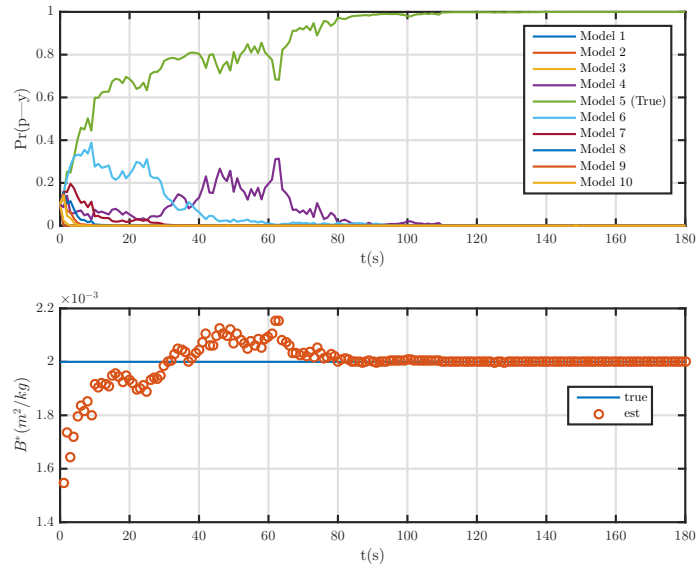
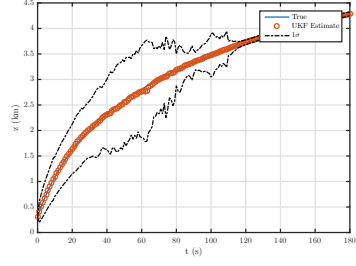Figure C.2: Likelihood time series and weighted B^* estimate for a realization of the reentry scenario.
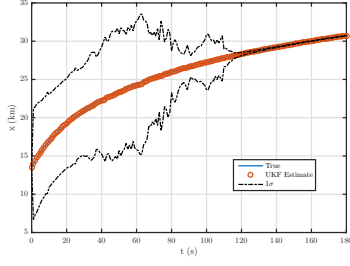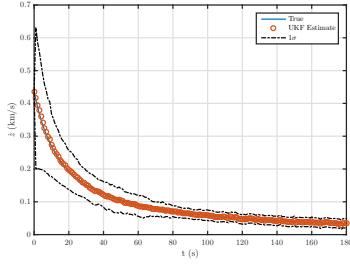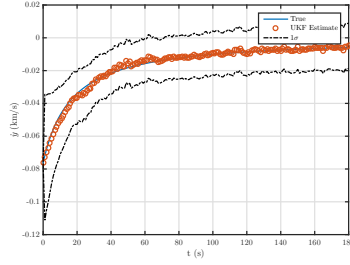
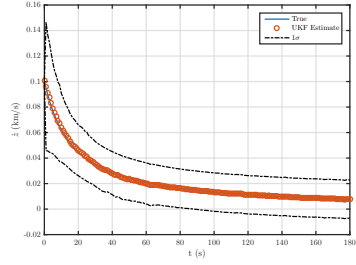(a) Position Estimate - x　　(b) Position Estimate - y　　(c) Position Estimate - z
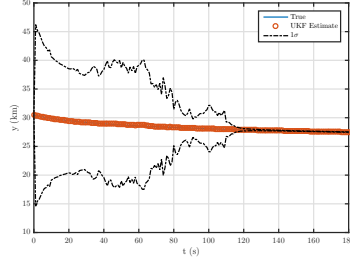
(d) Velocity Estimate - $\dot{x}$　　(e) Velocity Estimate - $\dot{y}$　　(f) Velocity Estimate - $\dot{z}$

Figure C.3: Comparison of position and velocity state estimates using a UKF on simulated radar data for the ballistic reentry problem.

Bibliography

[1] Department of Defense, "National Security Space Strategy [Unclassified Summary]," Tech. rep., 2011.

[2] Baird, M. A., "Maintaining Space Situational Awareness and Taking It to the Next Level," *Air and Space Power Journal*, Sep-Oct 2013, pp. 50–72.

[3] Sandau, R., "Implications of New Trends in Small Satellite Development," *Yearbook on Space Policy*, Vol. 2, 2011, pp. 296–312.

[4] Air Force Space Command, "Resiliency and Disaggregated Space Architectures White Paper," Tech. rep., 2013.

[5] Bombardelli, Claudio and Hernando-Ayuso, J., "Optimal Impulsive Collision Avoidance in Low Earth Orbit," *Journal of Guidance, Control, and Dynamics*, Vol. 38, No. 2, 2015, pp. 217–225.

[6] National Research Council, "Continuing Kepler's Quest Assessing Air Force Space Command's Astrodynamics Standards," Tech. rep., 2012.

[7] Hughes, P., *Spacecraft Attitude Dynamics*, Dover, 2004.

[8] Phys.org, "Japan gives up on failed black hole research satellite (Update)," 2016, http://phys.org/news/2016-04-japan-black-hole-satellite.html.

[9] Linares, R., Jah, M. K., and Crassidis, J. L., "Space object area-to-mass ratio estimation using multiple model approaches," *Advances in the Astronautical Sciences*, Vol. 144, 2012, pp. 55–72.

[10] Rago, C. and Mehra, R. K., "Robust Adaptive Target State Estimation for Missile Guidance using the Interacting Multiple Model Kalman Filter," *Position Location and Navigation Symposium, IEEE 2000*, 2000, pp. 355–362.

[11] Bogler, P., "Tracking a Maneuvering Target Using Input Estimation," *IEEE Transactions on Aerospace and Electronic Systems*, Vol. 3, 1987, pp. 298–310.

[12] Goff, G. M., Black, J. T., and Beck, J. A., "Tracking maneuvering spacecraft with filter-through approaches using interacting multiple models," *Acta Astronautica*, Vol. 114, 2015, pp. 152–163.

[13] Goff, C. G. M., Black, J. T., and Beck, J. A., "Orbit Estimation Of A Continuously Thrusting Satellite Using Variable Dimension Filters," *Journal of Guidance, Control, and Dynamics*, Vol. 38, No. 12, 2015, pp. 2407–2420.

[14] Lee, S. and Hwang, I., "Interacting Multiple Model Estimation for Spacecraft Maneuver Detection and Characterization," *AIAA Guidance, Navigation, and Control Conference*, AIAA SciTech, American Institute of Aeronautics and Astronautics, January 2015, pp. 1–9.

[15] Lee, S. and Hwang, I., "State-Dependent Adaptive Estimation for Impulsively Maneuvering Spacecraft Tracking," *AIAA Guidance, Navigation, and Control Conference*, AIAA SciTech, American Institute of Aeronautics and Astronautics, January 2016, pp. 1–13.

[16] Crassidis, J. L. and Markley, F. L., "Unscented Filtering for Spacecraft Attitude Estimation," *Journal of Guidance, Control, and Dynamics*, Vol. 26, No. 4, 2003, pp. 536–542.

[17] Markley, F. L., "Attitude determination using vector observations - A fast optimal matrix algorithm," *The Journal of the Astronautical Sciences*, Vol. 41, No. 2, 1993, pp. 261–280.

[18] Strobach, P., "The fast quartic solver," *Journal of Computational and Applied Mathematics*, Vol. 234, No. 10, 2010, pp. 3007–3024.

[19] Hess, J. A., Swenson, E. D., Leve, F. A., Black, J., and Goff, G. M., "Adaptive Estimation of Nonlinear Spacecraft Attitude Dynamics with Time-Varying Moments of Inertia Using On-Board Sensors," *AIAA Guidance, Navigation, and Control Conference*, AIAA SciTech, American Institute of Aeronautics and Astronautics, January 2016, pp. 1–18.

[20] Wahba, G., "Problem 65-1 : A Least Squares Estimate of Satellite Attitude," *SIAM Review*, Vol. 7, No. 3, 1965, pp. 409.

[21] Davenport, P. B., "A Vector Approach to the Algebra of Rotations with Applications," Tech. Rep. NASA TN D-4696, NASA Goddard Space Flight Center, 1968.

[22] Hall, C. D., *Spacecraft attitude dynamics and control*, 2001.

[23] Shuster, M. D. and Oh, S. D., "Three-axis attitude determination from vector observations," *Journal of Guidance and Control*, Vol. 4, No. 1, 1981, pp. 70–77.

[24] Crassidis, J. L., Markley, F. L., and Cheng, Y., "Survey of Nonlinear Attitude Estimation Methods," *Journal of Guidance, Control, and Dynamics*, Vol. 30, No. 1, January 2007, pp. 12–28.

[25] Shuster, M. D., "A Survey of Attitude Representations," *The Journal of the Astronautical Sciences*, Vol. 41, No. 4, 1993, pp. 439–517.

[26] Schaub, H. and Junkins, J., *Analytical Mechanics of Space Systems*, American Institute of Aeronautics and Astronautics, Reston ,VA, January 2003.

[27] Shuster, M. D., "The Nature of the Quaternion," *The Journal of the Astronautical Sciences*, Vol. 56, No. 3, 2008, pp. 359–373.

[28] Schaub, H. and Junkins, J. L., "Stereographic orientation parameters for attitude dynamics: a generalization of the Rodrigues parameters," *The Journal of the Astronautical Sciences*, Vol. 44, No. 1, 1996, pp. 1–19.

[29] Doupe, C., *Optimal Attitude Control of Agile Spacecraft Using Combined Reaction Wheel and Control Moment Gyroscope Arrays*, Phd thesis, Air Force Institute of Technology, 2015.

[30] Thakur, D., Srikant, S., and Akella, M. R., "Adaptive Attitude-Tracking Control of Spacecraft with Uncertain Time-Varying Inertia Parameters," *Journal of Guidance, Control, and Dynamics*, Vol. 38, No. 1, January 2015, pp. 41–52.

[31] Doroshin, A. V., "Analysis of attitude motion evolutions of variable mass gyrostats and coaxial rigid bodies system," *International Journal of Non-Linear Mechanics*, Vol. 45, No. 2, 2010, pp. 193–205.

[32] Narrea, M. I. and Lanchares, V., "Chaos in the Reorientation Process of a Dual-spin Spacecraft with Time-dependent Moments of Inertia," *International Journal of Bifurcation and Chaos*, Vol. 10, No. 5, 2000, pp. 997–1018.

[33] de Matos Lino, M. F. G., *Design and Attitude Control of a Satellite with Variable Geometry*, Master thesis, Instituto Superior Tecnico, 2013.

[34] Thakur, D. and Marchand, B. G., "Tracking Control of Nanosatellites with Uncertain Time Varying Parameters," *AAS/AIAA Spaceflight Mechanics Meeting*, 2012.

[35] Wiesel, W., *Modern Orbit Determination*, Aphelion Press, 2010.

[36] Lefferts, E., Markley, F., and Shuster, M. D., "Kalman Filtering for Spacecraft Attitude Estimation," *Journal of Guidance, Control, and Dynamics*, Vol. 5, No. 5, 1982, pp. 417–429.

[37] Stengel, R., *Optimal Control and Estimation*, Dover, 1994.

[38] Vallado, D., *Fundamentals of Astrodynamics and Applications*, Springer, 3rd ed., 2007.

[39] Vandyke, M. C., Schwartz, J. L., and Hall, C. D., "Unscented Kalman Filtering for Spacecraft Attitude State and Parameter Estimation," *in Proceedings of the AAS/AIAA Space Flight Mechanics Conference, no. AAS 04-115, (Maui*, 2004, pp. 1–13.

[40] Julier, S., Uhlmann, J., and Durrant-Whyte, H., "A new approach for filtering nonlinear systems," *Proceedings of 1995 American Control Conference - ACC'95*, Vol. 3, No. June, 1995, pp. 1628–1632.

[41] Julier, S. J. and Uhlmann, J. K., "Unscented filtering and nonlinear estimation," *Proceedings of the IEEE*, Vol. 92, No. 3, March 2004, pp. 401–422.

[42] Idan, M., "Estimation of rodrigues parameters from vector observations," *IEEE Transactions on Aerospace and Electronic Systems*, Vol. 32, No. 2, 1996, pp. 578–586.

[43] Psiaki, M. L., "Backward-Smoothing Extended Kalman Filter," *Journal of Guidance, Control, and Dynamics*, Vol. 28, No. 5, September 2005, pp. 885–894.

[44] Yang, Y. and Zhou, Z., "An analytic solution to Wahbas problem," *Aerospace Science and Technology*, Vol. 30, No. 1, 2013, pp. 46–49.

[45] Psiaki, M. L., "Attitude-Determination Filtering via Extended Quaternion Estimation," *Journal of Guidance, Control, and Dynamics*, Vol. 23, No. 2, 2000, pp. 206–214.

[46] Thienel, J., Luquette, R., and Sanner, R., "Estimation of Spacecraft Inertia Parameters," *AIAA Guidance, Navigation and Control Conference and Exhibit*, August 2008.

[47] Kay, S., *Fundamentals of Statistical Signal Processing, Volume I: Estimation Theory*, Prentice-Hall, 1993.

[48] Goff, C. G. M., Showalter, C. D., Black, J. T., and Beck, J. A., "Parameter Requirements for Noncooperative Satellite Maneuver Reconstruction Using Adaptive Filters," *Journal of Guidance, Control, and Dynamics*, Vol. 38, No. 3, 2015, pp. 361–374.

[49] Li, X. and Jilkov, V., "Survey of maneuvering target tracking. Part V: multiple-model methods," *IEEE Transactions on Aerospace and Electronic Systems*, Vol. 41, No. 4, 2005, pp. 1255–1321.

[50] Li, X.-R., "Engineer's guide to variable-structure multiple-model estimation for tracking," *Multitarget-multisensor tracking: Applications and advances*, 2000, pp. 499–567.

[51] Magill, D. T., "Optimal Adaptive Estimation of Sampled Stochastic Processes," 1963.

[52] Magill, D., "Optimal adaptive estimation of sampled stochastic processes," *IEEE Transactions on Automatic Control*, Vol. 10, No. 4, 1965, pp. 434–439.

[53] Lainiotis, D. G., "Optimal adaptive estimation: Structure and parameter adaption," *IEEE Transactions on Automatic Control*, Vol. AC-16, No. 2, 1971, pp. 160–170.

[54] Maybeck, P., *Stochastic Models, Estimation, and Control, Vol II*, Academic Press, New York, 1982.

[55] Bloom, H. A. P., "An efficient filter for abruptly changing systems," *Decision and Control, 1984. The 23rd IEEE Conference on*, 1984, pp. 656 – 658.

[56] Rupp, D., Ducard, G., Shafai, E., and Geering, H., "Extended Multiple Model Adaptive Estimation for the Detection of Sensor and Actuator Faults," *Proceedings of the 44th IEEE Conference on Decision and Control*, No. 4, Ieee, 2005, pp. 3079–3084.

[57] Tudoroiu, N., Sobhani-Tehrani, E., and Khorasani, K., "Interactive bank of unscented Kalman filters for fault detection and isolation in reaction wheel actuators of satellite attitude control system," *IECON Proceedings (Industrial Electronics Conference)*, 2006.

[58] Bolandi, H., "Effect of dynamic model of satellite on accuracy of attitude estimation with unknown star sensor noise level," *Second International Conference on Control, Instrumentation, and Automation*, 2011, pp. 1091–1096.

[59] Soken, H., Sakai, S., and Wisniewski, R., "In-orbit estimation of time-varying residual magnetic moment," *IEEE Transactions on Aerospace and Electronic Systems*, Vol. 50, No. 4, 2014, pp. 3126–3136.

[60] Soken, H. E. and Sakai, S.-i., "Multiple-Model Adaptive Estimation of Time-Varying Residual Magnetic Moment for Small Satellites," *Advances in Aerospace Guidance, Navigation and Control: Selected Papers of the Third CEAS Specialist Conference on Guidance, Navigation and Control held in Toulouse*, edited by J. Bordeneuve-Guibé, A. Drouin, and C. Roos, Springer International Publishing, Cham, 2015, pp. 303–321.

[61] Linares, R., Crassidis, J., and Jah, M. K., "Space object classification and characterization via Multiple Model Adaptive Estimation," *Information Fusion (FUSION), 2014 17th International Conference on*, 2014, pp. 1–7.

[62] Linares, R., Crassidis, J. L., Jah, M. K., and Kim, H., "Astrometric and Photometric Data Fusion for Resident Space Object Orbit, Attitude, and Shape Determination Via Multiple-Model Adaptive Estimation," *AIAA Guidance, Navigation, and Control Conference*, No. August, 2010, pp. AIAA 2010–8341.

[63] Lam, Q. and Crassidis, J., "Precision Attitude Determination Using a Multiple Model Adaptive Estimation Scheme," *2007 IEEE Aerospace Conference*, Ieee, 2007, pp. 1–20.

[64] Lam, Q. and Crassidis, J., "Evaluation of a Multiple Model Adaptive Estimation Scheme for Space Vehicle's Enhanced Navigation Solution," *AIAA Guidance, Navigation and Control Conference and Exhibit*, , No. August, 2007, pp. 1–21.

[65] Tanygin, S. and Williams, T., "Mass Property Estimation Using Coasting Maneuvers," *Journal of Guidance, Control, and Dynamics*, Vol. 20, No. 4, July 1997, pp. 625–632.

[66] Lee, A. Y. and Wertz, J. a., "In-Flight Estimation of the Cassini Spacecraft's Inertia Tensor," *Journal of Spacecraft and Rockets*, Vol. 39, No. 1, 2002, pp. 153–155.

[67] Peck, M., "Mass-properties estimation for spacecraft with powerful damping," *AAS/AIAA Astrodynamics Specialist Conference*, Girdwood, Alaska, 1999.

[68] Norman, M. C., Peck, M. A., and O'Shaughnessy, D. J., "In-orbit estimation of inertia and momentum-actuator alignment parameters," *Advances in the Astronautical Sciences*, Vol. 140, No. 6, November 2011, pp. 911–928.

[69] Bordany, R., Stern, W., and Crawford, M., "In-Orbit Estimation of the Inertia Matrix and Thruster Parameters of UoSAT-12,," *14th Annual AIAA/USU Conference on Small Satellites*, 2000.

[70] Ferguson, P. A., "On-Orbit Spacecraft Inertia and Rate Sensor Scale Factor Estimation for Microsatellites," *22nd Annual AIAA/USU Conference on Small Satellites*, Logan, Utah, 2008.

[71] Wright, J., *Advancements of In-Flight Mass Moment of Inertia and Structural Deflection Algorithms for Satellite Attitude Simulators*, Phd thesis, Air Force Institute of Technology, 2015.

[72] Colebank, J., Jones, R., Nagy, G., Pollack, R., and Mannebach, D., *SIMSAT: A Satellite System Simulator and Experimental Test Bed for Air Force Research*, Master thesis, Air Force Institute of Technology, 1999.

[73] Roach, N., Rohe, W., and Welty, N., *A Systems Engineering Approach to the Design of a Spacecraft Dynamics and Control Testbed*, Master thesis, Air Force Institute of Technology, 2008.

[74] Sheinfeld, D. and Rock, S., "Rigid Body Inertia Estimation with Applications to the Capture of a Tumbling Satellite," *AAS/AIAA Spaceflight Mechanics Meeting*, Savannah, GA, 2009, pp. 343–356.

[75] Luke, S., *Essentials of Metaheuristics*, Lulu, 2nd ed., 2014.

[76] Conway, B. A., "A Survey of Methods Available for the Numerical Optimization of Continuous Dynamic Systems," *Journal of Optimization Theory and Applications*, Vol. 152, No. 2, September 2012, pp. 271–306.

[77] Eberhart, R. and Kennedy, J., "A new optimizer using particle swarm theory," *MHS'95. Proceedings of the Sixth International Symposium on Micro Machine and Human Science*, 1995, pp. 39–43.

[78] Pontani, M. and Conway, B. a., "Particle Swarm Optimization Applied to Space Trajectories," *Journal of Guidance, Control, and Dynamics*, Vol. 33, No. 5, September 2010, pp. 1429–1441.

[79] Showalter, D. J. and Black, J. T., "Responsive Theater Maneuvers via Particle Swarm Optimization," *Journal of Spacecraft and Rockets*, June 2014, pp. 1–10.

[80] Salehizadeh, S. M. A., Yadmellat, P., and Menhaj, M. B., "Local optima avoidable particle swarm optimization," *2009 IEEE Swarm Intelligence Symposium, SIS 2009 - Proceedings*, 2009, pp. 16–21.

[81] Schmitt, M. and Wanka, R., "Particle swarm optimization almost surely finds local optima," *Theoretical Computer Science*, Vol. 561, No. PA, 2015, pp. 57–72.

[82] Showalter, D. J., *Optimal Autonomous Spacecraft Resiliency Maneuvers using Metaheuristics*, Phd thesis, Air Force Institute of Technology, 2014.

[83] Boeringer, D. W. and Werner, D. H., "Particle swarm optimization versus genetic algorithms for phased array synthesis," *IEEE Transactions on Antennas and Propagation*, Vol. 52, No. 3, 2004, pp. 771–779.

[84] Pontani, M. and Conway, B. A., "Optimal finite-thrust rendezvous trajectories found via particle swarm algorithm," *Advances in the Astronautical Sciences*, Vol. 142, No. 6, November 2012, pp. 3781–3800.

[85] Rahimi, A., Dev Kumar, K., and Alighanbari, H., "Particle Swarm Optimization Applied to Spacecraft Reentry Trajectory," *Journal of Guidance, Control, and Dynamics*, Vol. 36, No. 1, January 2013, pp. 307–310.

[86] Hu, D., Sarosh, A., and Dong, Y. F., "An improved particle swarm optimizer for parametric optimization of flexible satellite controller," *Applied Mathematics and Computation*, Vol. 217, No. 21, 2011, pp. 8512–8521.

[87] Fang, H. and Chen, L., "Application of an enhanced PSO algorithm to optimal tuning of PID gains," *2009 Chinese Control and Decision Conference, CCDC 2009*, , No. 1, 2009, pp. 35–39.

[88] Holland, J. H., *Adaptation in Natural and Artificial Systems: An Introductory Analysis with Applications to Biology, Control and Artificial Intelligence*, MIT Press, Cambridge, MA, USA, 1992.

[89] Thompson, R. E., Colombi, J. M., Black, J. T., and Ayres, B. J., "Disaggregated space system conceptual design optimization - Stochastic analysis methods," *2015 IEEE Aerospace Conference*, 2015, pp. 1–16.

[90] Mosher, T., "Conceptual Spacecraft Design Using a Genetic Algorithm Trade Selection Process," Vol. 36, No. 1, 1999, pp. 200–208.

[91] Diniz, H., *Navigation Constellation Design Using a Multi-Objective Genetic Algorithm*, Master thesis, Air Force Institute of Technology, 2003.

[92] Thompson, R. E., Colombi, J. M., Black, J., and Ayres, B. J., "Model-Based Conceptual Design Optimization Methods: Disaggregated Weather System Follow-On," *Journal of Spacecraft and Rockets*, Vol. 52, No. 4, 2015, pp. 1021–1037.

[93] Abbate, E., *Disaggregated Imaging Spacecraft Constellation Optimization with a Genetic Algorithm.*, Master thesis, Air Force Institute of Technology, 2014.

[94] Abdelkhalik, O. and Mortari, D., "Orbit Design for Ground Surveillance Using Genetic Algorithms," *Journal of Guidance, Control, and Dynamics*, Vol. 29, No. 5, September 2006, pp. 1231–1235.

[95] Kim, Y. H. and Spencer, D. B., "Optimal Spacecraft Rendezvous Using Genetic Algorithms," *Journal of Spacecraft and Rockets*, Vol. 39, No. 6, 2002, pp. 859–865.

[96] Alfriend, K. T., Lee, D., and Creamer, N. G., "Optimal Servicing of Geosynchronous SateIIites," *J. Guidance*, Vol. 29, No. 1, 2005, pp. 203–206.

[97] Arribas, M., Elipe, A., and Palacios, M., "Quaternions and the rotation of a rigid body," *Celestial Mechanics and Dynamical Astronomy*, Vol. 96, No. 3-4, 2006, pp. 239–251.

[98] Marschke, J., Crassidis, J., and Lam, Q., "Multiple Model Adaptive Estimation for Inertial Navigation During Mars Entry," *AIAA/AAS Astrodynamics Specialist Conference and Exhibit*, 2008, pp. 1–18.

[99] Sekhavat, P., Gong, Q., and Ross, I. M., "Unscented Kalman Filtering: NPSAT1 Ground Test Results," *AIAA Guidance, Navigation, and Control Conference*, August 2007.

[100] Leve, F., "Personal correspondence regarding spacecraft MOI development," .

[101] Shuster, M. D., "A Simple Kalman Filter and Smoother for Spacecraft Attitude," *The Journal of the Astronautical Sciences*, Vol. 37, No. 1, 1989, pp. 89–106.

[102] Chang, G., "Total least-squares formulation of Wahba's problem," *Electronics Letters*, Vol. 51, No. 17, 2015, pp. 1334–1335.

[103] Shuster, M. D., "The Generalized Wahba Problem," *The Journal of the Astronautical Sciences*, Vol. 54, No. 2, 2006, pp. 245–259.

[104] Markley, F. L., "Equivalence of Two Solutions of Wahba's Problem," *Journal of Astronautical Science*, Vol. 60, No. 2, 2013, pp. 303–312.

[105] Birkhoff, B. and MacLane, S., *A Survey of Modern Algebra*, Macmillan, New York, 1996.

[106] Forbes, J. R. and de Ruiter, A. H. J., "Linear-Matrix-Inequality-Based Solution to Wahba's Problem," *Journal of Guidance, Control, and Dynamics*, Vol. 38, No. 1, 2015, pp. 147–151.

[107] Palimaka, J. and Burlton, B. V., "Estimation of Spacecraft Mass Properties Using Angular Gyro Data," *Guidance, Navigation, and Control Conference Hilton Head Island, SC*, 1992.

[108] Jo, S. and Bang, H., "Mass Property Estimation of Gyroless Spacecraft," *11th International Conference on Control, Automation, and Systems*, 2011, pp. 1884–1887.

[109] Rimrott, F., *Introductory Attitude Dynamics*, Springer-Verlag, New York, 1989.

[110] Dogruer, C. U., "Estimation of Odometer Parameters with MMAE and LSE," *2014 IEEE/ASME International Conference on Advanced Intelligent Mechatronics*, No. 1, 2014, pp. 1728–1733.

[111] West, N. and Swiler, L., "2010 AIAA SDM Student Symposium Parameter Estimation via Gaussian Processes and Maximum Likelihood Estimation," 2010, pp. 5800.

[112] David, B. and Bastin, G., "A maximum likelihood parameter estimation method for nonlinear dynamical systems," *Proc IEEE Conf Decis Control*, Vol. 1, December 1999, pp. 612–617.

[113] Donnet, S. and Samson, A., "Estimation of parameters in incomplete data models defined by dynamical systems," *Journal of Statistical Planning and Inference*, Vol. 137, No. 9, 2007, pp. 2815–2831.

[114] Hamilton, F., "Parameter Estimation in Differential Equations: A Numerical Study of Shooting Methods," 2011, pp. 16–31.

[115] Shawash, J. and Selviah, D., "Real-time non-linear parameter estimation using the Levenberg-Marquardt algorithm on Field Programmable Gate Arrays," Vol. 60, No. 1, 2012, pp. 170–176.

[116] Ramsay, J. O., Hooker, G., Campbell, D., and Cao, J., "Parameter Estimation for Differential Equations: A Generalized Smoothing Approach," *Differential Equations*.

[117] Chee, S. A. and Forbes, J. R., "Norm-constrained Unscented Kalman Filter with Application to High Area-to-Mass Ratio Space-Debris Tracking," *AIAA Guidance, Navigation, and Control Conference*, AIAA SciTech, American Institute of Aeronautics and Astronautics, January 2016, pp. 1–18.

[118] Alizadeh, G. and Fallah, M. A., "Design of Novel Augmented Extended and Unscented Kalman Filters for Uncontrolled Satellites," *AIAA Infotech@Aerospace Conference*, 2009.

[119] Hicks, K. D., *Introduction to Astrodynamic Reentry*, AFIT/EN/TR-09-03, 2009.

REPORT DOCUMENTATION PAGE

The public reporting burden for this collection of information is estimated to average 1 hour per response, including the time for reviewing instructions, searching existing data sources, gathering and maintaining the data needed, and completing and reviewing the collection of information. Send comments regarding this burden estimate or any other aspect of this collection of information, including suggestions for reducing this burden to Department of Defense, Washington Headquarters Services, Directorate for Information Operations and Reports (0704–0188), 1215 Jefferson Davis Highway, Suite 1204, Arlington, VA 22202–4302. Respondents should be aware that notwithstanding any other provision of law, no person shall be subject to any penalty for failing to comply with a collection of information if it does not display a currently valid OMB control number. **PLEASE DO NOT RETURN YOUR FORM TO THE ABOVE ADDRESS.**

1. REPORT DATE *(DD–MM–YYYY)*	2. REPORT TYPE	3. DATES COVERED *(From — To)*
15–09–2016	Dissertation	October 2013 - September 2016

4. TITLE AND SUBTITLE

Adaptive Estimation and Heuristic Optimization of Nonlinear Spacecraft Attitude Dynamics

5a. CONTRACT NUMBER

5b. GRANT NUMBER

5c. PROGRAM ELEMENT NUMBER

6. AUTHOR(S)

Hess, Joshuah A., Captain, USAF

5d. PROJECT NUMBER

5e. TASK NUMBER

5f. WORK UNIT NUMBER

7. PERFORMING ORGANIZATION NAME(S) AND ADDRESS(ES)

Air Force Institute of Technology
Graduate School of Engineering and Management (AFIT/EN)
2950 Hobson Way
Wright-Patterson AFB, OH 45433-7765

8. PERFORMING ORGANIZATION REPORT NUMBER

AFIT-ENY-DS-16-S-061

9. SPONSORING / MONITORING AGENCY NAME(S) AND ADDRESS(ES)

Withheld

10. SPONSOR/MONITOR'S ACRONYM(S)

11. SPONSOR/MONITOR'S REPORT NUMBER(S)

12. DISTRIBUTION / AVAILABILITY STATEMENT

Distribution Statement A:
Approved for Public Release; Distribution Unlimited

13. SUPPLEMENTARY NOTES

This work is declared a work of the U.S. Government and is not subject to copyright protection in the United States.

14. ABSTRACT

For spacecraft conducting on-orbit operations, changes to the structure of the spacecraft are not uncommon. These planned or unanticipated changes in inertia properties couple with the spacecraft's attitude dynamics and typically require estimation. For systems with time-varying inertia parameters, multiple model adaptive estimation (MMAE) routines can be utilized for parameter and state estimates. MMAE algorithms involve constructing a bank of recursive estimators, each assuming a different hypothesis for the system's dynamics. This research has three distinct, but related, contributions to satellite attitude dynamics and estimation. In the first part of this research, MMAE routines employing parallel banks of unscented attitude filters are applied to analytical models of spacecraft with time-varying mass moments of inertia (MOI), with the objective of estimating the MOI and classifying the spacecraft's behavior. New adaptive estimation techniques were either modified or developed that can detect discontinuities in MOI up to 98% of the time in the specific problem scenario. Second, heuristic optimization techniques and numerical methods are applied to Wahba's single-frame attitude estimation problem, decreasing computation time by an average of nearly 67%. Finally, this research poses MOI estimation as an ODE parameter identification problem, achieving successful numerical estimates through shooting methods and exploiting the polhodes of rigid body motion with results, on average, to be within $< 1\%$ to 5% of the true MOI values.

15. SUBJECT TERMS

Attitude Dynamics, Multiple Model Adaptive Estimation, Attitude Estimation, Heuristic Optimization

16. SECURITY CLASSIFICATION OF:			17. LIMITATION OF ABSTRACT	18. NUMBER OF PAGES	19a. NAME OF RESPONSIBLE PERSON
a. REPORT	b. ABSTRACT	c. THIS PAGE			Dr. Eric D. Swenson, AFIT/ENY
U	U	U	U	203	19b. TELEPHONE NUMBER *(include area code)* (937) 255-3636 x7479 eric.swenson@afit.edu